Aeroelastic Limit Cycle Oscillations Mitigation Using Linear and Nonlinear Tuned Mass Dampers

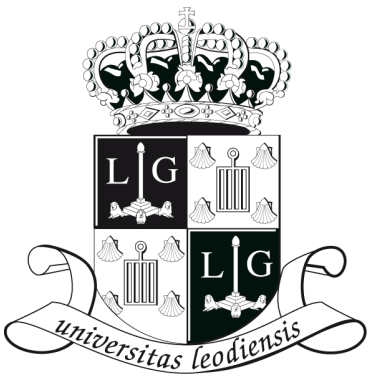

Edouard VERSTRAELEN

Department of Aerospace and Mechanical engineering

University of Liège

A thesis submitted for the degree of

Doctor of Philosophy

January 2018

Members of the Examination Committee

GILET, Tristan - President - Professor at University of Liège

DIMITRIADIS, Grigorios - Supervisor - Professor at University of Liège

KERSCHEN, Gaëtan - Supervisor - Professor at University of Liège

RAVEH, Daniella - Professor at Technion Israel Instritute of Technology

DE TROYER, Tim - Professor at Vrije Universiteit Brussel

MICHON, Guilhem - Professor at Institut Supérieur de l'Aéronautique et de l'Espace

Abstract

Flutter is a destructive aeroelastic phenomenon occurring on flexible aeronautical structures because of an energy exchange between two or more of the system's vibration modes and an airflow. In some rare cases, limit cycle oscillations (LCOs) related to flutter are observed because of nonlinearities, which might require aircraft redesign or flight envelope limitations. One way of suppressing such LCOs could be using Linear and Nonlinear Tuned Vibration Absorbers ((N)LTVAs), which are widely used in civil engineering but have to date received very little attention in the aerospace community.

The objectives of this thesis are the understanding of nonlinear aeroelastic phenomena and the investigation and demonstration of the beneficial effects of such absorbers for flutter and LCO suppression. Two nonlinear aeroelastic systems featuring smooth (continuously hardening) and non-smooth (freeplay) nonlinearities are investigated by means of mathematical models and wind tunnel experiments.

An increase in flutter speed of up to 35% is observed on the former system, both in the wind tunnel and using the model, however, a very precise tuning of the absorber's natural frequency is required. On the other hand, a negligible increase in LCO onset speed is observed on the latter system although a reduction in LCO amplitude of up to 60% is achieved in a given airspeed range, using a nonlinear absorber whose nonlinearity mimics that of the aeroelastic apparatus. The effect of linear and nonlinear vibration absorbers on the shape of the limit cycle branches of aeroelastic systems is described in detail and it is shown that such devices can change the nature of bifurcations from supercritical to subcritical and vice versa and can even cause the appearance of isolated solution branches. Therefore, extreme care must be taken when designing and implementing LTVAs and NLTVAs, as their effectiveness in increasing the linear flutter speed can be compromised by the change in the nature of the bifurcation. Furthermore, it is shown that a LTVA can not only delay classical flutter but also delay/suppress stall flutter.

Acknowledgements

Even though this thesis only bears my name, it wouldn't have seen the light of the day without the support of many people whom I would like to express my gratitude to, for their support but also for for making this journey enjoyable and enriching.

First, I would like to thank all the people without whom nothing would have been possible: my advisors, Gaetan Kerschen and Greg Dimitriadis for their trust, guidance, support and availability, the European Union for the funding (ERC Starting Grant NoVib 307265), and the members of the jury for taking the time to review this work.

Then, I would like to thank my friends and colleagues Marco, Thibaut, Vincent, Samir, Thomas and all the others, for all the technical (or not) discussions that provided (hopefully) good ideas, a good working atmosphere, a proper understanding of the plot of Game of Thrones and amazing "B" strategies.

I spent quite a bit of time fiddling with bolts, bearings and aluminium bits and I would like to thank Mathieu and Antonio for their help and their advice.

Twenty seventeen has been a rough year and I would like to thank all those who contributed in making it brighter.

I would also like to thank the Colettes for watering my parents' plants on that 8th of August and for all the fond memories that arose from that day, in Russia, in Durham, in Blindeff, in the Swabs, in Angleur, and everywhere else.

Last but not least, I would like to thank my family and all my friends for everything. I wish I had something cool to tell them but unfortunately I do not right now. Sorry folks.

« Attention
cette thèse n'est pas
une thèse sur
le cyclimse »

d'après M.Hazanavicius

Contents

Chapter 1

Introduction

1.1 Aeroelastic problems throughout history

Most theses ever written about aeroelasticity start from Collar's triangle [1]. This one makes no exception. Introduced in 1946 and depicted in figure 1.1, the triangle defines the aeroelasticity as the branch of physics that involves the combination of structural, inertial and aerodynamic forces.

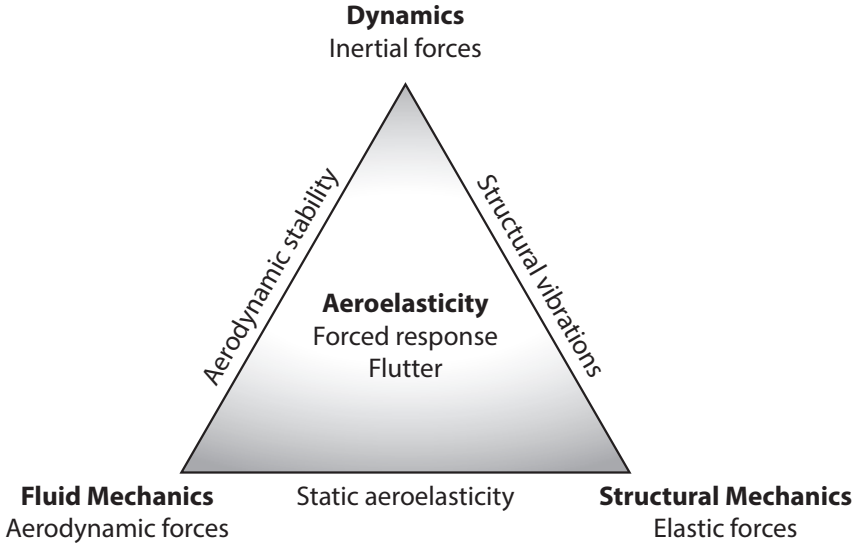

Figure 1.1: Collar's triangle of forces [1]

Even though it was not named as such yet, static aeroelasticity was discovered centuries ago when aerodynamic structures such as wind mill blades and sails had to withstand wind loads. Static aeroelasticity was actually one of the major design parameters of the first aircraft whose very low thrust required very light structures and therefore very low

structural strength. The Langley machine (figure 1.2(a)), for instance, crashed on the Pomotac river in 1903 because of a classical torsional divergence of the wing [2, 3]. This phenomenon occurs when the torsional stiffness of the wing is lower than the aerodynamic moment, resulting in a diverging response that leads to the destruction of the wing. Similarly, the Foker D8 (figure 1.2(b)) suffered from flexural wing failure during high load manoeuvres because the lack of sufficient torsional stiffness of the wing combined with the aerodynamic loads led to an increase in the angle of attack of the wing tips, resulting in flexural loads larger than designed [4]. A similar phenomenon, due to the lack of sufficient torsional stiffness, is control surface reversal where the moment induced by the deflection of the control surfaces leads to a wing twist that reduces the wing tips' angle of attack, which counters the effects of the control surface.

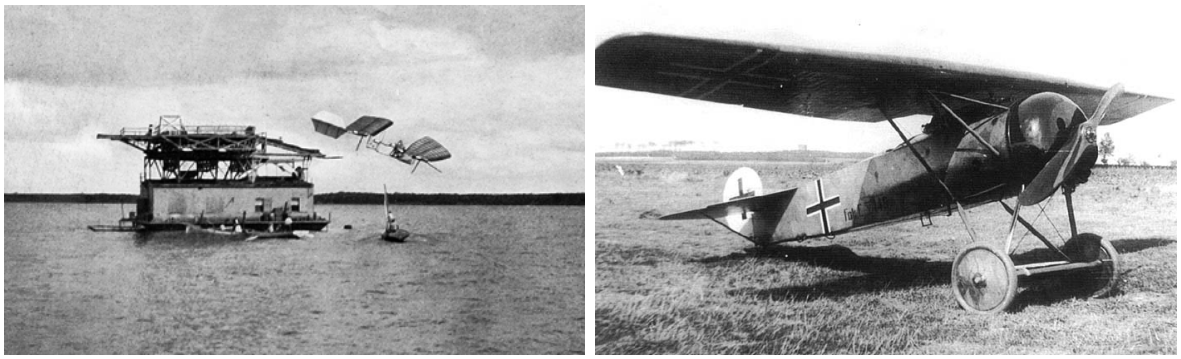

(a) Photograph of the Langley machine instants before its crash.

(b) Photograph of a Foker D8 aircraft.

Figure 1.2: Aircrafts featuring static aeroelastic problems. Credits: Wikipedia

As airplanes became more powerful, stiffer and faster, inertial forces started playing a role and aircraft designers were faced with a novel dynamic aeroelastic phenomenon: flutter. This phenomenon occurs when two or more natural frequencies of vibration of an aeroelastic system approach each other because of the wind loads and start exchanging energy between them and with the airflow, resulting in a exponential increase in vibration amplitude that usually leads to the loss of the aircraft. Figure 1.3 depicts a typical flutter case on an fundamental aeroelastic system with two modes of vibration. At wind-off conditions and below the flutter speed, the modes have well separated frequencies and positive damping ratios. As a result, the response of the system to non-zero initial conditions is a decaying oscillation (blue case). As the airspeed increases, the frequency gap between the modes decreases, the damping ratio of mode 1 increases and the damping ratio of mode 2 increases at first then decreases. When the airspeed reaches exactly the

system's linear flutter speed, the modal damping of mode 2 is exactly equal to zero (orange) and a constant amplitude oscillation can be observed. For any airspeed higher than that, the system features a negative damping ratio in mode 2 and a response amplitude that exponentially diverges as time passes is observed (red). One of the first observations of such phenomena is the elevator-fuselage flutter that occurred on the Handle Page 0/400 during World War I [5]. The problem was solved by connecting the two elevators to the same torque tube, suppressing the anti-symmetric vibration mode of the elevator. Nowadays, aircraft still undergo complex and expensive flight flutter test campaigns to certify that that no point of the flight envelope is closer than 80% (civil) or 85% (military) to the lowest flutter speed of the aircraft [6, 7]. Note that such phenomena are not limited to aircraft as long span bridges can also undergo, among other aeroelastic instabilities, flutter because of the combination of torsional and flexural modes [8–10].

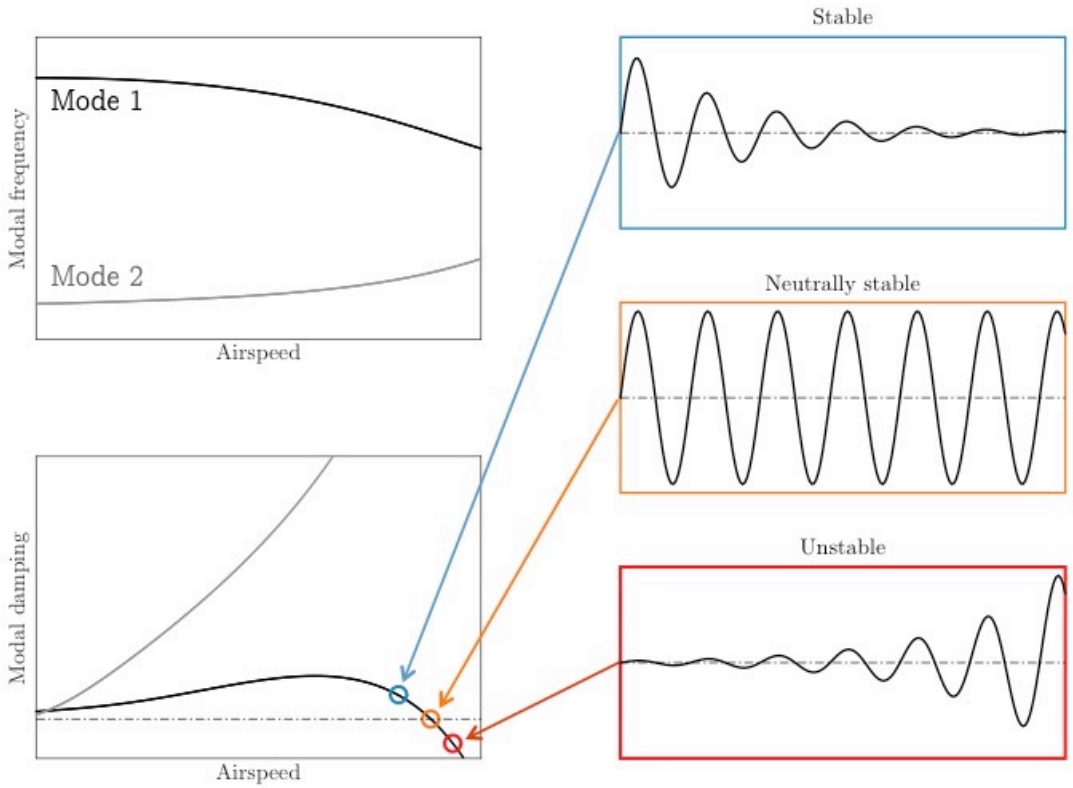

Figure 1.3: Linear flutter of a two-DOFs aeroelastic system

The fact that an aircraft is futter-free does not mean that it cannot undergo other, less dangerous aeroelastic instabilities. Nonlinearities present in the structure or in the air-

flow can indeed cause Limit Cycle Oscillations (LCOs) at airspeeds lower than the linear flutter speed of the system. Such LCOs can lead to structural failure, aircraft re-design, flight envelope limitations or increased maintenance. Four decades after the first flights of the F-16, the aircraft still undergoes LCOs during certain manoeuvres at certain flight conditions with certain payloads that are most likely the result of aerodynamic missile - wing interactions, transonic effects and nonlinear friction in the bolted connections but which are still not fully understood. On the other hand, the F-18 (figure 1.4) aircraft suffers from vertical tail buffeting during certain high angle of attack manoeuvres because the fundamental frequency and location of vortices generated by the plane's leading edge extensions coincides with that of the fins. Flutter is not limited to wings and control surfaces as skin panels flutter and LCOs can also be observed in numerous cases, most often in supersonic flight conditions. The clamping conditions of the panels usually introduce a hardening nonlinearity that limits the amplitude of the oscillations but can also lead to buckling when thermal effects are considered, which may significantly reduce the instability onset speed and cause chaotic oscillations because of snap-through phenomena. Depending on the amplitude and duration of the phenomena, panel LCO can result in structural failure. For instance, this phenomenon was judged dangerous for the X-15 aircraft and required a stiffening of the structure [11] but, on the other hand, it was judged non-destructive on Saturn V's third stage because the amplitude and duration of the vibrations were not critical enough to cause structural failure [12]. In this case, hardening nonlinearities can have a beneficial effect because they limit the amplitude of the oscillations but panel buckling due to thermal stresses can also decrease the onset speed of the instability and require particular attention. A backlash or freeplay nonlinearity also caused the loss of a F-117 stealth aircraft during an airshow in 1997 [13]. The aircraft took off without any issue after the maintenance crew forgot to tighten four of the right aileron's bolts, then a large amplitude LCO occurred during a particular manoeuvre and the wing broke into pieces, resulting in the loss of the aircraft.

1.2 State of the art in nonlinear aeroelasticity

As briefly introduced earlier, linear and nonlinear flutter can totally destroy aeronautic structures and should be avoided at all costs. As a result, it has received a lot of attention in the scientific community. This section presents an overview of the beneficial and detrimental effects that nonlinearities can have on the aeroelastic response of aircraft and introduces many nonlinear terms that are used in the thesis. The ultimate goal of this thesis is the study of dynamic absorbers, which are highly sensitive to the system's natural frequencies and far less sensitive to the system's damping ratios. As a result, the

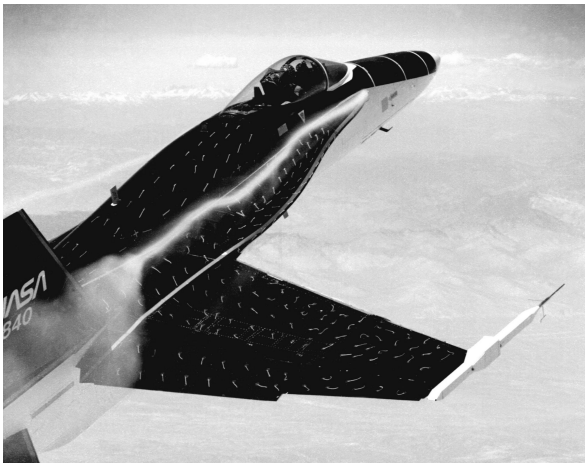

Figure 1.4: Photograph of a F-18 aircraft at high angle of attack with smoke generators showing the leading edge vortex breakdown on the vertical tail. Credits: NASA Photo

accent is put on stiffness nonlinearities rather than damping nonlinearities.

1.2.1 Linear flutter

If linear flutter remains a challenge in complex structures, the basic theory is now well understood and the aeroelastic response of simple 2-DOF (degree of freedom) or 3-DOF systems or of simple continuous wings is very well described in several good textbooks [14–18].

Figure 1.5 plots the bifurcation diagram (LCO amplitude variation with airspeed) of a typical linear aeroelastic system. At airspeeds lower than U_F, the linear flutter speed of the system, the modal damping of all the modes is positive and the response to a perturbation is a decay to a **stable fixed point**, which is a static equilibrium of the equations of motion that can attract a response trajectory. At the airspeed U_F, a degenerate Hopf bifurcation occurs, the fixed point becomes **unstable**, the modal damping of one of the modes is exactly equal to zero and circles whose amplitudes depend on the initial conditions are observed. At any airspeed larger than the flutter speed, a diverging response is observed. Note that linear flutter only exists mathematically as nonlinear phenomena such as stall, hardening/softening nonlinearities or structural failure will always affect the amplitude of the oscillations in real life applications.

1.2.2 Nonlinear aeroelasticity

The presence of nonlinearities in the structure or in the airflow significantly affects the aeroelastic response of the system. Depending on the nature of the nonlinearities, they can

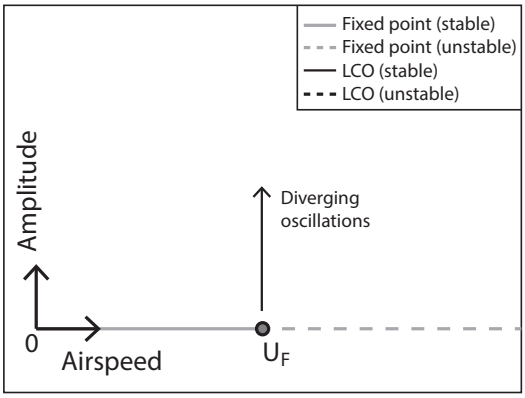

Figure 1.5: Typical bifurcation diagram of a linear aeroelastic system

lead to LCOs at airspeeds lower than the system's linear flutter speed but also usually limit the amplitude of the response compared to linear flutter. In this section, a non exhaustive review of the relevant nonlinearities is discussed along with the dedicated studies.

Smooth nonlinearities

Continuous nonlinearities were first considered for their simplicity and because they represent geometric nonlinear phenomena associated with large displacements. Figure 1.6 depicts typical hardening and softening smooth nonlinearities. The restoring force is hardening when an increase in amplitude leads to an increase in the slope of the restoring force and therefore to an increase in instantaneous frequency or softening when it is the opposite. Many authors investigated such nonlinearities on systems with pitch and plunge DOFs, starting with Woolston et al. in 1955 [19] using an experimental apparatus and analog computers and McIntosh et al. in 1981 [20], who designed an apparatus than can feature many different types of linearities by changing simple elements, including continuous hardening. These first studies focused on the onset speed of the LCOs rather than on their amplitude variation with airspeed. Then, the Texas A&M department designed the Nonlinear Aeroelastic Testbed Apparatus (NATA), a system that uses cams and wires to generate any desired continuous nonlinearity [21–23] and Abdelkefi et al. [24] obtained very good experiment/mathematical model agreement on a system with cubic and quadratic stiffness. Price et al. [25] also demonstrated that hardening systems can undergo smooth LCOs in a wide airspeed range but also aperiodic or chaotic oscillations at airspeeds above the system's torsional divergence speed because of a pitchfork bifurcation.

The response of systems with smooth nonlinearities was classified by Dowell as "good

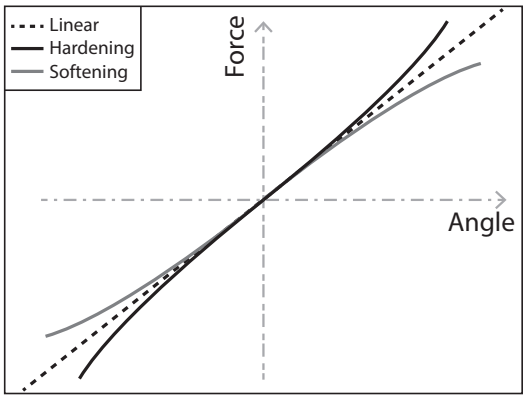

Figure 1.6: Typical smooth nonlinear restoring forces

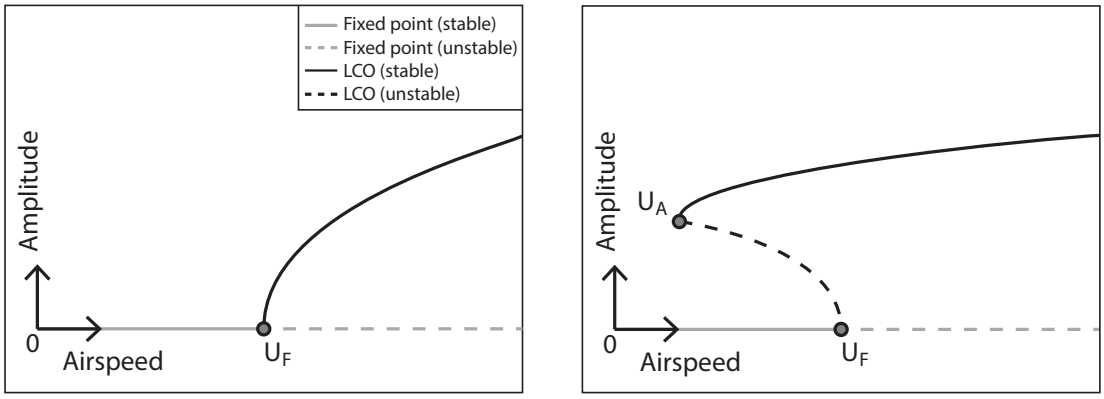

(a) Super-critical Hopf bifurcation

(b) Sub-critical Hopf bifurcation

Figure 1.7: Typical bifurcations diagrams observed with continuously nonlinear aeroelastic systems

LCOs" and "bad LCOs" [22]. Good LCOs (see figure 1.7(a)) arise at U_F, the linear flutter speed of the system (i.e. the flutter speed of the underlying linear system), because of a **supercritical Hopf bifurcation** and propagate in the increasing airspeed direction. As a result, at airspeeds below the Hopf speed, the response of the system to non-zero initial conditions will always decay to a **fixed point** and at airspeeds above the flutter speed, the response of the system to non zero initial conditions will stabilise to a LCO. In this case, the nonlinearity has a beneficial effect on the system since it does not induce any LCO at airspeeds below the flutter speed but limits the amplitude at higher airspeeds.

Bad LCOs (see figure 1.7(b)) arise at U_F because of a **sub-critical Hopf bifurcation** and propagate in the decreasing airspeed direction then usually change direction because of a **fold bifurcation** at an airspeed U_A. The branch that emanates from the Hopf bi-

furcation is usually unstable and becomes stable after the fold. As a result, below the airspeed U_A, the response of the system decays to the fixed point irrespective of the initial conditions. At airspeeds between U_A and U_F, the system can undergo LCOs or decay to the fixed point depending on the initial conditions and at airspeeds above U_F only LCOs can be observed. The airspeed region between U_A and U_F is referred to as a **bi-stable region** because LCOs can be observed depending on the initial conditions. Due to the sub-critical nature of the Hopf bifurcation, LCOs can be observed at airspeeds smaller than the system's Hopf point. As a result, the limiting airspeed is U_A, the **LCO onset speed**, which is the smallest airspeed at which LCOs can be observed.

The origin of such supercritical and subcritical phenomena can be explained by looking at the system's natural frequencies variation with airspeed. Figure 1.3 plots an aeroelastic systems' modal frequency variation with airspeed. Linear flutter is observed at an airspeed U_F because of the combination of mode 1 and mode 2. If mode 1 is hardening and/or if mode 2 is softening, an increase in amplitude would tend to separate the natural frequencies of the system irrespective of the airspeed and no LCO can be observed below the linear flutter speed. As a result, the system would behave as in figure 1.7(a), i.e. only fixed point solutions exist between airspeeds 0 and U_F. Above the linear flutter speed of the system, the nonlinearities tend to stabilise the system and LCOs are observed. Conversely, if mode 1 is softening and/or mode 2 is hardening, an increase in amplitude at airspeeds lower than the flutter speed would reduce the frequency gap between the modes and may cause LCOs at airspeeds smaller than the flutter speed. As a result, bifurcation diagrams similar to that displayed in figure 1.7(b) can be observed. Between airspeeds of 0 and U_A, the frequency gap is large enough to avoid flutter irrespective of the amplitude. Between airspeeds of U_A and U_F, the natural frequencies of modes 1 and 2 are close but not enough to flutter. If the amplitude is increased, the frequency gap is decreased and LCOs can occur. For airspeeds above U_F, linear flutter has occurred and only LCOs can be observed. In real life applications, there usually are more than two modes and a hardening nonlinearity on mode 1 might lead to sub-critical LCOs because of the coalescence of this mode with another mode of higher frequency and the same phenomenon may happen with mode 2 and a softening nonlinearity.

Non-smooth nonlinearities

Freeplay nonlinearities feature a bi-linear stiffness which is zero within the freeplay gap of width 2δ and non-zero outside (see figure 1.8). If the freeplay spring is placed in parallel with a linear spring, the full restoring force is bilinear and while a "freeplay" or "flat spot" restoring force is considered when the structural stiffness is equal to zero inside the

freeplay gap. Such bilinear restoring forces can be studied by de-coupling the system into two linear sub-systems. The underlying linear system is the system whose response lies within the freeplay boundaries while the overlying linear system is the system with full stiffness, when the freeplay gap width is equal to zero, i.e. when the aircraft performs in a normal way.

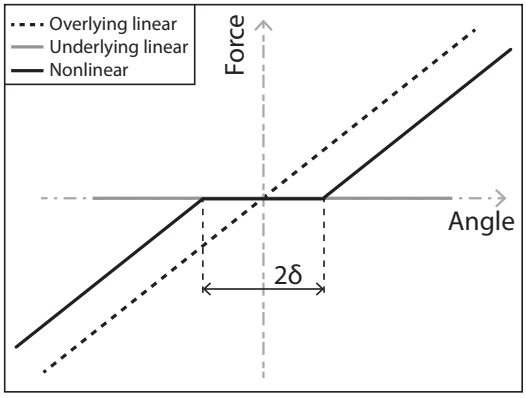

Figure 1.8: Typical freeplay nonlinear restoring forces

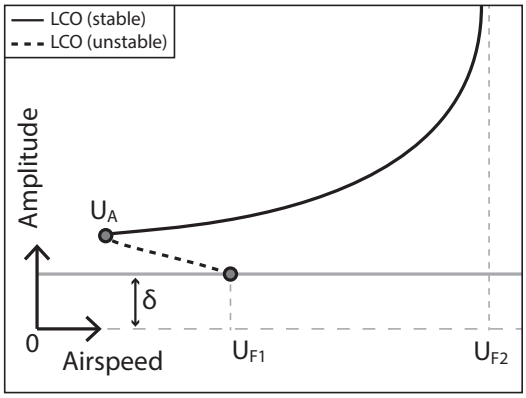

Figure 1.9: Typical bifurcations observed in systems with freeplay in pitch

Figure 1.9 depicts a sub-critical bifurcation characteristic of symmetric wing section with pitch and plunge degrees of freedom and with freeplay in pitch. At $U_{F,1}$, the flutter speed of the underlying linear system, three unstable LCO branches emanate from a **grazing bifurcation**. Two of these branches are highly asymmetric and investigated in detail in chapter 5 and in [26] on a similar system while the amplitude variation with airspeed of the symmetric branch is depicted in figure 1.9. The small amplitude highly asymmetric limit cycles are referred to as two-domain LCOs and orbit around points lying just outside the two boundaries while the large amplitude LCO is referred to as a three-domain

LCO and orbits around zero. After the bifurcation, an unstable LCO branch propagates in the decreasing airspeed direction until airspeed U_A where a fold bifurcation occurs, which changes the branch stability and propagation direction. Then, the LCO amplitude increases smoothly with airspeed and asymptotically becomes infinite at $U_{F,2}$, the flutter speed of the overlying linear system. Note that for such phenomena to occur, the underlying linear system's flutter speed must be smaller than that of the overlying linear system. One of the major differences between systems with freeplay and systems with smooth nonlinearities is that, since LCOs can only be observed on nonlinear systems, the first limit cycle that emanates from the bifurcation cannot have an amplitude equal to zero as it must enter and exit the freeplay region.

Such nonlinearities usually lead to LCOs at airspeeds lower than the linear flutter speed of the overlying linear system, which makes them potentially dangerous. As a result, the FAA authorities place very strict limits on the amount of freeplay allowed in aircraft control surfaces (see [27]) and a lot of research has been devoted to this subject, usually on simple systems featuring 2 or 3 DOFs.

Some of the first studies where conducted by Woolston et al. [19] and by McIntosh et al. [20] on pitch and plunge wings with freeplay in pitch. The authors focused on the onset speed of the instability. Yang et al. [28] studied the whole branch using the Harmonic Balance method. Hauenstein et al. [29], Price et al. [25], Liu et al. [30] and Chung et al. [31] then demonstrated numerically and experimentally the existence of aperiodic oscillations, most likely because of the coexistence of several stable fixed points. Experiments performed by Marsden et al. [32] with various freeplay gaps demonstrated that the LCO amplitude depends linearly on the width of the freeplay gap and that the smaller the gap, the higher the LCO onset speed. The authors concluded that this increase in LCO onset speed with small freeplay gaps was due to nonlinear bearing damping.

Systems with a higher complexity but still freeplay in pitch were then considered. Chen et al. [33] observed the co-existence of chaos and LCOs on a pitch-plunge wing with freeplay in pitch and with an external store. Tang et al. [34] combined the ONERA stall model [35] on a helicopter blade with freeplay in pitch and with a flap DOF. They observed that chaos was dominant at small amplitude with the freeplay model and at high amplitude with the stall model. Flexible control surfaces with freeplay in pitch were used by Kim et al [36] and Tang et al. [37,38]. The authors observed that the flexibility of the surface has a significant effect on the linear flutter behaviour of the system but does not affect much the system's response when freeplay is also considered. The latter authors also observed

that the LCO onset speed increases with the aerodynamic preload, which led Chen et al. [39] to state that the military freeplay specifications are too strict after a similar study on a F-16 model with freeplay in the control surfaces.

The effect of freeplay in the control surface was investigated by many researchers using the typical aeroelastic surface [40], a rigid 2D wing featuring pitch, plunge and control surface deflection DOFs with freeplay in the control surface. Theoretical models and experiments were used to understand the aeroelastic response of the system, which features complex branches that appear and disappear [40–42] but also to validate numerical methods used to tackle aeroelastic problems and the discontinuities inherent to freeplay [43–47]. One of the major differences between this system and those with freeplay in pitch is that the underlying linear system features not one but three stability changes, two of which are due to plunge-control surface flutter and the third is due to pitch-control surface flutter. As a result, the system features two branches of limit cycles that are able to interact with each other, resulting in complex behaviour.

Subsonic aerodynamic nonlinearities

The main source of subsonic aerodynamic nonlinearities is separation of the airflow. Such separation usually occurs around bluff bodies or around streamlined bodies at high angles of attack. Depending on the geometry of the objects, this separation of the airflow can lead to several types of aeroelastic instabilities. Galloping and vortex induced vibration (VIV) are translational instabilities that occur in a direction perpendicular to that of the mean airstream. Separated airflows usually have a natural frequency, which is related to the Strouhal number. In the case of galloping, the fluid's natural frequency is usually higher than that of the structure and the instability, whose amplitude increases with airspeed once the critical airspeed has been reached, is due to a negative damping provided by the airflow. Vortex induced vibration (VIV) on the other hand, occurs when the shedding frequency of the Von Karman vortices is close to one of the translational natural frequencies of the structure. In that case, a coupling between the fluid and the structure can occur, resulting in a lock-in phenomenon and large amplitude LCOs in a given airspeed range. Slender civil engineering structures such as bridges, cables and tall towers are typically prone to such instabilities however, they are usually not encountered in aerospace structures because they are streamlined. Stall flutter, on the other hand, is a rotational instability due to dynamic stall, which can occur on buff bodies but also on streamlined bodies such as wings or helicopter blades at high angle of attack. As a result, it has received much more attention in the aerospace community. Owing to the high complexity of the involved phenomena, a lot of research has been conducted on dynamic

stall, which is an unsteady aerodynamic phenomena occurring under forced motion, but not so much on stall flutter, which is an aeroelastic phenomenon involving the coupling of dynamic stall with the dynamics of a flexible structure. Note that unlike all the non-linearities investigated above, flow separation can cause instabilities on systems featuring a single structural mode.

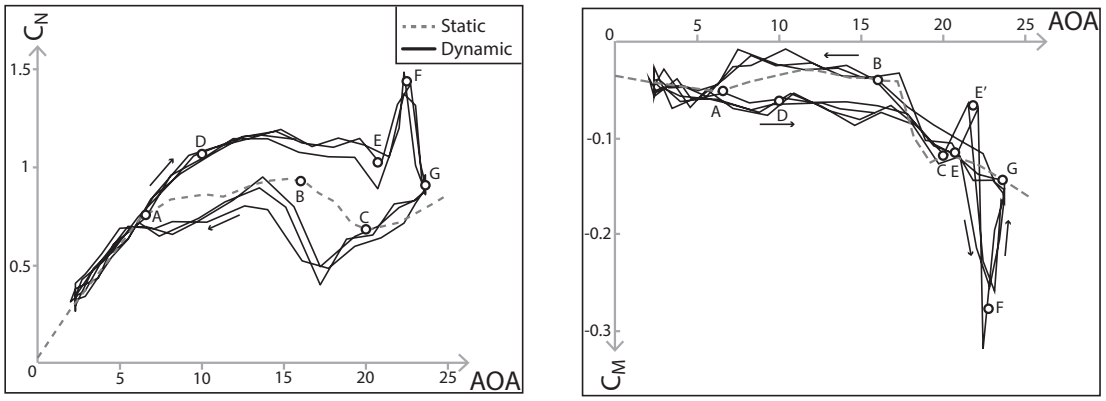

(a) Normal force coefficient

(b) Pitching moment coefficient

Figure 1.10: Static and dynamic normal force and pitching moment of a S809 profile undergoing a dynamic stall test

Figure 1.10 depicts the variation of the normal force coefficient (force perpendicular to the wing), C_N, and pitching moment coefficient around the quarter chord, C_M, with angle off attack (AOA) of a S809 wind turbine blade, obtained from the National Renewable Energy Laboratory (NREL) [48]. The grey curves correspond to static tests while the black lines correspond to dynamic tests performed by continuously varying the AOA between 2° and 24° at a reduced frequency $k = \omega b/U = 0.0335$, where ω is the forcing frequency, b is the half-chord and U is the airspeed. Unlike the static measurements, the dynamic data feature hysteresis and the path indicated by the arrows corresponds to an AOA that is equal to 2°, increases to 24° and eventually decreases back to 2°.

The static normal force increases linearly with the pitch angle up to AOA = 6° (A), the static stall angle, then slowly varies up to AOA = 16° (B), drops until AOA = 20° (C) and increases smoothly with the AOA at higher angles. The smooth load variation with AOA above the stall angle is due to the thickness and to the "whale" shape of the airfoil profile, which induces a separation from the trailing edge that slowly reaches the leading edge as the AOA is increased. Thinner profiles such as the widely studied NACA 0012 lead to a more abrupt stall (see the work of McAlister, Mcroskey et al. for instance [49–51]).

The moment coefficient is relatively low at small angles because the moment is measured around the wing's quarter chord. At AOA = 6° (A), stall occurs and the moment starts to increase with the AOA. Right after point (B), the moment starts to drop because the aerodynamic center moves towards the trailing edge of the wing.

The dynamic test results are quite different from the static ones and three key phenomena inherent to dynamic stall are observed: stall delay, leading edge vortex (LEV) and re-attachment. In the dynamic case, the lift increases linearly with the AOA up to AOA = 10° (D) before stall begins to saturate the lift force. This phenomenon, known as stall delay, can be due to viscid (see McCroskey [52]) and inviscid boundary layer (see Ericsson and Reding [53]) contributions and can lead to maximum aerodynamic loads much higher (approximately 25% in this case) than predicted using steady data. Between AOA = 10° and AOA = 21°, the separation point moves towards the wing's leading edge and a leading edge vortex (LEV) starts forming. At AOA = 21° (E), the separation point reaches the leading edge of the wing and the LEV detaches from the wing, is convected downstream and creates a strong suction effect that greatly increases the aerodynamic load. At AOA = 23.4° (F), the LEV is at the trailing edge of the profile and leaves the wing, which leads to a rapid decrease of its effect. At 24°, the LEV is already far enough from the wing to have a negligible effect. The width of the LEV-induced peak is directly dependent on the reduced frequency and its strength induces maximum normal forces 58% higher than the static predictions. When the AOA decreases, re-attachment starts to occur at an angle that is different from the stall angle and that lies between 6°, the static stall angle, and 10°. Unlike the stall angle which is approximately the same at each cycle, the re-attachment angle is different from one cycle to the next but remains within a bounded space.

Those three dynamic stall phenomena are also observed on the moment curves. Even though those data are nosier than the normal force ones, point D appears to be aligned with the static curve owing to the stall delay phenomenon. The LEV is shed at point E, increases the moment at first because it is located in front of the quarter chord (point E′) then leads to a large drop in moment as its strength and distance from the quarter chord increases. The dynamic moment is around twice as high as the static predictions. When the angle decreases, the moment increases to values similar to the static ones and the re-attachment process begins.

Combining dynamic stall with a linear flexible structure with, for instance, pitch and plunge DOFs can cause stall flutter which leads to bifurcation diagrams similar to those

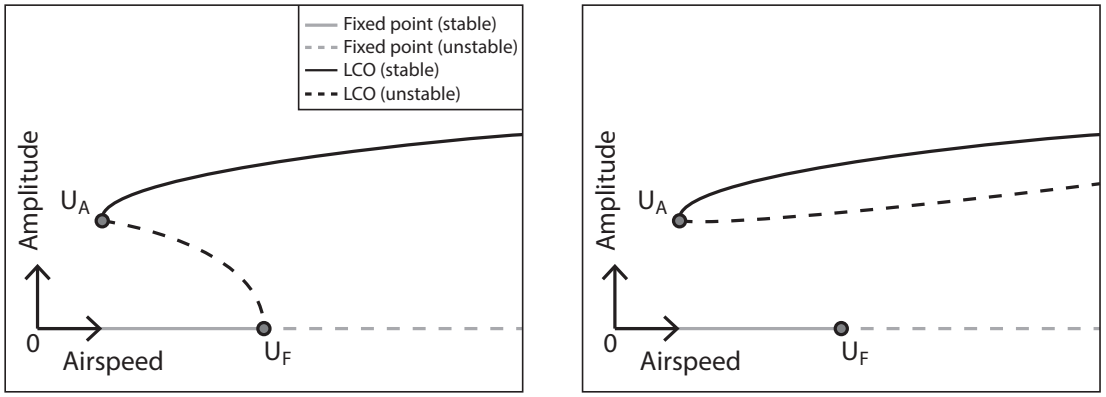

(a) Branch connected to a Hopf

(b) Isolated branch

Figure 1.11: Typical bifurcations observed in nonlinear systems undergoing stall flutter

depicted in figure 1.11. At airspeeds smaller than U_A, the aerodynamic loads are not sufficient to cause stall flutter irrespective of the initial conditions imposed on the wing. At airspeeds between U_A and U_F (the linear flutter speed of the system), large enough initial perturbations can cause LCOs while small initial perturbations lead to decaying responses. At airspeeds above U_F, linear flutter has occurred, the fixed point is unstable and the amplitude of the oscillations increases until it stabilises on a limit cycle. In this case, the stall phenomena have a beneficial effect because they limit the amplitude of the oscillations, which would diverge if linear aerodynamics were considered. In figure 1.11(a), the LCO branch is connected to the Hopf point associated with the system's linear flutter speed and a sub-critical Hopf bifurcation is observed while in figure 1.11(b), the LCO branch is not connected to the Hopf point and is referred to as an **isolated solution branch** or **isola**. Stall flutter can of course also occur on systems with other additional nonlinearities, resulting in complex bifurcation behaviours combining the branches of figure 1.11 with smooth or non-smooth nonlinearities (figures 1.7 and 1.9) that lie underneath the stall flutter branches.

Because of the complexity of stall flutter phenomena, full aeroelastic studies are usually limited to simple wings with few DOFs. The ONERA dynamic stall model, introduced by Tran et al. [35] has been coupled to flexible structures by several authors. Tang et al. [34, 54] performed experiments and computations on a helicopter blade, achieved a good experiments - model correlation and observed that chaos could arise at sufficiently high LCO amplitudes. Dunn et at [55] studied numerically and experimentally the response of a cantilever wing with a NACA0012 profile and focused on the effect of the mean angle of attack of the wing on the reponse. Dimitriadis and Li [56] performed experiments

on a NACA 0012 airfoil and observed that fixed points, symmetric LCOs, and strongly asymmetric LCOs could co-exist depending on the airspeed. The authors also observed that all limit cycles demonstrate a certain amount of cycle-to-cycle variability, probably because of the non-repetitive nature of the re-attachment phenomenon. They also observed the travel of the leading edge vortex by means of pressure transducers. Similar experiments performed by Abdul Razak et al. [57] on a NACA 0018 airfoil with pitch and plunge DOFs highlighted that the higher (in absolute value) the mean pitch angle, the lower the stall flutter airspeed but also the smoother the LCO amplitude variation with airspeed. They also observed that the LCO frequency of wings undergoing stall flutter is closely related to that of the linear flutter speed of the same system, which suggests that the two phenomena are linked.

1.3 Vibration mitigation techniques

1.3.1 Active control

The basic principle of active flutter control consists in measuring the aircraft's response in real time and applying a feedback force in order to increase the flutter speed or decrease the LCO amplitude. Figure 1.12 depicts a typical control loop where a controller records the system's accelerations and velocities and applies an input force on the system, usually thanks to minijets, piezoelectric actuators or control surfaces. Thorough introductions into the subject are available in Dowell et al. [17] and Wright and Cooper [18]. Most modern aircraft feature Flight Control Systems (FCS) that integrate some sort of feedback using accelerometers or gyroscopes and control surface deflections in order to enhance the flying qualities or the gust response of the aircraft however these systems are not designed to affect the structural modes and the flutter properties of the aircraft, probably because it is not permitted by the airworthiness regulation authorities and because a failure in the system would result in the loss of the aircraft. Nevertheless, active flutter control has been widely studied by the scientific community using numerical models, wind tunnel experiments and even flight tests. The goals of these studies were mainly to demonstrate the potential of the technique, to compare the performance of different control lows and to test various methods of applying control forces.

The most straightforward way of applying control forces is using the aircraft's existing control surfaces, which means that it might be feasible to implement such active control systems without significant modifications of the structure. Borglund et al. [58] and Yu et al. [59] achieved an increase in flutter speed of 50% and 13.4%, respectively, numerically

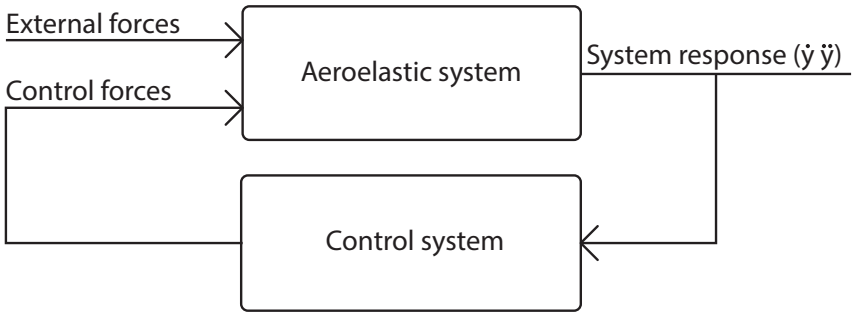

Figure 1.12: Block diagram of an aeroelastic system with a control loop

and in the wind tunnel. The former authors nevertheless suspect that the very good performance of their control system is due to a weak flutter mechanism. Mukhopadhyay [60] used the PAPA (Pitch And Plunge Apparatus) in a transonic wind tunnel and achieved an increase in critical airspeed of at least 20% (wind tunnel limitations did not allow to test at sufficiently high airspeeds). Huang et al. [61] studied the effect of time delay in the control loop. The authors showed numerically that an increase in flutter speed of 19% with a sufficiently fast controller can be achieved but also that a controller whose response is too slow can decrease the system's flutter speed. Sensburg et al. [62] performed flight tests on a F4 Phantom fighter jet and were able to increase the aircraft's flutter speed by 16%. Nevertheless, three backup flutter suppression mechanisms were implemented to guarantee the safety of the test.

Piezoelectric actuators can also be used to apply the necessary control forces. In this case, the aeroelastic control loop does not interact with the FCS. Han et al. [63] achieved an increase in flutter speed of between 6 and 11% depending on the control law and Moses [64] performed wind tunnel tests on a 1/6 scale model of a F-18 undergoing tail buffeting. Piezoelectric actuators and control surface actuators both led to a decrease in root RMS (root mean square) amplitude of about 60%.

1.3.2 Passive control via structural aircraft modifications

To this day, no active control solution has been approved for use on aircraft by airworthiness regulation authorities and the only possibility to increase the flutter speed of an aircraft is a structural re-design of the components that interact to cause the instability. Generally, flutter can be avoided by increasing the stiffness of the structure (at the cost of increased weight) or by reducing the coupling between the relevant structural modes. This can be done either by adding masses at certain strategic locations or by displacing the elastic axis of the structure. The former method, called mass balancing, is often used for

control surfaces. An example of control surface masses is depicted in figure 1.13. With the increasing amount of composite materials used in aerospace structures, aeroelastic tailoring, which consists in optimizing the composite structure while taking aeroelastic contraints into account, is another potential technique for flutter speed optimisation [65].

Figure 1.13: Photograph of the balancing masses on the control surfaces of a Messerschmitt 110 aircraft. Credits: Wikipedia

Usually, increasing the modal damping of the system may also increase the flutter speed and/or reduce the LCO amplitude. Cunha et al., for instance, tested numerically the effect of viscoelastic materials in a sandwich configuration to mitigate panel flutter [66]. Malher et al., on the other hand, used a shape memory alloy on a 2-DOF aeroelastic apparatus in order to introduce hysteretic dissipation, resulting in increased flutter speed and decreased LCO amplitude [67, 68].

1.3.3 Passive control via dynamic absorbers

Yet another option to mitigate LCOs, which is investigated in detail in this thesis, is the use of dynamic absorbers. Figure 1.14(a) depicts a generic 1-DOF system, called the primary system, with a dynamic absorber made of a mass attached to the primary system by means of linear or nonlinear stiffness and damping couplings. Depending on the couplings chosen, very different properties can be obtained. Such absorbers have received a lot of attention in the civil and mechanical engineering communities however very few studies are available for aircraft flutter suppression. Table 1.1 summarises all the absorbers considered in this literature review and their stiffness and damping properties.

	Classical mass dampers	
Absorber	Stiffness force	Damping force
LTVA (Frahm) [69]	Linear	-
LTVA [70–74]	Linear	Linear
Cubic NES [75–83]	Purely cubic	Linear
Damping NES [84]	Linear	Quadratic
Impact NES (VA) [85]	Impact	Impact
Hysteretic TMD [86]	Hysteresis	Hysteresis
NLTVA [87–92]	Linear + Polynomial	Linear
	Special mass dampers	
Membrane NES [93]	Grounded cubic	Linear
LTVA + Impact [94]	Linear + Impact	Linear + Impact

Table 1.1: Summary of the dynamic absorbers used in the literature

Linear absorber

A Linear Tuned Absorber (LTVA) also called Tuned Mass Damper (TMD) is obtained when the absorber mass is connected to the primary system using a linear spring and dashpot. Introduced by Frahm in 1911 [69] and upgraded by Ormondroyd in 1928 [70], this absorber is capable of splitting a large amplitude resonance peak of the primary system's frequency response function (FRF) into two small amplitude peaks, provided its natural frequency and damping ratio are tuned in accordance to those of the primary system. The equal peaks method, approximated by Den Hartoog and Brock [71, 72] and derived in an exact form by Asami [73], allows to rapidly tune the absorber's stiffness and damping. This absorber provides a large amplitude reduction however a very accurate tuning of the stiffness is required and the LTVA is only effective on one mode while the structure might feature several potentially dangerous modes. Moreover, in the presence of structural nonlinearities, the change in natural frequency of the primary system with amplitude of oscillation can be sufficient to detune the absorber, thus greatly reducing the resulting dissipation. TMDs are widely used in high towers and bridges for vortex-induced-vibration (VIV) or human-induced vibration [95–100]. Bridge torsion-flexure flutter has also been considered by Gu et al. [9]. The authors showed mathematically and in the wind tunnel that an increase in flutter speed of 40% was achievable with TMDs weighing 5.6% of the total mass of the bridge. Kwon et al. [101], performed a similar study however many TMDs with smaller masses were considered rather than one or two absorbers. The authors showed that by optimising the natural frequencies and damping

ratios of the smaller absorbers, it is possible to increase the robustness of the system. Another example demonstrating the performance of the TMD can be found in formula one. Such absorbers were fitted on the Renault R26 car at the end of the 2005 season to mitigate the vibrations induced by the kerbs, thus increasing the mechanical grip and downforce consistency on the car's front and back ends. They were then banned in the middle of the 2006 season, after other teams failed to achieve Renault's performance and complained to the international automobile federation.

Even though they are effective in a narrow frequency band, such absorbers can increase the flutter speed of 2-DOF systems by a large amount. The first aeroelastic study, conducted by Karpel [102] in 1981, demonstrated that an increase in flutter speed of 62% could be achieved using an absorber weighing 20% of the total mass of the system however, as in mechanical engineering, a small change in the absorber's or in the primary system's natural frequency led to a large decrease in performance. The absorber was tuned by computing the variation of the flutter speed of the coupled system with absorber natural frequency and damping ratio, i.e. by trial and error. A LTVA made of a RLC (resistance, inductance, capacitance) resonant shunt circuit with piezoelectric materials was also considered by Moon et al. to mitigate panel flutter [103]. The authors computed a reduction in LCO amplitude of 30% to 60% but were not able to increase the onset speed of the instability.

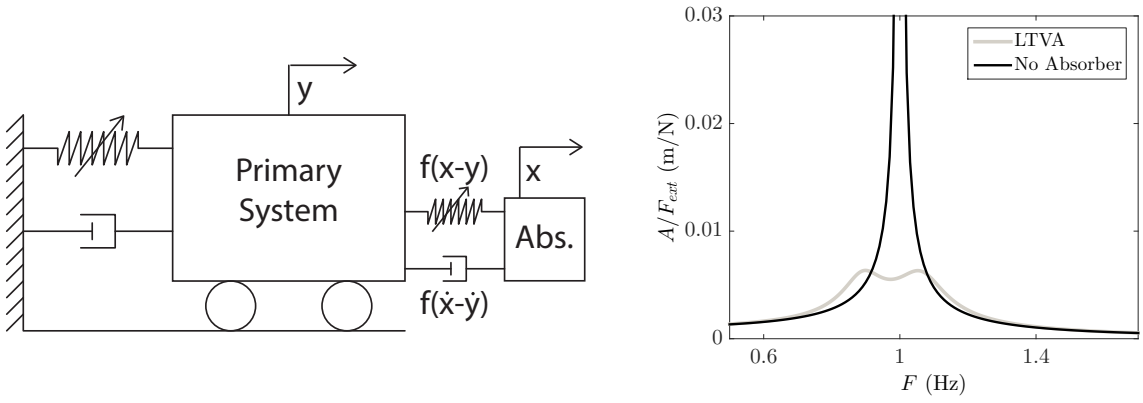

(a) Schematics of the system

(b) FRF of the system

Figure 1.14: Archetypical linear 1-DOF system with a LTVA

Classical nonlinear energy sink

As the natural frequency of aeroelastic systems usually varies with flight condition and oscillation amplitude and since flutter is the result of the combination of two or more modes, it might be tempting to use an absorber featuring a linear damping force (for simplicity) and a purely cubic stiffness force. This absorber, which is referred to as a classical Nonlinear Energy Sink (classical NES), has been introduced by Roberson and studied by many authors in the mechanical engineering community ever since [75–80, 83]. The absorber is capable of pumping energy out of a mode using Targeted Energy Transfer (TET) but, more importantly, it offers a broadband dissipation while the LTVA is only able to dissipate energy in a narrow frequency band. As a result, the NES is also widely studied in civil engineering for earthquake protection [104, 105]. The drawback of such absorbers is that their performance is amplitude-dependent and a threshold is usually required to achieve good performance.

Aeroelastic studies have been performed using such an absorber by Lee et al. [80–82] on the NATA system both numerically and experimentally. The authors showed an increase in flutter speed of about 3% numerically and 26% experimentally as well as a great reduction in LCO amplitude with NES weighting between 10% and 12.5% of the mass of the primary system. Hubbard et al. [83] demonstrated numerically and experimentally an increase in LCO onset speed of about 6% on a swept wing in the transonic regime using an absorber with a mass of only 1% of the total mass of the wing.

As mentioned earlier, the stability of a nonlinear system at very low oscillation amplitudes is identical to that of an underlying linear system, i.e. the Hopf bifurcation flight condition of the nonlinear system is coincident with the flutter speed of the underlying linear system. As a result, it is possible to demonstrate that the NES can never outperform the LTVA in increasing the Hopf point airspeed using equivalent linearisation [106]. Assuming an aeroelastic system similar to that sketched in figure 1.14(a) undergoing a LCO described by the DOF y at a frequency ω and a NES undergoing a displacement x, the relative displacement between the absorber and the primary system can be approximated using a sinusoidal assumption

$$x - y = A\sin(\omega t) \tag{1.1}$$

where A is the amplitude of oscillation and ω its frequency. The resulting NES restoring force, F_{NES}, is given by

$$F_{\mathrm{NES}} = k_3(x - y)^3 \tag{1.2}$$

where k_3 is the cubic restoring force coefficient which has been optimally tuned. Substituting equation 1.1 into equation 1.2, using trigonometric identities and neglecting the third harmonic (equivalent linearisation) yields

$$\begin{aligned} F_{NES} &= k_3 A^3 \sin^3(\omega t) \\ &= \tfrac{1}{4} k_3 A^3 \left[3\sin(\omega t) - \sin(3\omega t)\right] \\ &\approx \tfrac{3}{4} k_3 A^3 \sin(\omega t) \\ &\approx \tfrac{3}{4} k_3 A^2 (x - y) \end{aligned} \tag{1.3}$$

which means that for any LCO inducing a relative NES-primary system displacement of amplitude A, the NES's restoring force can be approximated by a linear restoring force of equivalent linear stiffness $k_{eq} = \frac{3}{4} k_3 A^2$. As a result, at the flutter point, since it is reasonable to assume that A is very small, the NES behaves like a LTVA without stiffness, i.e. it can only be tuned in damping. In contrast, an LTVA can also be tuned in stiffness and therefore it will always outperform a NES in increasing the flutter speed.

Other nonlinear dynamic absorbers

Other types of nonlinear absorbers were also considered in the literature. Poovarodom et al. [84] used an absorber with linear stiffness and purely quadratic damping, corresponding to the drag of a plate immersed in a liquid, because it is easier to build than a LTVA. They showed that a performance similar to that of a LTVA can be obtained in a civil engineering case. Lacarbonara et al. [86] considered hysteretic forces and showed that they were able to provide additional dissipation compared to a LTVA. Ema et al. [85] considered an impact damper where most of the dissipation came from the contact between a mass and mechanical stops. This absorber was able to increase the damping in the system by a factor of 10 but again is probably not effective in delaying linear flutter because a minimum amplitude is required to trigger the NES. Collette et al. [94] countered the problem by attaching the impact damper to a linear absorber. As a result, the system behaves like a LTVA at small amplitude and like a coupled LTVA - impact damper at larger amplitude. Bellet et al. [93] also considered a NES made of a membrane coupled linearly to the primary system but with a grounded nonlinear restoring force in order to damp low frequency sound waves. Such complex NESs have not been investigated in the aeroelastic literature yet.

Nonlinear tuned vibration absorber

As stated earlier, the LTVA is very effective in a narrow frequency band while the classical NES is not effective in delaying the Hopf point but dissipates energy in a wide frequency band. Combining a classical NES with a LTVA results in a nonlinear tuned vibration absorber (NLTVA) which offers better robustness than the LTVA and better low amplitude performance than the classical NES. The NLTVA was probably introduced by Robertson et al. in 1952 [87] who used it on a linear primary system to extend the frequency band where the absorber is effective. Many other studies followed on Duffing primary systems which consist of a linear 1-DOF oscillator with a cubic stiffness in parallel to the linear stiffness [88–92, 107]. These studies showed that in the presence of a hardening or softening nonlinearity, the LTVA can be effective at low forcing amplitude but detuned when the forcing amplitude is increased. The addition of a NLTVA whose nonlinearity mimics the nonlinearity of the primary system can counter the effects of the nonlinearity in the primary system and greatly improve the absorber performance [92]. Figure 1.15 plots the FRF of a 1-DOF Duffing oscillator with LTVA (grey) and NLTVA (black) at 4 different forcing amplitudes. At low level (figure 1.15(a)), the linear and nonlinear absorbers perform identically because the nonlinearity in the primary system is not effective. Then, the higher the forcing amplitude, the higher the detuning and the larger the difference in performance between the LTVA and the NLTVA (figures 1.15(b) to 1.15(d)).

The NLTVA was first tested in aeroelasticity by Habib et al. [108]. The authors used a Van der Poll-Duffing 1-DOF oscillator to mimic an aeroelastic system featuring a super-critical bifurcation and LCOs. They demonstrated that a LTVA was effective in increasing the LCO onset speed but turned the super-critical bifurcation into sub-critical. By adding a nonlinear restoring force, they could restore the super-criticality and decrease the LCO amplitude. Similar results were obtained by Malher et al. [109] on more realistic systems featuring pitch and plunge DOFs and hardening nonlinearities in pitch.

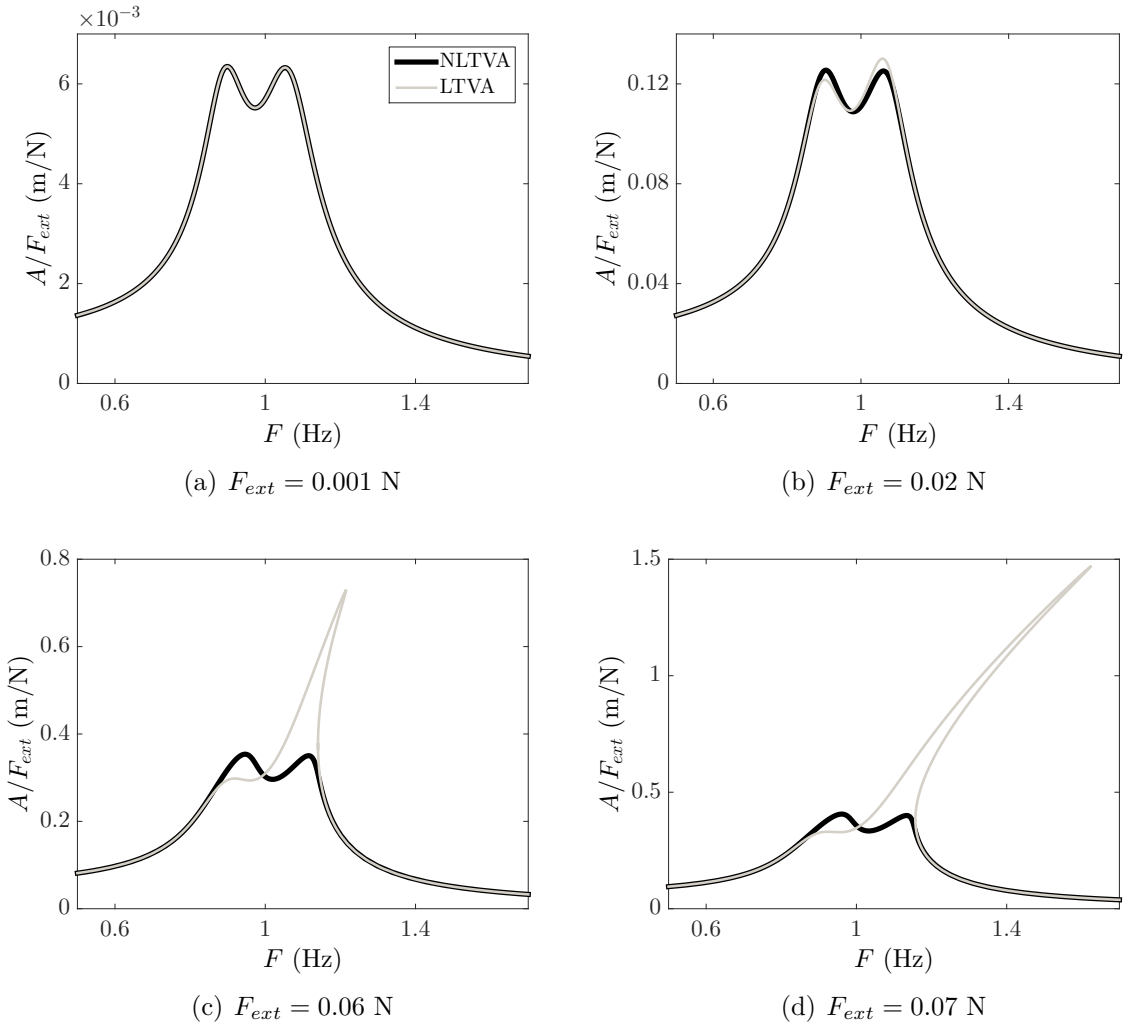

(a) $F_{ext} = 0.001$ N

(b) $F_{ext} = 0.02$ N

(c) $F_{ext} = 0.06$ N

(d) $F_{ext} = 0.07$ N

Figure 1.15: Frequency response function of a Duffing oscillator with LTVA and NLTVA

1.4 Objectives of the thesis

Nonlinear aeroelastic phenomena occur in real life applications and usually have to be avoided for safety, performance and maintenance reasons. Such phenomena are usually linked to linear flutter, smooth nonlinearities, freeplay, transonic effects, stall or buckling. Dynamic absorbers have proven to be effective tools in order to dissipate energy in mechanical systems and civil engineering structures, however appart from a few pioneering studies, very little work has been carried out on the application of such absorbers on aircraft-like aeroelastic systems.

The goal of this thesis is to understand and demonstrate the performance of linear and nonlinear tuned mass dampers for flutter and LCO suppression. Two simple aeroelastic systems featuring different structural nonlinearities are investigated theoretically and experimentally.

The first system is made of a flat plate with pitch and flap DOFs and a structurally hardening nonlinearity in pitch. This system features one of the simplest aeroelastic responses possible and is therefore a good candidate for a first flutter suppression attempt. The system is first tested in the wind tunnel then modelled using simple aerodynamics. Subsequently, the mathematical model is used to investigate the performance of linear and nonlinear absorbers and to determine optimal tuning rules for the absorbers. Finally, the experimental apparatus is used again to demonstrate the performance of the absorber in the wind tunnel.

The second aeroelastic system is made of a rigid wing with pitch, plunge and control surface deflection DOFs with freeplay in the pitch DOF. This system features a much more challenging aeroelastic response featuring the co-existence of small and large amplitude LCOs in a given airspeed range, aperiodic LCOs and up to three fixed points, depending on the aerodynamic preload. A similar approach is followed: the system is tested in the wind tunnel, then a mathematical model is derived and used to investigate the performance of the absorbers. No experimental validation was performed for this system.

Chapter 2

Design, analysis and modelling of a pitch and flap wing

2.1 Introduction

In this chapter, a novel experimental aeroelastic setup with degrees of freedom in pitch and flap is proposed. Inspired by the wing designed by G.J Hancock in the eighties for teaching purposes [110], the system is made of a flat plate suspended from the roof of the wind tunnel of the University of Liège by means of a leafspring that provides a linear restoring force in flap and a continuously hardening restoring force in pitch. The advantage of this design is that it is simple, cheap and that is does not use any bearings. One of the goals of this experiment is to observe a super-critical Hopf bifurcation at the flutter speed of the system, which is usually not possible with bearings because they introduce nonlinear damping that is large at rest and small when the motion starts.

The chapter first presents the experimental apparatus. Then, static and dynamic identification of the linear and nonlinear parameters of the structural system is performed. Subsequently, aeroelastic results at pre-critical (below the flutter speed of the system) and post-critical (above the flutter speed of the system) conditions are performed. Finally, a simple mathematical model with two degrees of freedom and linear aerodynamics based on Wagner's theory [15] and strip theory [16] is proposed and compared to the experimental results.

2.2 Experimental setup

Installed in the large low-speed wind tunnel of the University of Liège, the experimental apparatus is based on Hancock's wing [110]. It is designed to achieve very low damping ($\approx 0.3\%$ at wind-off conditions) and flutter at an airspeed of around 12 m/s. To achieve such a low structural damping, the setup does not use any bearings or rotational springs. The pitch and flap restoring torques are provided by a specially designed leaf spring and a nonlinear clamp assembly. The complete Nonlinear Pitch and Flap Wing (NLPFW)

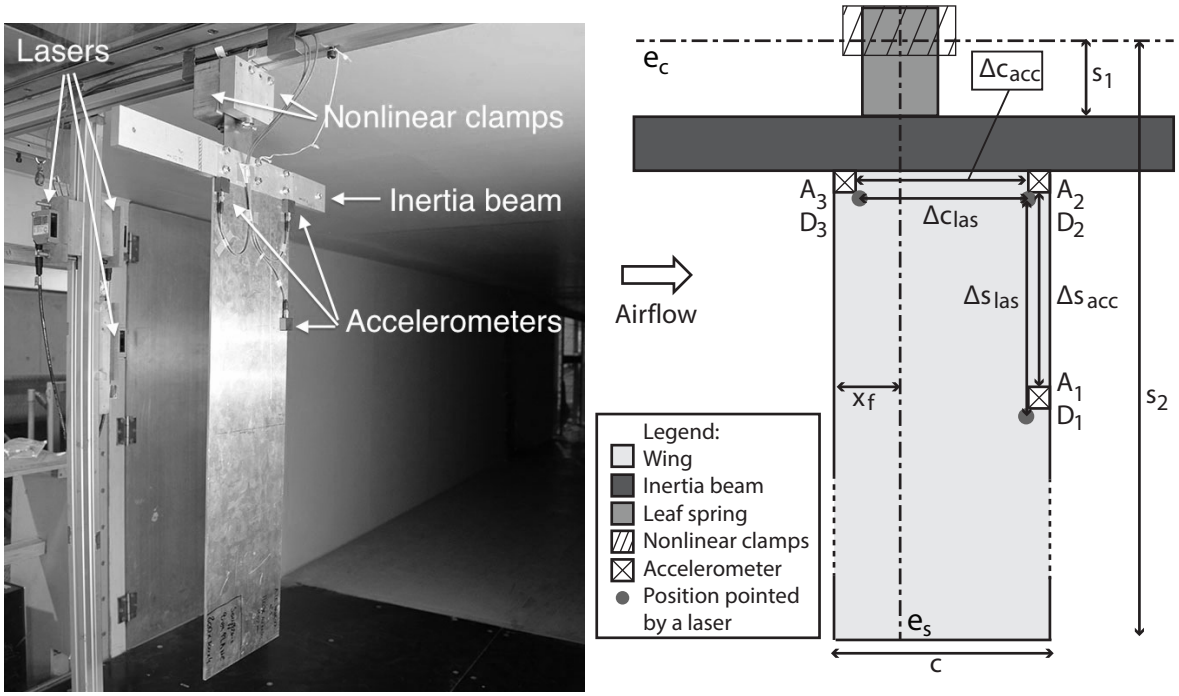

(a) Photo of the setup in the wind tunnel

(b) Diagram showing transducer locations and major components of the NLPFW

Figure 2.1: Experimental setup showing wing, support and transducers

is shown in figure 2.1. It is a stiff thin rectangular unswept aluminium flat plate with span $s = 800$ mm, chord $c = 200$ mm, thickness $t = 4$ mm and an aspect ratio of 4. It is supported at its root at $0.3c$ from the leading edge. As a result, it features two rigid DOFs: a pitch rotation θ and a flap rotation α, as shown in figure 2.2. The flexural axis, e_s, is parallel to the leading edge and passes by the hinge while the axis e_c is at a distance s_1 above the root of the wing. The stiffness in both pitch and flap is provided by a thin C75S steel leaf spring. It is 100 mm long, 70 mm wide and 0.7 mm thick. It is clamped linearly to the flat plate and nonlinearly to the roof of the test section of the wind tunnel. Figure 2.3(a) draws the geometry of the nonlinear roof clamps and figure 2.3(b) plots the nonlinear restoring torque of the pitch DOF. On the other hand, the flap stiffness is linear

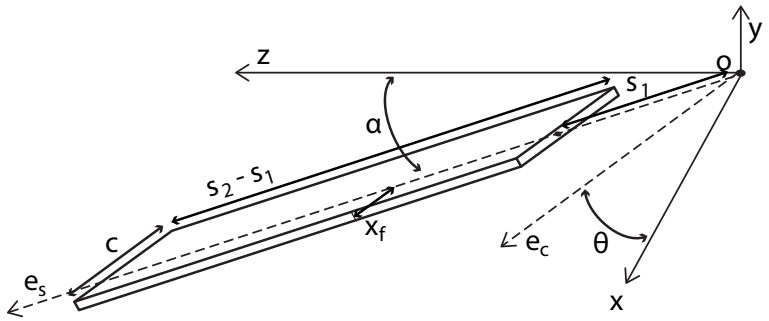

Figure 2.2: Schematic of the Hancock Wing

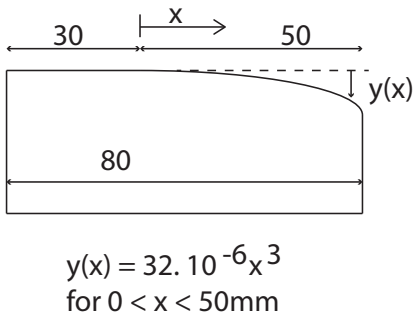

(a) Sketch of the two nonlinear roof clamps

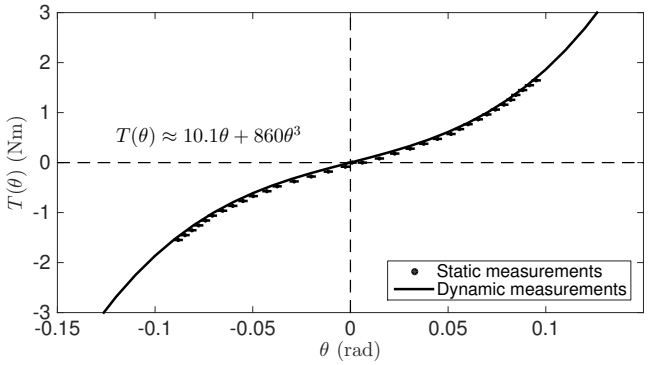

(b) Experimental restoring torque curve in the pitch DOF

Figure 2.3: Characteristics of the nonlinear clamps

in the displacement range considered.

Finally, a 500 mm × 50 mm × 15 mm aluminium beam is bolted at the junction between the flat plate and the leaf spring (see figure. 2.1). It increases the rotational inertia of the system and consequently decreases its flutter speed to the target speed range: [10-15] m/s. The wind-off characteristics are summarised in appendix C.

The displacements are measured by means of 3 laser displacement sensors with a sensitivity of 9.6 mV/mm and a range of 100-500 mm. The accelerations are measured using 3 MEMS DC accelerometers with a sensitivity of 100 mV/g and a range of ± 30 g. The position of the sensors is shown in figure 2.1(b). Accelerometers A_2 & A_3 and lasers D_2 & D_3 are placed at the root of the wing at a distance $\Delta c_{acc} = 180$ mm and $\Delta c_{las} = 168.5$ mm from each other while accelerometer A_1 and laser D_1 are located close to the trailing edge at a distance $\Delta s_{acc} = 200$ mm and $\Delta s_{las} = 205.5$ mm from sensor 2.

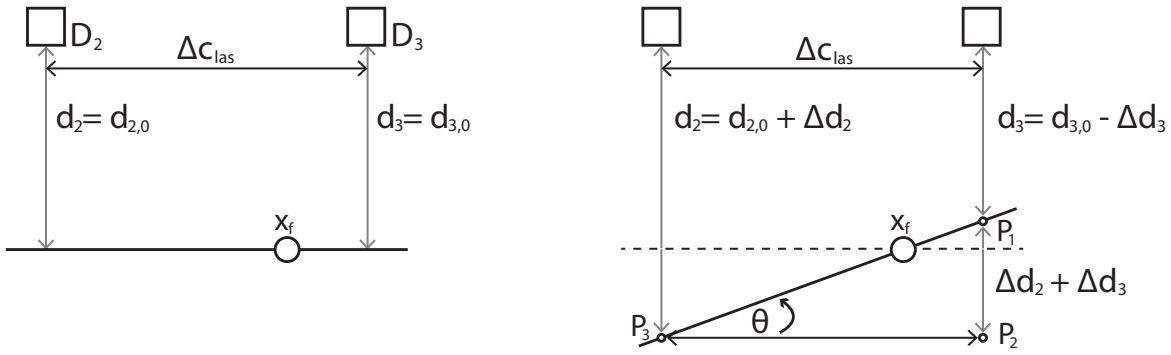

(a) $\theta = 0$ (b) $\theta \neq 0$

Figure 2.4: Pitch angle computation

The pitch displacements are computed from the response of lasers D_2 and D_3. Figure 2.4 depicts the system configuration for $\theta = 0$ and $\theta \neq 0$. Lasers D_2 and D_3 are located at a distance Δc_{las} from each other and respectively measure distances d_2 & d_3 given by

$$d_2 = d_{2,0} + \Delta d_2(\theta) \tag{2.1}$$

$$d_3 = d_{3,0} - \Delta d_3(\theta) \tag{2.2}$$

where $d_{2,0}$ & $d_{3,0}$ are the offset sensor distances measured at rest and Δd_2 & Δd_3 are the variations of measured distances due to to the wing's rotation around x_f. Subtracting Equations 2.1 and 2.2 yields the relative displacement due to the pitch angle θ

$$\Delta d_2 + \Delta d_3 = d_2 - d_3 - d_{2,0} + d_{3,0} \tag{2.3}$$

When $\theta \neq 0$, the points P_1, P_2 and P_3 form a right triangle in P_2 where $\overline{P_2P_3} = \Delta c_{las}$ and $\overline{P_1P_2} = \Delta d_2 + \Delta d_3$ and the pitch angle can be computed as

$$\theta = \text{ATAN}\left(\frac{d_2 - d_3 + d_{3,0} - d_{2,0}}{\Delta c_{las}}\right) \tag{2.4}$$

Conversely, as sketched in figure 2.5, the accelerometers move with the wing and always measure accelerations perpendicular to the surface of the flat plate. As a result, accelerometers A_2 & A_3 both measure accelerations a_2 & a_3 proportional to $\ddot{\theta}$, the angular acceleration in pitch and Δc_2 & Δc_3, the distances between each sensor and the

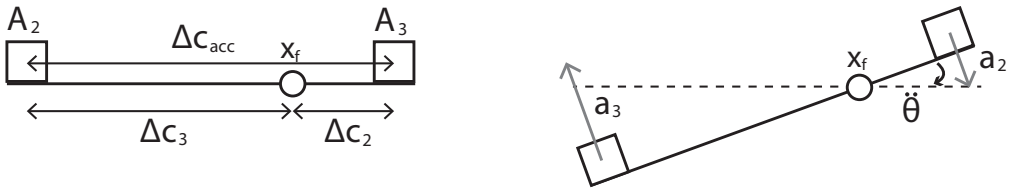

(a) $\ddot{\theta} = 0$ (b) $\ddot{\theta} \neq 0$

Figure 2.5: Pitch acceleration computation

flexural axis

$$a_2 = \Delta c_2 \ddot{\theta} \tag{2.5}$$

$$a_3 = -\Delta c_3 \ddot{\theta} \tag{2.6}$$

Subtracting equations 2.5 & 2.6, isolating $\ddot{\theta}$ and noting that $\Delta c_2 + \Delta c_3 = \Delta c_{acc}$, the pitch acceleration is given by

$$\ddot{\theta} = \frac{a_3 - a_2}{\Delta c_{acc}} \tag{2.7}$$

Following the same procedure, the flap displacements and accelerations are given by

$$\alpha = \arctan\left(\frac{d_2 - d_1 + d_{1,0} - d_{2,0}}{\Delta s_{las}}\right) \tag{2.8}$$

$$\ddot{\alpha} = \frac{a_1 - a_2}{\Delta s_{acc}} \tag{2.9}$$

The measured pitch angle and accelerations exactly correspond to those of the Hancock wing but the flap does not necessarily correspond. The presence of higher modes of the leafspring-wing assembly leads to relative displacements between sensors 1 and 2 that can be misinterpreted as a flap angle or as a flap acceleration in the sense of the Hancock wing but which are not (see sections 2.3 & 2.5.2). As a result, great care will be taken when considering flap measurements.

2.3 Wind-off identification

2.3.1 Linear identification

A roving hammer test was carried out to identify the first few linear modes of vibration of the structural system. The wing was impacted five times in 24 different locations using a hammer instrumented with a load cell. The response was measured with a single accelerometer placed on the trailing edge at the tip of the wing while the modal parameters were estimated from the Frequency Response Function (FRF) of the signal. Figure 2.6 depicts a typical system response and the corresponding FRF where six modes are clearly identified.

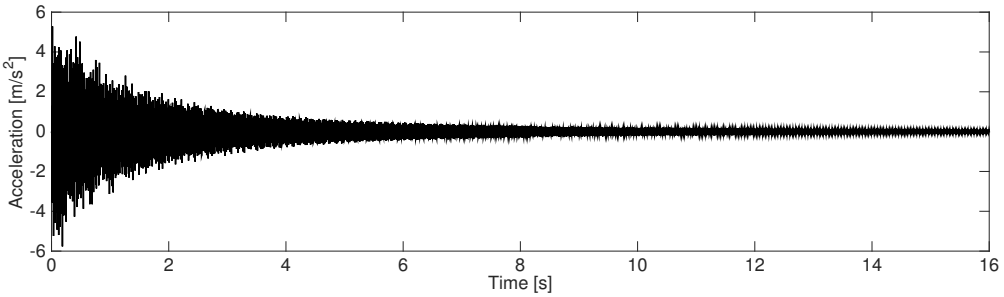

(a) Timeseries of a decay after a hammer hit

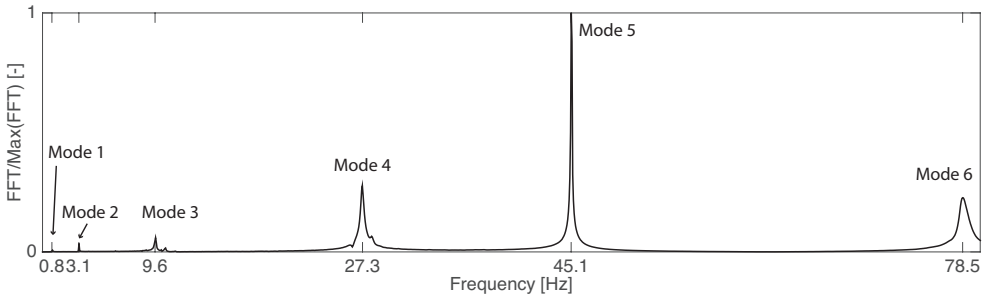

(b) FRF obtained from the accelerometer time response

Figure 2.6: Accelerometer time response and FRF used to perform linear wind-off modal analysis on the setup

	Mode 1	Mode 2	Mode 3	Mode 4	Mode 5	Mode 6
Frequency [Hz]	0.84	3.1	9.6	27.3	45.1	78.5
Damping ratio [%]	0.84	0.24	0.40	0.35	0.06	0.39

Table 2.1: Modal frequencies and damping ratios of the NLPFW

Since it is very difficult to excite the leaf spring with the hammer, its modal shapes are estimated from a shell element model of the whole structure computed by means of the Finite Element package SAMCEF. The first six modes of the complete system are depicted in figure 2.7 and their frequencies and damping ratios, identified using the Half-Power method, are given in table 2.1. The system's modes of vibration can be described as follows:

1. Mode 1: first flexural mode of the leaf spring and no deformation of the flat plate. It is dominated by α, the flap DOF of the Hancock wing. The response of all three sensors should be in phase when this mode is excited.

2. Mode 2: first torsional mode of the leaf spring and no deformation of the flat plate. It mostly involves θ, the pitch DOF of the Hancock Wing. The response of sensors 1-2 should be in phase while the response of sensors 1-3 and 2-3 should be out of phase when this mode is excited.

3. Mode 3: second flexural mode of the leaf spring and first flexural mode of the flat plate. The response of all the sensors should be in phase when this mode is excited but, in contrast to the flap mode case, sensor 1 should measure larger accelerations/displacements than sensor 2. The effect of the deflection of the wing is so small compared to that of the deflection of the leaf spring that this mode could be approximated by a rigid plate with a combination of a flap DOF and a plunge DOF.

4. Mode 4: second flexural mode of the leaf spring and second flexural mode of the flat plate. The response of sensors 2-3 should be in phase while that of sensors 1-2 and 1-3 should be out of phase.

5. Mode 5: first torsional mode of the flat plate. It is not possible to differentiate this mode from mode 4 with the sensor setup used in this study.

6. Mode 6: second flexural mode of the leaf spring and third flexural mode of the flat plate.

Considering the mode shapes, the pitch angle defined in section 2.2 is mostly due to mode 2, which is the only one that leads to significant relative displacement between sensors 2 and 3. Conversely, the flap angle can be a combination of the displacements of modes 1, 3, 4, 5 and 6 and great care should be taken when comparing this angle to the predictions of the model of the Hancock wing, which only represents mode 1.

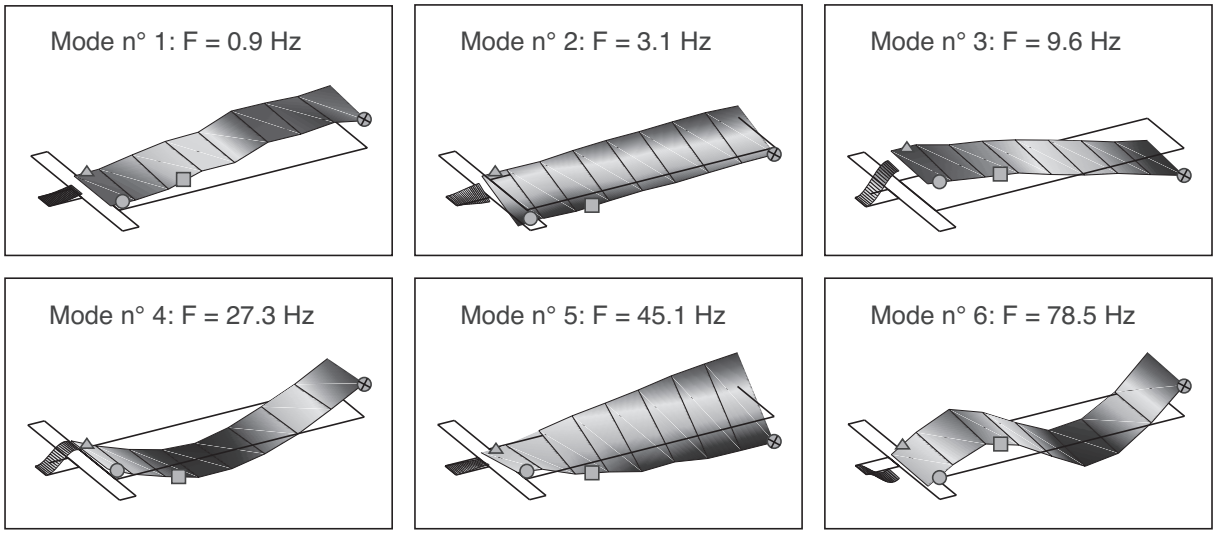

Figure 2.7: First six mode shapes of the NLPFW. The squares indicate the positions of sensors A_1 & D_1, the circles A_2 & D_2 and triangles A_3 & D_3. The crossed circle indicates the position of the accelerometer used for the roving hammer test.

2.3.2 Nonlinear identification

Nonlinear identification was performed on the flap and pitch modes using large amplitude free-decay tests in order to measure the frequency and damping amplitude dependence of the pitch and flap modes.

Figure 2.8 plots the response of the flap DOF after an initial condition $\alpha_0 \approx 10$ deg and the Wavelet Transform [111] of the response, which indicates the response frequency variation with time. Despite the large amplitude variation during the decay, the frequency remains approximately constant, which suggests that the stiffness in flap is linear in the displacement range considered.

Figure 2.9 depicts the response of the pitch after an initial condition $\theta_0 \approx 6$ deg and the Wavelet Transform of the response. This time, the frequency of the oscillations is initially close to 4 Hz and decreases smoothly to 3.09 Hz, the linear frequency of the pitch mode, as the amplitude of the motion is reduced. This response is typical of a system with hardening stiffness.

Relating the frequency of the modes to the oscillation amplitude yields the frequency backbones of the nonlinear modes. Figure 2.10(a) plots the flap and pitch frequency backbones of the system computed from the time series of figures 2.8(a) & 2.9(a). The black markers are obtained by computing the amplitude and the instantaneous frequency

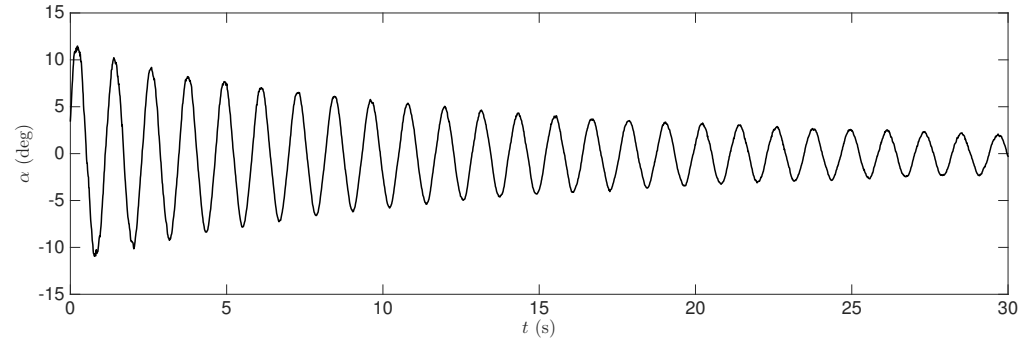

(a) Signal decay

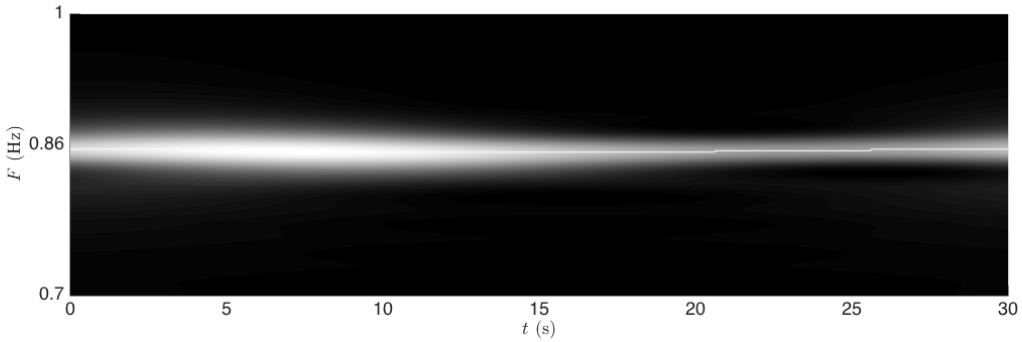

(b) Frequency variation with time

Figure 2.8: Flap free-decay and corresponding frequency backbone

using a Peak-Picking routine while the grey markers are computed using a Hilbert transform and a Wavelet transform. The flap mode has a frequency of 0.86 Hz irrespective of the flap response amplitude while the pitch mode has a frequency that starts at around 3.09 Hz, the frequency of the linear pitch mode, and increases to 4 Hz at 6 deg of pitch amplitude. The Peak-Picking routine leads to more scattering because of the noise in the data but provides information at higher amplitude because both the Wavelet and the Hilbert transforms suffer from transient effects at the beginning of the signal. This figure illustrates the fact that the flap frequency can be measured from any signal amplitude while the pitch linear frequency should be estimated using signals with amplitudes as low as possible. Moreover, the nonlinearity tends to increase the difference between the frequencies of the pitch and flap modes.

Figure 2.10(b) plots the damping backbone of the system computed from the time series in figures 2.8(a) & 2.9(a). The markers are obtained using the logarithmic decrement technique [112] while the dashed lines are obtained by fitting an exponential curve to the Hilbert transform of the response. Assuming the response of the pitch and flap modes is

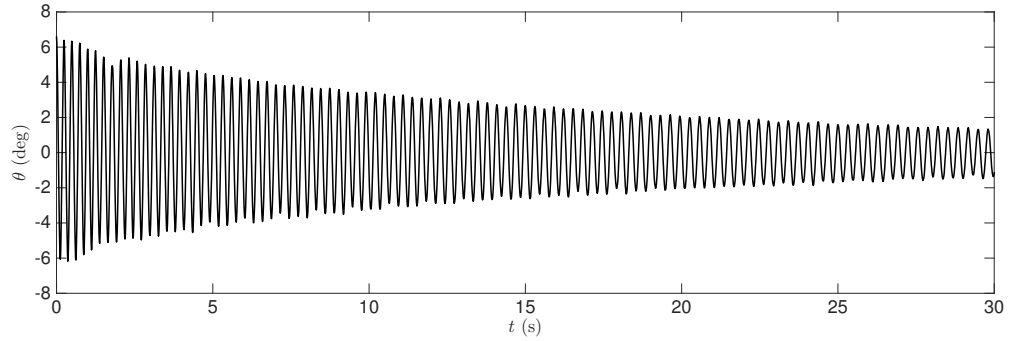

(a) Signal decay

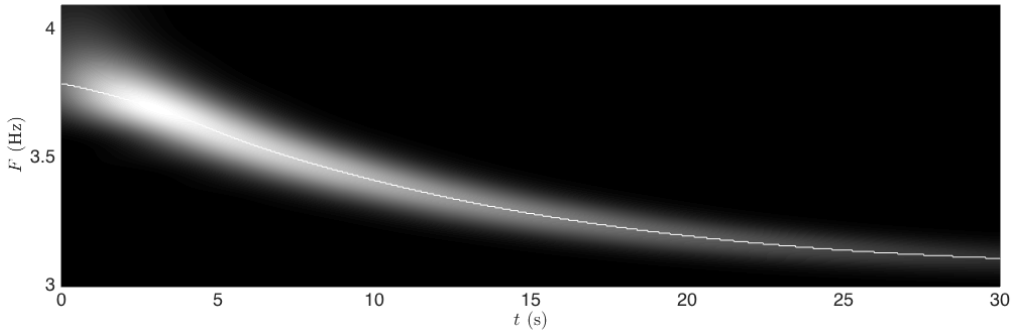

(b) Frequency variation with time

Figure 2.9: Pitch free-decay and corresponding frequency backbone

de-coupled, the time variation of either DOF can be approximated as

$$x(t) \approx X_0 \times \sin(\omega_x t) \times e^{-\zeta_x \omega_x t} \tag{2.10}$$

where x corresponds to either α or θ, X_0 is an initial condition, ω_x is the undamped frequency and ζ_x is the damping ratio. Computing the norm of the Hilbert transform of a signal provides the envelope of the response

$$||\text{Hilbert}(x)|| \approx X_0 \times e^{-\zeta_x \omega_x t} \tag{2.11}$$

and performing an exponential fitting of this envelope provides the term $\zeta_x \omega_x$. Computing ω_x from a FFT (and neglecting the frequency variation with amplitude) finally allows to isolate ζ_x. This simple method provides an estimate of the damping over the whole decay and requires an estimation of the frequency from another method. Note that more advanced methods using the Hilbert transform to compute the frequency and damping backbone exist (see for instance [26]), however they use the phase of the signal and are sensitive to noise, which is usually high during wind tunnel experiments. The logarithmic

decrement technique, on the other hand, leads to noisier measurements than the proposed fitting of the response's Hilbert transform but does not assume that the frequency is constant and allows to compute a damping backbone by plotting the damping ratio of each cycle against its amplitude.

The pitch damping does not vary much with the amplitude and both techniques predict a damping ratio of 0.24%. Conversely, the flap damping is equal to 0.84% for amplitudes between 2 and 3 degrees, then increases for higher flap angles. The exponential fitting method measures a damping of 1.15%, i.e. in the middle of the backbone, which is consistent with the fact that it provides a global picture of the response. The nonlinear damping phenomenon is probably due to drag forces that vary quadratically with the flow speed which is, for a wind-off test, related to the amplitude of the oscillations. Nevertheless, in LCO conditions, the flap amplitudes are smaller than 3 degrees and the damping can be considered to be linear.

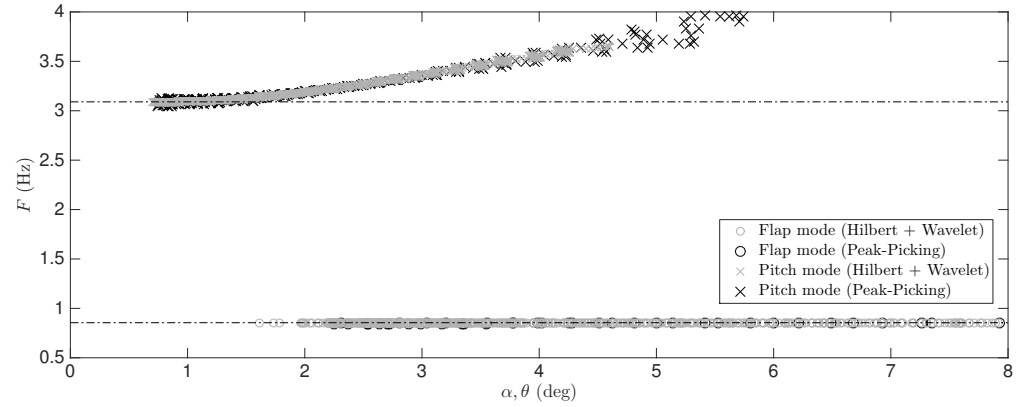

(a) Frequency backbone

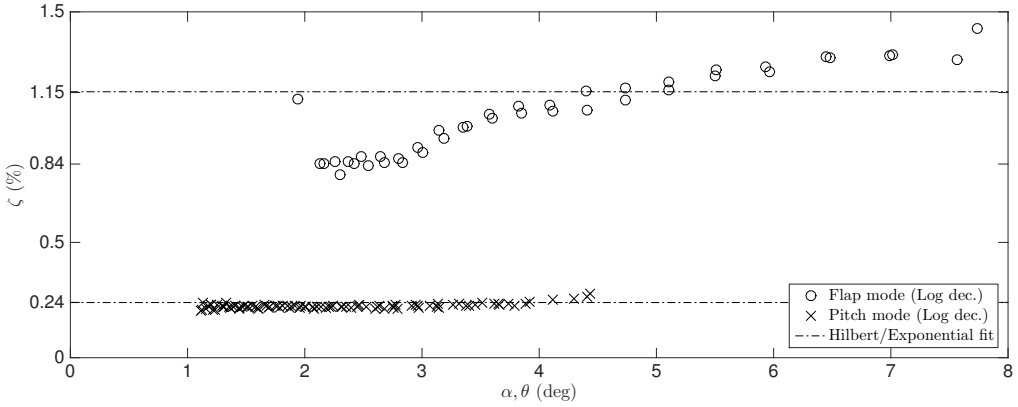

(b) Damping backbone

Figure 2.10: Experimental frequency and damping backbones of the NLPFW

2.4 Pre-critical aeroelastic investigation

A pre-critical aeroelastic investigation is performed in order to study the pitch and flap linear frequency and damping variation with airspeed. The procedure, similar to that used for the nonlinear identification, consists of releasing the system from an initial pitch and flap angle at as many stabilised airspeeds as possible and carrying out identification on the measured response. Figure 2.11 depicts pitch and flap decays at 6.2 m/s (top) and 10.5 m/s (bottom). Comparing the two cases shows that the airflow tends to increase the flap damping and to decrease the pitch damping in this velocity range but no conclusion can be drawn yet on the effect of the wind on the frequencies.

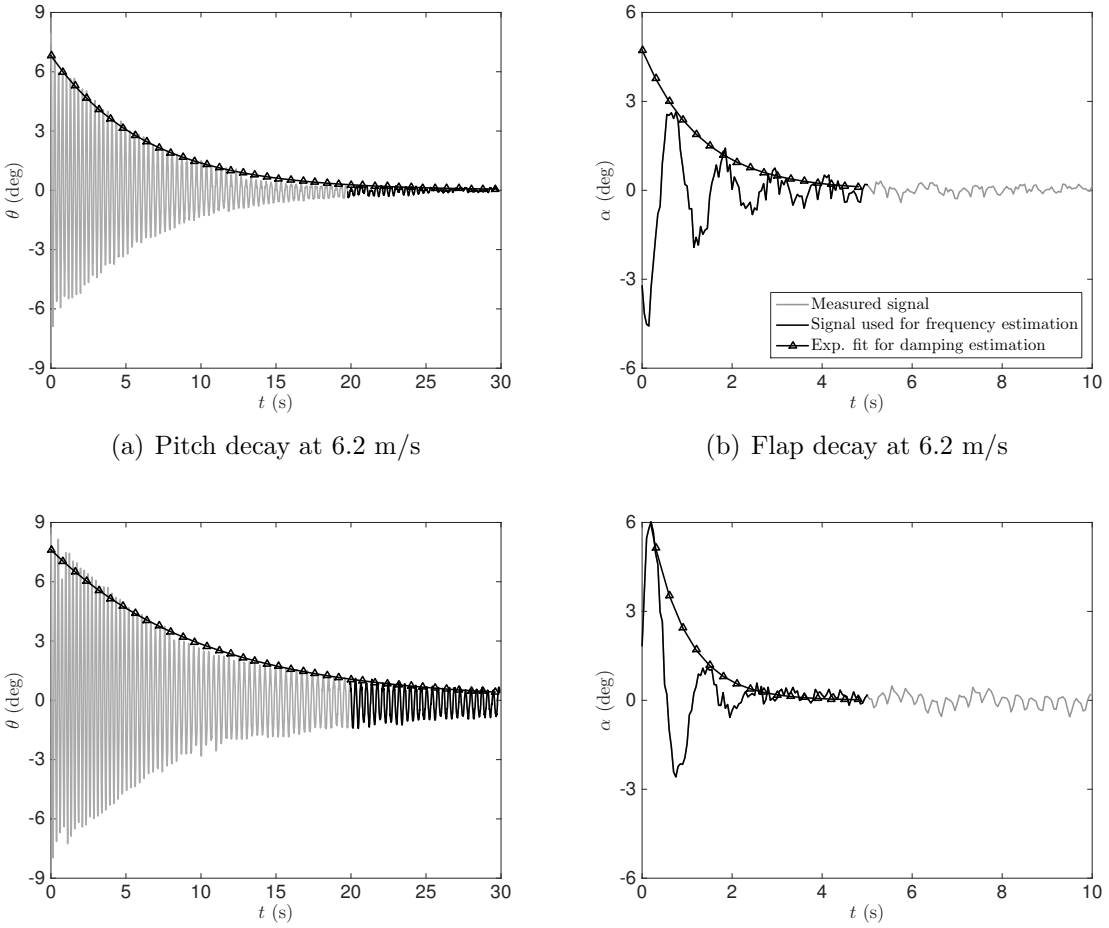

(a) Pitch decay at 6.2 m/s

(b) Flap decay at 6.2 m/s

(c) Pitch decay at 10.5 m/s

(d) Flap decay at 10.5 m/s

Figure 2.11: Time series of the pitch and flap free decay responses at airspeeds of 6.2 m/s and 10.5 m/s. The legend applies to all 4 subplots.

The frequency of the oscillations is computed from the free decays of figure 2.11 us-

ing both Fast Fourier Transform (FFT) and Wavelet Analysis. The last 10 seconds of the pitch response signals were used to estimate the frequency in order to minimise the effect of the nonlinearity on the frequency. Conversely, the first 5 seconds of the flap responses were used in the curve fits because as the damping in flap is quite high, the motion decays very quickly. The damping was estimated using three methods: an exponential curve fit of the Hilbert Transform of the responses, an exponential curve fit of the amplitude peaks of the responses, and the logarithmic decrement technique.

Computing the damping and the frequency at several stabilised airspeeds yields the curves displayed in figure 2.12. In figure 2.12(a), the error bars indicate the resolution of the FFT. In figure 2.12(b) the error bars indicate the 95% confidence bounds of either the exponential fit of the Hilbert transform or of the peaks of the signal, or the standard deviation of the logarithmic decrement, depending on which method gives the largest error bars. The curves are typical of aeroelastic systems: the pitch damping rate increases with the airspeed. It reaches its maximum at 8.3 m/s then decreases until it becomes zero and flutter occurs. On the other hand, the damping of the flap mode increases continuously. The flap frequency is approximately constant while the pitch frequency decreases until the modes can interact to cause flutter. The scattering of the damping measurements is due to the high damping. The aerodynamic damping was indeed so high that the system could only undergo two or three oscillations before going back to rest.

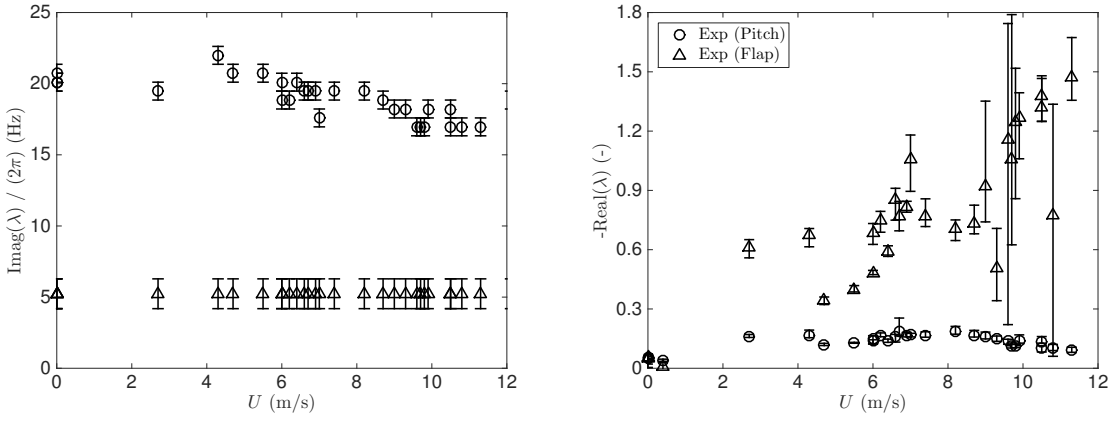

(a) Imaginary part: damped frequency

(b) Real part: effective damping

Figure 2.12: Variation of the modal parameters of the pitch and flap DOFs with the airspeed before flutter. The legend applies to all 2 subplots.

2.5 Post-critical aeroelastic investigation

2.5.1 Bifurcation diagrams

Once the flutter speed is reached, the total damping in the system drops to zero and LCOs are observed. Figure 2.13 displays pitch and flap responses measured at airspeeds of 11.6 m/s and 14.8 m/s. The pitch response is symmetric, smooth and dominated by the fundamental harmonic at both airspeeds. The flap response, on the other hand, is in phase with that of the pitch and quite noisy at low airspeeds because its amplitude is significantly lower than that of the pitch. Furthermore, the flap response is asymmetric, as it is centred around a small negative angle. At higher airspeeds, the flap signal is distorted due to the presence of higher frequency plate - leaf spring modes and the asymmetry is increased.

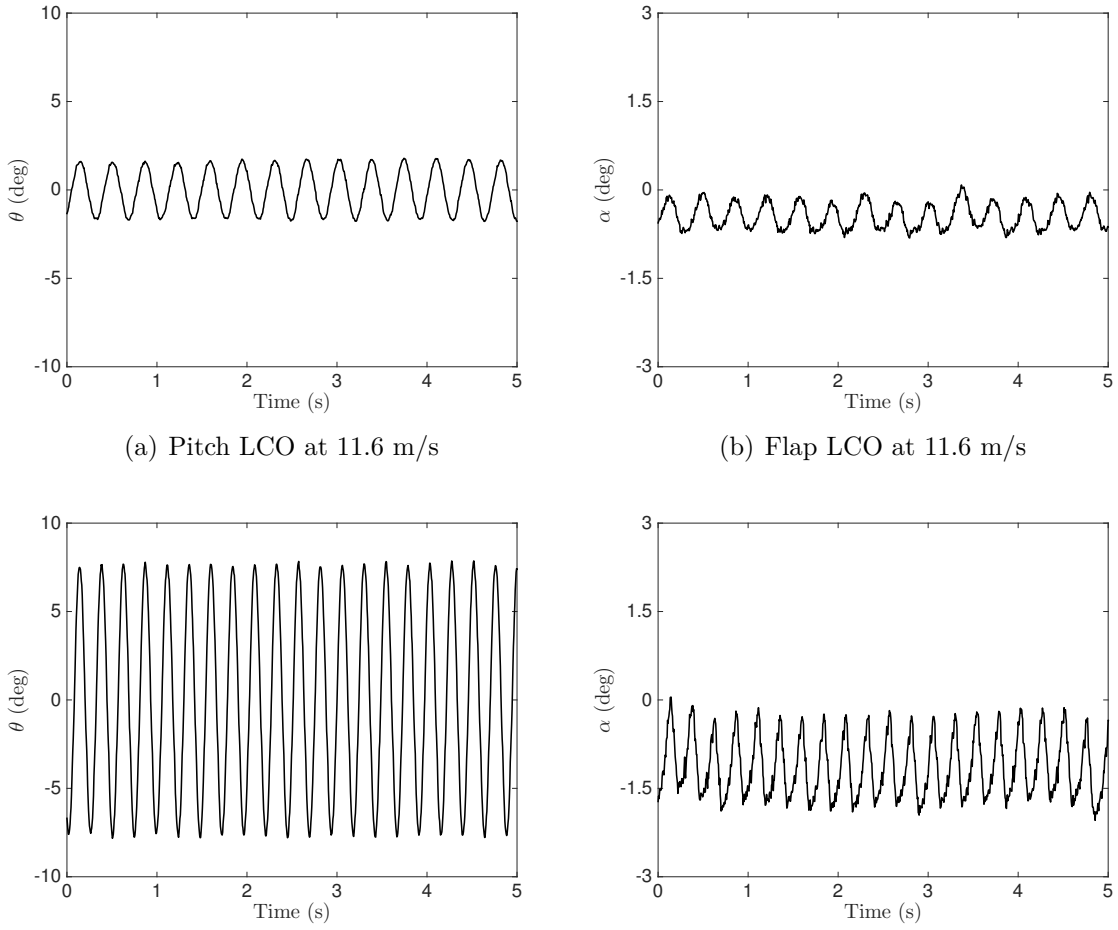

(a) Pitch LCO at 11.6 m/s

(b) Flap LCO at 11.6 m/s

(c) Pitch LCO at 14.8 m/s

(d) Flap LCO at 14.8 m/s

Figure 2.13: Time series of the pitch and flap LCO responses at airspeeds of 11.6 m/s and 14.8 m/s

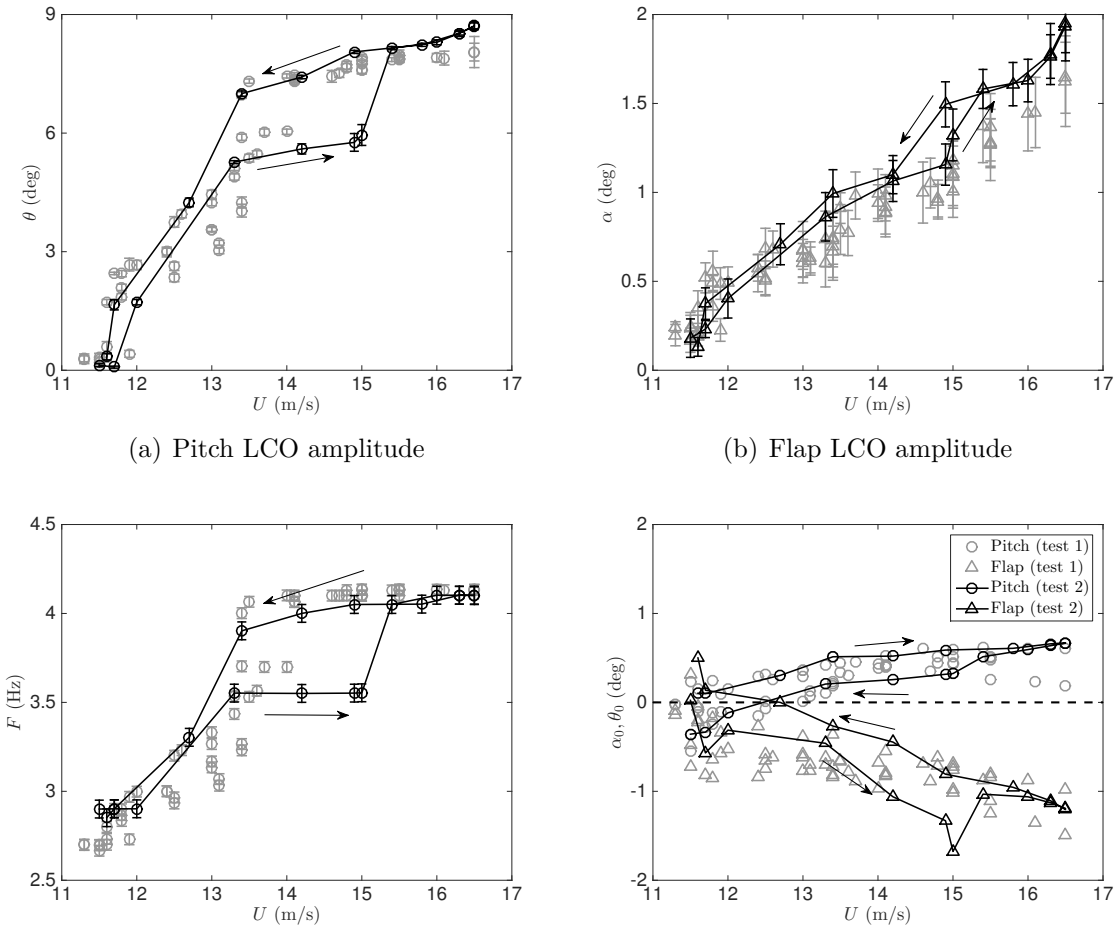

(a) Pitch LCO amplitude

(b) Flap LCO amplitude

(c) LCO frequency

(d) Pitch and Flap average angle

Figure 2.14: Bifurcation diagram of the system. The legend applies to all 4 subplots.

Measuring the frequency, amplitude and mean angles at several stabilised airspeeds yields the system bifurcation diagrams that are depicted in figure 2.14. The grey marks are related to a first test while the black lines corresponds to a second one. In both tests, the airspeed was swept up and down to detect any hysteretic behaviour.

Figure 2.14(a) shows the variation of pitch LCO amplitude (defined as the half of the peak-to-peak amplitude) with airspeed, where the error bars indicate the standard deviation around these averages. The bifurcation at 11.5 m/s is a supercritical Hopf: the LCOs were self-excited, and manual perturbations to the system did not lead to jumps on branches of higher amplitude. The Hopf point coincides with the flutter speed of the underlying linear system, i.e. a linearised version of the nonlinear system around the fixed point [17]. As a consequence, the terms Hopf speed and flutter speed are used inter-

changeably in this work. Further measurements were performed at increasing airspeeds up to a maximum of 16.5 m/s, followed by decreasing airspeed recordings. A hysteresis loop was observed between 13 and 15 m/s, whereby the amplitude jumped upwards for increasing airspeeds and downwards for decreasing airspeeds. The slope of the amplitude airspeed diagram changed because of these jumps.

The flap bifurcation diagram plotted in figure 2.14(b) is different to that of the pitch. The amplitude is low, which explains why the flap error bars look bigger, and increases smoothly with airspeed in both tests. The hysteresis effect is much less visible in this graph. The pitch domination of the motion was expected since the flutter mechanism of figure 2.12 shows that the pitch damping becomes zero at flutter.

The variation of the LCO frequency with airspeed is depicted in figure 2.14(c). The LCO frequency is initially 2.5 Hz and increases steadily up to 3.5 Hz. Then an hysteresis loop occurs and a saturation is observed in the increasing airspeed direction, so that the frequency is stabilised at 4.1 Hz. The loop is bounded by frequency jumps that coincide with those of the pitch amplitude jumps, i.e. between 13 and 15 m/s.

Finally the pitch and flap mean angles, shown in figure 2.14(d), indicate the asymmetry of the LCOs. The pitch mean angle is negligible but that of the flap is not. Consequently, the flap oscillations are highly asymmetrical and the mean flap angle increases steadily with airspeed. This phenomenon is due to the geometrical asymmetry in the system and the position of the pitch axis, which lies behind the aerodynamic centre. A small pitch displacement leads to a large aerodynamic flap moment which in turn causes a flap deflection that increases quadratically with airspeed but has a negligible effect on the LCO amplitude.

2.5.2 Waterfall plots

The waterfall plots of figure 2.15 provide additional insight into the frequency content of the LCOs. This representation of the frequency content, computed using Wavelet transforms, provides a quick and compact overview of the system's behaviour. Figure 2.15(a) plots the frequency content of the pitch accelerations, $\ddot{\theta}$, while figure 2.15(b) displays the frequency content measured from accelerometer A_1, placed at the trailing edge of the plate near the quarter of the span. As a result, accelerometer A_1 is excited by the pitch and flap modes, but also by the higher modes that involve deformation of the plate and the second mode of the leafspring. The following peaks are observed:

- The fundamental frequency, f_0, lies at 2.9 Hz at 11.7 m/s and reaches 4.1 Hz at 15.5 m/s on the A_1 and $\ddot{\theta}$ accelerations, see figure 2.14(c).
- A small second harmonic, $2f_0$, is observed throughout the airspeed range. The magnitude of this harmonic increases after the jump on the response of A_1 but decreases on $\ddot{\theta}$.
- The third harmonic, $3f_0$, is present in both signals and its relative magnitude is not significantly affected by the jump.
- The fourth, fifth and sixth harmonics, $4f_0$, $5f_0$ and $6f_0$, are visible throughout the airspeed range on A_1 only. After the jump, they appear on the pitch accelerations and the magnitude of the $4f_0$ and $6f_0$ peaks increases drastically on A_1.

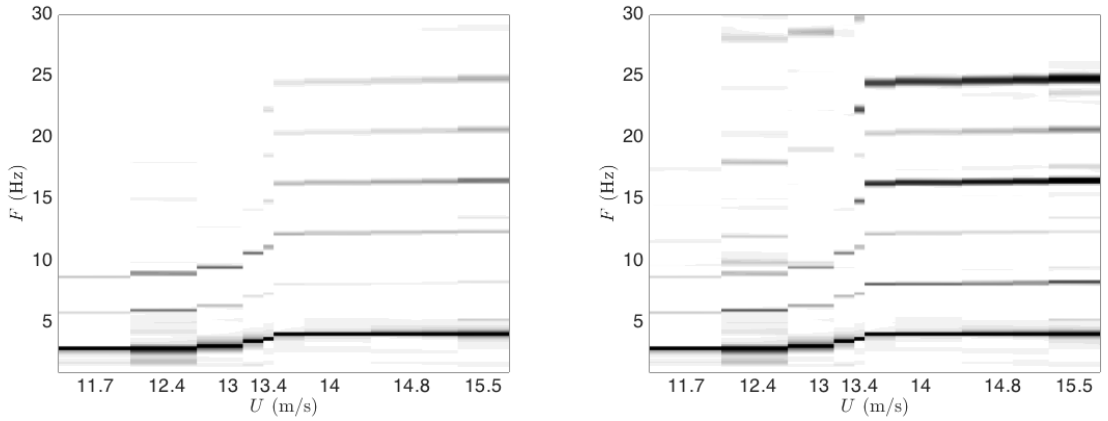

(a) Pitch accelerations (b) Accelerations A_1 (quarter span trailing edge)

Figure 2.15: Waterfall plot of the pitch acceleration $\ddot{\theta}$ (left) and of the accelerations A_1 (right)

Another representation of the waterfall plots is given in figure 2.16. This time, the magnitude and the relative phase of the response of accelerometers A_1, A_2 and A_3 are plotted in the frequency domain. This representation of the frequency content of the response is less compact however spatial information is now available thanks to the phase of the signals (see section 2.3). The goal of this waterfall plot is to look for modal interactions close to the airspeed of the jump in order to understand whether or not they can be the cause of this jump. The following airspeeds are considered:

- 11.7 m/s: the fundamental LCO frequency lies at 2.9 Hz and is dominated by the pitch mode (accelerometers A_2 and A_3 are out of phase and accelerometers A_1 and A_2 are in phase). Mode 3 lies at 9.6 Hz, between harmonics 3 and 4 and therefore does

not interact with the pitch or any of its harmonics. Mode 4 lies at 28.3 Hz between harmonics 9 and 10 and does not seem to interact either. Most of the harmonics of the fundamental LCO frequency feature in-phase accelerometer responses, which suggests that they do not lead to pitching deflections but to deflections similar to the shapes of modes 3, 4 and 6. Conversely, harmonic 3 features in-phase responses of accelerometers A_1 & A_2 and out-of-phase responses of the other combinations which suggests a pitching motion.

- 12.4 m/s: the third harmonic of the pitch is closer to mode 3 and mode 4 does not have any harmonics to interact with. Most of the harmonics still lead to in-phase accelerometer responses, which suggests that the deflections are similar to the shapes of modes 3, 4 and 6.

- 13 m/s: the frequency of harmonic 3 coincides with that of mode 3 and the frequency of harmonic 9 coincides with that of mode 4 however the jump is not observed yet, which means that the jump is not the result of these 3:1 and 9:1 modal interactions between mode 2 and modes 3 and 4.

- 13.3 m/s: the jump has occurred and there is no more frequency matching between mode 3 and harmonic 3 or between harmonic 9 and mode 4, which suggests that the jump is not caused by these modal interactions.

The fact that the jump does not appear when a harmonic of the fundamental LCO frequency is matched to the frequency of mode 3 or 4 suggests that modal interaction is not the origin of the jump observed on the bifurcation diagrams.

At all the airspeeds considered, harmonics 2, 4 and 6 lead to an in-phase response of accelerometers A_1, A_2 and A_3, which suggests that such harmonics induce a motion that is similar to the deflections of modes 3, 4 and 6 rather and a pitching motion, which would lead to a response of accelerometer A_3 out of phase with those of accelerometers A_1 and A_2. This phenomenon is most likely due to asymmetry in the nonlinear clamps. Figure 2.17 is a sketch of the leaf spring - nonlinear clamps assembly with a drawing of a cut in the plane Φ located at a vertical distance y from the roof. If the assembly is perfectly symmetric (figure 2.17(a)), the torsion of the leaf spring leads to a contact of the spring and the two clamps at points A and B for the same pitch angle no matter the position of plane Φ and a pure hardening pitching moment is obtained. On other hand, if a slight asymmetry is present in the system ((figure 2.17(b)), for any given vertical position of the plane Φ, the leaf spring touches the top clamp at point A at first, then the bottom clamp at point B at a higher pitch angle. This leads to a hardening pitch

moment but also to a force that may excite modes 3, 4 and 6 even number of times per pitching period. Note that if the leaf spring and the clamps are flat, this asymmetry leads to asymmetric forces in plunge but to a symmetric pitching moment.

2.5.3 Airflow separation visualisation using wool tufts

A test with wool tufts demonstrated that separation of the airflow occurs after the jump to pitch LCO amplitudes of around 7° while it does not occur before the jump. Figs. 2.18(b) to 2.18(e) show 4 pictures of the wool tufts placed as displayed in figure 2.18(a) at four time instances of the same half limit cycle. The right row of tufts, which corresponds to the black set in figure 2.18(a), lies near the leading edge of the wing while the left row, which corresponds to the grey set, lies near the trailing edge. The following phenomena occur:

- t_1: the pitch angle is small and increasing, the tufts stick to the surface because the airflow is attached.
- t_2: the pitch angle is large and the front line of tufts (right) is detached from the wing, which indicates separation of the airflow near the leading edge. The second line of tufts is much less affected by separation at this time.
- t_3: the pitch angle is larger than at t_2. The airflow is now separated on both the leading and trailing edges.
- t_4: the pitch angle is small and the airflow is re-attached on the wing.

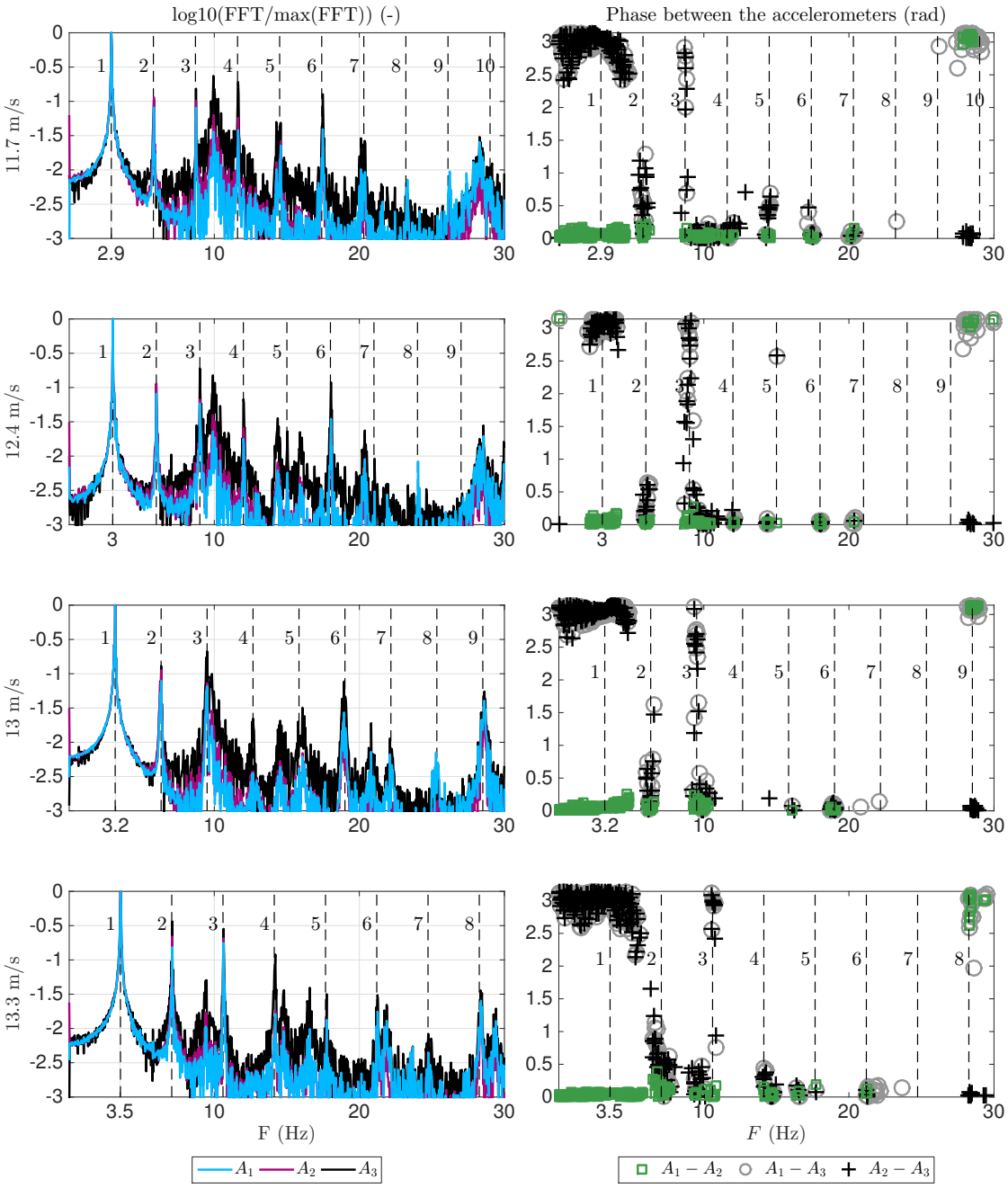

Figure 2.16: Waterfall plot of response of accelerometers A_1, A_2 and A_3 in amplitude (left) and phase (right)

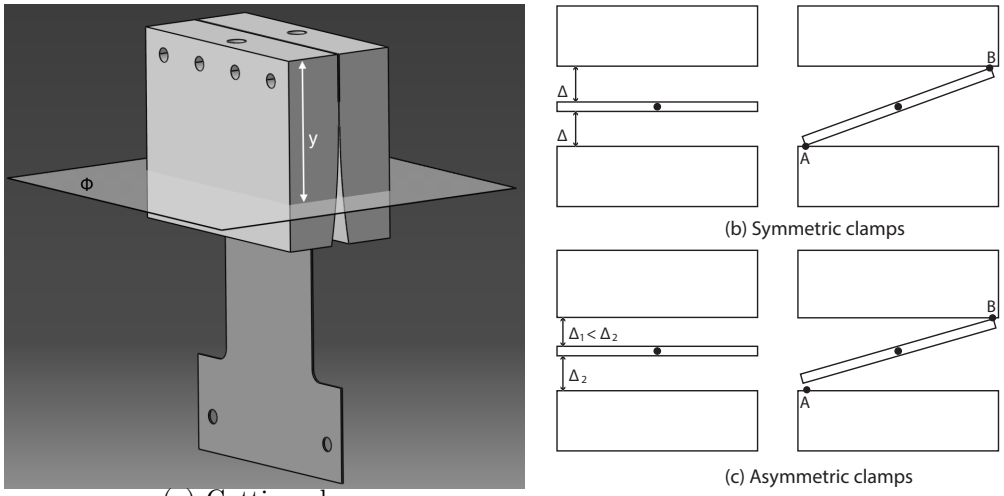

(a) Cutting plane

Figure 2.17: Cut of the nonlinear clamps / leaf spring assembly

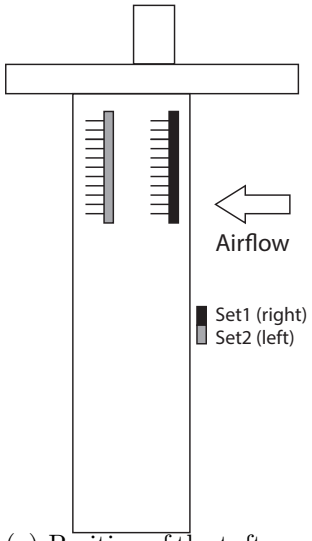

(a) Position of the tufts on the NLPF

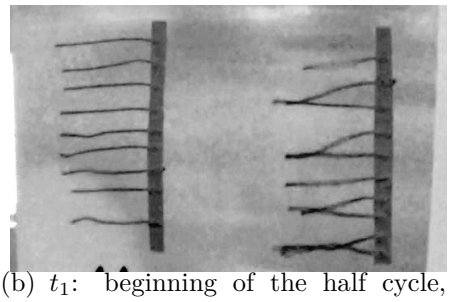

(b) t_1: beginning of the half cycle, small increasing pitch angle and attached flow

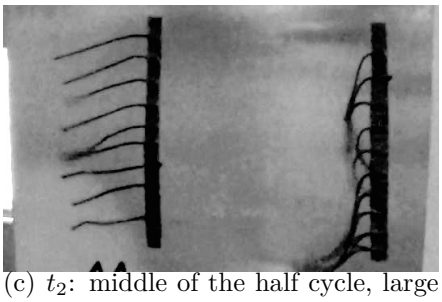

(c) t_2: middle of the half cycle, large pitch angle & separation of the airflow on the leading edge

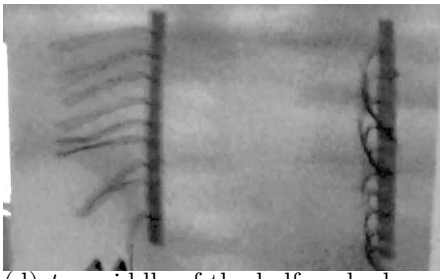

(d) t_3: middle of the half cycle, large pitch angle & separation of the airflow on both the leading and trailing edges

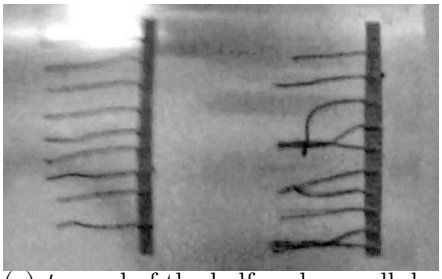

(e) t_4: end of the half cycle, small decreasing pitch angle and attached flow

Figure 2.18: Pictures of wool tufts on the wing during a cycle of half period of stall flutter at 14.9 m/s. The air flows from the right to the left on pictures (b) to (e).

2.5.4 Experimental results summary

The system undergoes a super-critical Hopf bifurcation at an airspeed of 11.5 m/s because of a flutter interaction between the pitch and the flap modes. After flutter, a smooth amplitude and frequency increase with airspeed is observed until about 14 m/s where an hysteresis loop and a jump phenomenon are observed.

The motion is dominated by the pitch motion no matter the airspeed considered. However, analyses performed with accelerometers highlighted that many harmonics arise at large amplitudes and lead to small amplitude deformations of the flat plate and of the leaf spring. The odd harmonics come from the hardening and aerodynamic nonlinearities which affect the pitch mode. Conversely, the even ones are attributed to asymmetric nonlinearities. Imperfect centring of the wing in the test section in combination with the structural and/or aerodynamic nonlinearities induces an asymmetric loading on the structure. Imperfections in the geometry of the system also lead to asymmetries in the aerodynamic loading. Finally, the most significant source of asymmetry is the nonlinear clamps whose geometries are slightly different. As a result, the leaf spring gets in contact with one clamp before the other, leading to excitations perpendicular to the clamps several times per period, which excites modes similar to the wind off modes 3,4 and 6 several times per period.

Using a leaf spring instead of a more typical configuration with bearings leads to the observation of very small amplitude LCOs close to the flutter speed of the system, which are usually damped by the bearings. Nevertheless, the present design resulted in many even harmonics instead.

The origin of the amplitude jump and hysteresis phenomena is most likely stall flutter. This nonlinear aeroelastic phenomenon is caused by the cyclic separation of the airflow (dynamic stall). A similar phenomenon was observed in [57], where among several stall flutter cases, a gentle amplitude growth followed by a jump and hysteresis was observed.

2.6 Mathematical model

The NLPFW is modelled as a two-DOF system, using a formulation similar to Hancock's and assuming that the flexible modes of the plate do not participate significantly in the observed aeroelastic phenomena. The goal of the model is to predict the low amplitude LCOs, in order to understand the effect of a LTVA on the flutter speed and on the post-critical response of the system.

The equations of motion of the system flying with airspeed U in air of density ρ can be developed using linear unsteady attached flow aerodynamic assumptions; a time-domain model can be written by means of Wagner function analysis [15] and strip theory [16]. The structural displacements are denoted by the vector $\mathbf{y} = [\alpha \quad \theta]$ while the 4 aerodynamic states are denoted by the vector $\mathbf{w} = [w_1 \quad \dots \quad w_4]$. Then the complete state vector of the system is given by $\mathbf{x} = [\dot{\mathbf{y}} \quad \mathbf{y} \quad \mathbf{w}]^T$ and has dimensions 8×1. The state space equations of motion of the system are given by

$$\dot{\mathbf{x}} = \mathbf{Q}_{\mathbf{x}} + \mathbf{q}_\theta k_{nl,3} \theta^3 \tag{2.12}$$

where

$$\begin{aligned} \mathbf{Q} &= \begin{pmatrix} -\mathbf{M}^{-1}(\mathbf{C} + \rho U \mathbf{D}) & -\mathbf{M}^{-1}(\mathbf{E} + \rho U^2 \mathbf{F}) & -\rho U^3 \mathbf{M}^{-1} \mathbf{W} \\ \mathbf{I}_{2\times 2} & \mathbf{0}_{2\times 2} & \mathbf{0}_{2\times 4} \\ \mathbf{0}_{4\times 2} & \mathbf{W}_1 & U\mathbf{W}_2 \end{pmatrix} \\ \mathbf{q}_\theta &= \begin{pmatrix} -\mathbf{M}^{-1} \begin{pmatrix} 0 \\ 1 \\ 0 \end{pmatrix} \\ \mathbf{0}_{5\times 1} \end{pmatrix} \end{aligned} \tag{2.13}$$

Matrix $\mathbf{C}$ is the structural damping matrix, $\rho U \mathbf{D}$ is the aerodynamic damping matrix, $\rho U^2 \mathbf{F}$ is the aerodynamic stiffness matrix, $\mathbf{W}$ is the aerodynamic state matrix, $\mathbf{W}_1$ and $\mathbf{W}_2$ are the aerodynamic state equation matrices, $\mathbf{M} = \mathbf{A} + \rho \mathbf{B}$, $\mathbf{A}$ is the structural mass matrix, $\mathbf{B}$ is the aerodynamic mass matrix and $q_\theta k_{nl,3} \theta^3$ is the nonlinear restoring force in pitch. The notation $\mathbf{I}_{2\times 2}$ denotes a unit matrix of size 2×2. The values of all the matrices are given in Appendix B.

2.7 Mathematical model validation

2.7.1 Wind-off frequency and damping backbones

The wind-off characteristics of the system have been validated by comparing the numerical damping and frequency backbones to those measured experimentally (see section 2.3.2). Figure 2.19(a) plots the experimental frequency backbone of the system compared to the frequency backbone of the model obtained by applying the same procedure on time series computed using the Runge Kutta 45 algorithm. Both the pitch (crosses) and the flap (circles) numerical backbones agree very well with the numerical ones.

Figure 2.19(b) depicts the experimental damping backbone of the system compared to the damping backbone of the model obtained again by applying the same identification procedure on simulated time series. The pitch numerical backbone (crosses) agrees very well with the experimental one. On the other hand, the flap damping is well estimated for angles between 2° and 3° then underestimated because the model uses linear damping. Nevertheless, as shown in section 2.5.1, the largest flap amplitude encountered in LCOs was around 3°, where the model accurately predicts the damping.

2.7.2 Pre-critical response

The variation of the system's effective damping and frequency with airspeed obtained from the experiments and from the linear aerodynamic model is plotted in figure 2.20. The frequency is predicted well for both modes (figure 2.20(a)) but the damping (figure 2.20(b)) is over-estimated by the model; it is about twice as high as the measured damping for both the pitch and the flap modes The methods used to compute the damping from the experimental results are subject to four problems that introduce uncertainties in the damping estimate. Firstly, since there is a coupling between the pitch and the flap, the signal used to compute the flap damping does not decay to zero because it is excited by the pitch, which is lightly damped. Secondly, the setup is subject to wind tunnel turbulence which means that its response never really decays to zero. Thirdly, the flap mode is so highly damped that it undergoes only two or three cycles of oscillation before it decays. Fourthly, in order to measure several oscillation cycles, the initial angle from which the setup was released was higher than the stall angle, so that the linear aerodynamic model is too simple. Nevertheless, the model predicts the damping trend reasonably well as the qualitative behaviour of the experimental and mathematical damping curves is similar and the flutter airspeed and frequency are identified with sufficient accuracy.

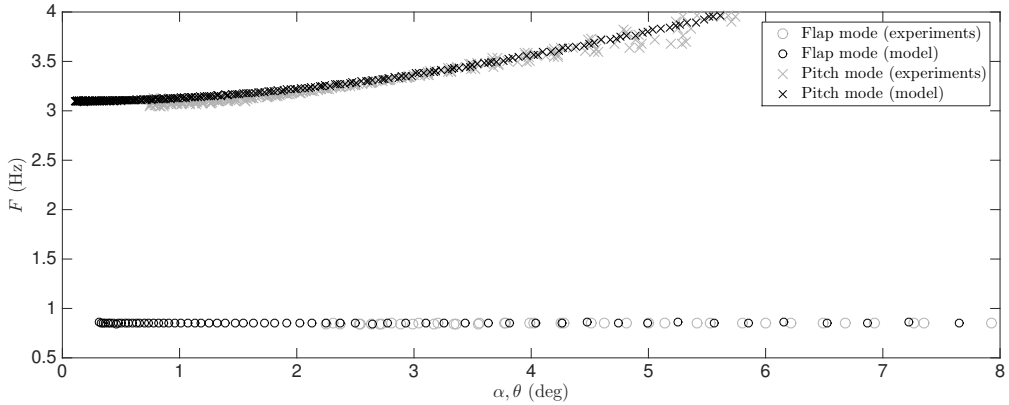

(a) Frequency backbone

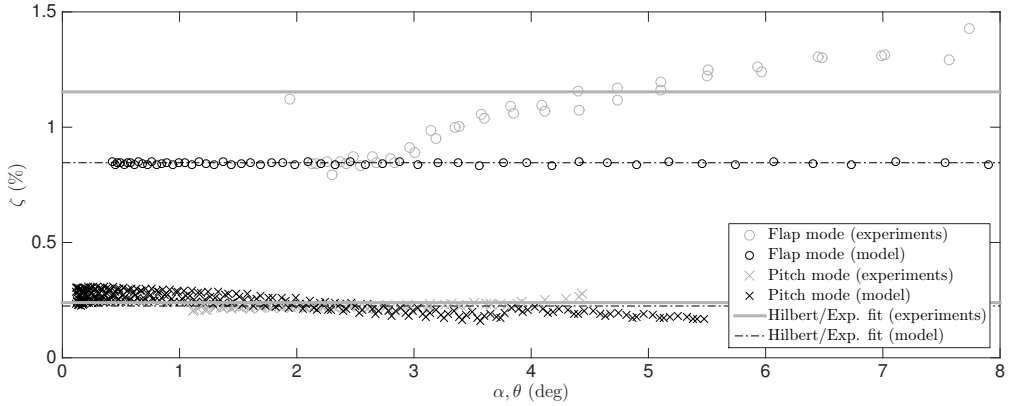

(b) Damping backbone

Figure 2.19: Numerical and experimental frequency and damping backbones of the NLPFW

2.7.3 Post-critical response

Figure 2.21 plots the pitch and flap modelled responses, obtained by numerically solving equation 2.13 using the Runge Kutta 45 algorithm, compared to the measurements at airspeeds of 11.8 m/s and 13.4 m/s. At low speed, both pitch and flap predictions are fairly accurate but a slight frequency difference is observed. At high speed the pitch responses still match, but the flap amplitude seems to be overestimated and the asymmetry is slightly different. Considering how scattered the experimental results are, this prediction is considered satisfactory.

Figure 2.22 compares the bifurcation diagrams measured in the wind tunnel to those obtained by performing numerical continuation [26] on the equations of motion. The pitch response (figure 2.22(a)) is correctly predicted for airspeeds between 11.5 and 13.5 m/s,

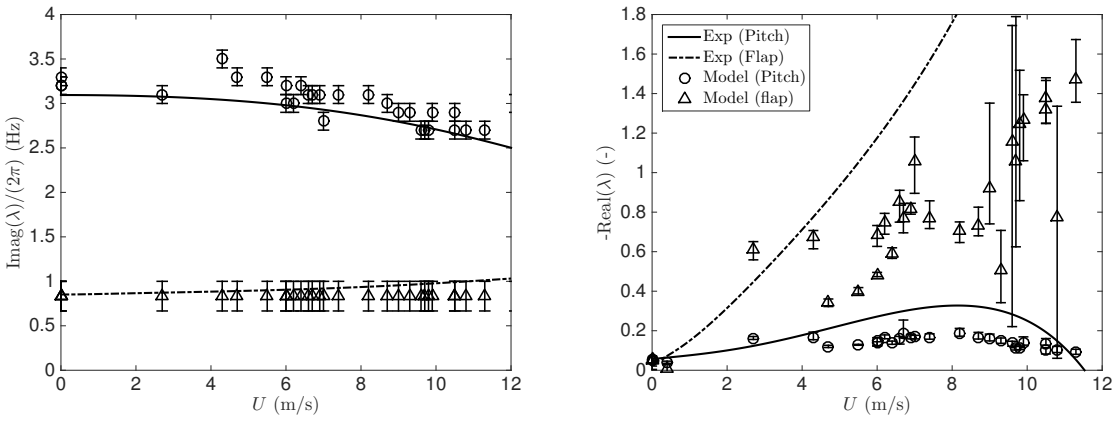

(a) Imaginary part: damped frequency

(b) Real part: effective damping

Figure 2.20: Comparison of the experimental and numerical frequency and damping variation with airspeed of the system

then the model fails to reproduce the jump because it does not take stall and higher mode effects into account. The flap response (figure 2.22(b)) on the other hand is slightly over-estimated by the model. The LCO frequency (figure 2.22(c)) predicted by the model is slightly smaller than the real one (≈ 0.3 Hz), however the model successfully predicts the variation of the frequency until the jump, then it fails again. Finally, the pitch and flap mean angles are accurately represented by setting an alignment error of $\theta_0 = 0.3°$ in pitch in the model. This pitch offset is added into equation 2.12 as

$$\dot{\mathbf{x}} = \mathbf{Q}_\mathbf{x} + \mathbf{q}_\theta k_{nl,3}(\theta - \theta_0)^3 \tag{2.14}$$

This offset has a significant effect on the flap mean amplitude but does not affect the LCO frequency and amplitude. It has therefore been neglected in all the LCO computations and in the LTVA design procedure.

In summary, the model successfully predicts the low amplitude pitch LCO response, slightly overestimates that of the flap and underestimates the LCO frequency. Nevertheless, it is considered accurate enough to attempt to predict the effect of a LTVA to mitigate these LCOs and derive tuning rules.

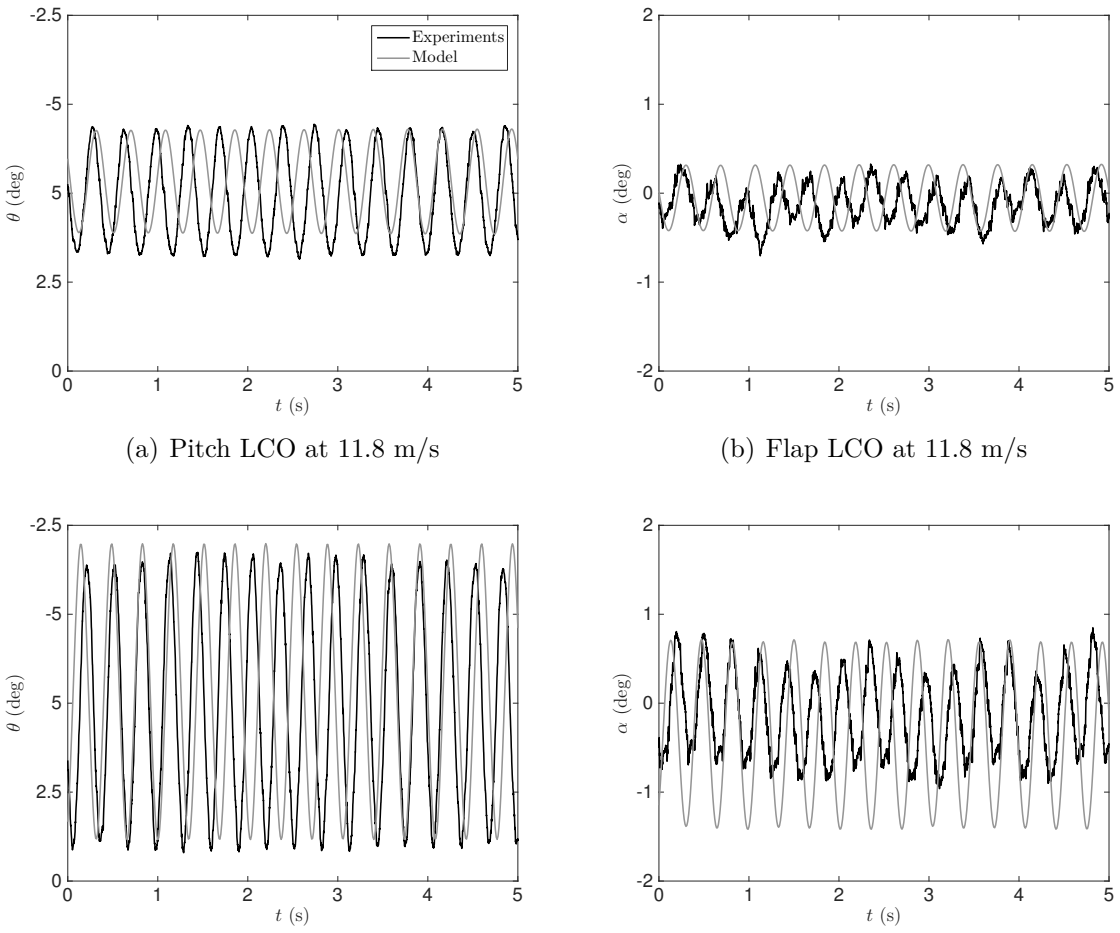

(a) Pitch LCO at 11.8 m/s

(b) Flap LCO at 11.8 m/s

(c) Pitch LCO at 13.4 m/s

(d) Flap LCO at 13.4 m/s

Figure 2.21: Comparison of the experimental and numerical LCO responses of the system at airspeeds of 11.8 m/s and 13.4 m/s. The legend applies to all 4 subplots.

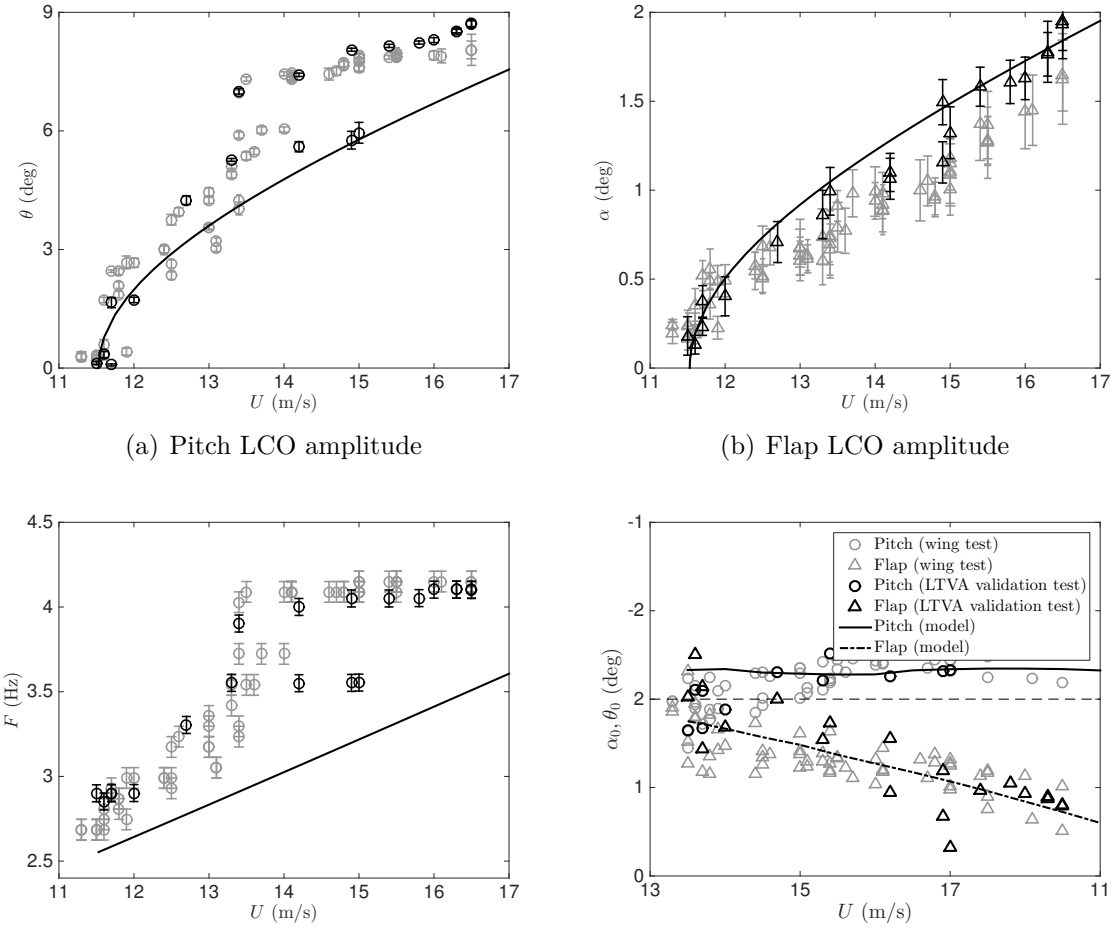

(a) Pitch LCO amplitude

(b) Flap LCO amplitude

(c) LCO frequency

(d) Pitch and Flap mean angle

Figure 2.22: Comparison of the experimental and numerical bifurcation diagrams of the system

2.8 Chapter summary

In this chapter a novel aeroelastic system called the Nonlinear Pitch and Flap Wing is presented. This system is easy to build and does not use any bearings, which allows the system to undergo very small amplitude LCOs close to the flutter speed. The supercriticality of the bifurcation makes the LCO onset speed (smallest speed where LCOs can be observed) independent of the initial conditions induced by the wind tunnel user which leads to a more accurate prediction of the flutter speed of the system. Flutter occurs at an airspeed of 11.5 m/s, then the amplitude increases smoothly until 13.5 m/s where a jump and an hysteresis loop are observed. The jump phenomenon is most likely the result of airflow separation and stall flutter.

A simple model with pitch and flap DOFs and aerodynamics derived from strip theory and Wagner's theory is proposed. Even though the model neglects the contribution of all the higher structural modes, it provides accurate predictions of the flutter speed of the system and of the pitch LCO amplitude for airspeeds between 11.5 m/s and 13.5 m/s then fails because the nonlinear aerodynamic phenomena that lead to the jump phenomenon are not modelled and because the higher frequency modes of the system are not included in the structural model. The LCO frequency is estimated with an accuracy of 0.3 Hz before the jump and the flap LCO amplitude is slightly overestimated, possibly because of the participation of the higher modes in the measured flap motion.

Chapter 3

Flutter and LCO suppression on a pitch and flap wing

3.1 Introduction

The goal of this third chapter is to use the numerical model and the experimental apparatus studied in chapter 2 in order to study and demonstrate the beneficial effect of linear and nonlinear tuned vibration absorbers on the NLPFW.

First, the mathematical model is used to understand the effect of the linear absorber on the system and to optimise its parameters to achieve the best possible increase in flutter speed for arbitrarily chosen absorber mass and position. Karpel [102] already demonstrated that a substantial increase in flutter speed can be achieved but did not study the effects of the absorber tuning and position. In the present work, the effect of the absorber's position, mass and length are thoroughly investigated.

Then, a cubic nonlinear restoring force is added to the LTVA, making it a NLTVA. The goal is to counter the effect of the detuning of the linear absorber induced by the cubic nonlinearity present in the model of the primary system, thus improving the performance. Malher et al. [109] and Habib et al. [108] demonstrated that such nonlinear absorbers can transform a sub-critical bifurcation into super-critical in a similar aeroelastic system, yet they did not investigate the presence of isolated solution branches.

Finally, the performance of the linear absorbers is demonstrated in the wind tunnel. Nonlinear absorbers could unfortunately not be tested for practical reasons.

3.2 Mathematical model

The primary system with a (N)LTVA attached is sketched in figure 3.1. The absorber consists of a mass m_{ltva} at the end of a rod of length r_a that is able to rotate in the plane ϕ around the LTVA axis, which is parallel to the pitch axis, at a distance r_θ. The rotation angle of the absorber is measured by the DOF ξ. The whole assembly is at a distance r_α from the flap axis. Finally, a rotational spring and dashpot of stiffness k_a and damping coefficient c_a, respectively, provide restoring and dissipative forces to the absorber. A nonlinear restoring force F_{nl}, added in parallel to the absorber's linear stiffness is also considered later in the study.

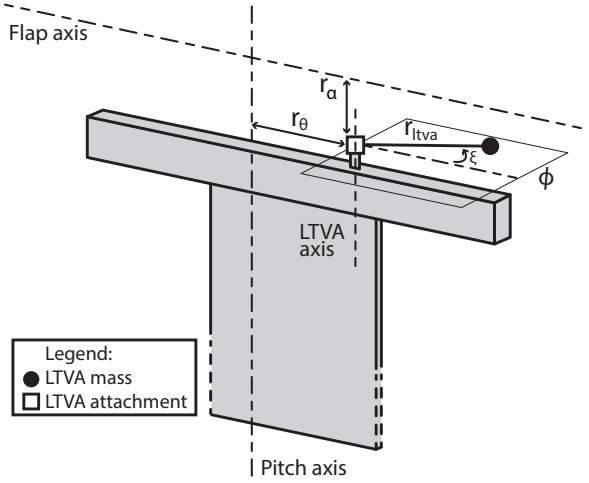

Figure 3.1: Drawing of the system with a LTVA attached

Assuming the absorber is isolated from the airflow, the equations of motion of the system flying with airspeed U in air of density ρ are very similar to equation 2.13. The structural displacements are denoted by the vector $\mathbf{y} = [\alpha \quad \theta \quad \xi]$ while the 4 aerodynamic states are denoted by the vector $\mathbf{w} = [w_1 \quad \dots \quad w_4]$. Then the complete state vector of the system is given by $\mathbf{x} = [\dot{\mathbf{y}} \quad \mathbf{y} \quad \mathbf{w}]^T$ and has dimensions 10×1. The state space equations of motion of the system are given by

$$\dot{\mathbf{x}} = \mathbf{Q}_\mathbf{x} + \mathbf{q}_\theta k_{nl,3}\theta^3 + \mathbf{q}_\xi F_{nl}(\xi) \tag{3.1}$$

where

$$\begin{aligned}
\mathbf{Q} &= \begin{pmatrix} -\mathbf{M}^{-1}\left(\mathbf{C}+\mathbf{C}_{ltva}+\rho U\mathbf{D}\right) & -\mathbf{M}^{-1}\left(\mathbf{E}+\mathbf{E}_{ltva}+\rho U^2\mathbf{F}\right) & -\rho U^3\mathbf{M}^{-1}\mathbf{W} \\ \mathbf{I}_{3\times 3} & \mathbf{0}_{3\times 3} & \mathbf{0}_{3\times 4} \\ \mathbf{0}_{4\times 3} & \mathbf{W}_1 & U\mathbf{W}_2 \end{pmatrix} \\
\mathbf{q}_\theta &= \begin{pmatrix} -\mathbf{M}^{-1}\begin{pmatrix} 0 \\ 1 \\ 0 \end{pmatrix} \\ \mathbf{0}_{7\times 1} \end{pmatrix} \qquad (3.2) \\
\mathbf{q}_\xi &= \begin{pmatrix} -\mathbf{M}^{-1}\begin{pmatrix} 0 \\ 0 \\ 1 \end{pmatrix} \\ \mathbf{0}_{7\times 1} \end{pmatrix} \\
\mathbf{M} &= \mathbf{A}+\mathbf{A}_{ltva}+\rho\mathbf{B} \qquad (3.3)
\end{aligned}$$

Matrices $\mathbf{A}$, $\mathbf{A}_{ltva}$ and $\mathbf{B}$ are respectively the structural, absorber and aerodynamic mass matrices, $\mathbf{C}$, $\mathbf{C}_{ltva}$ and $\rho U\mathbf{D}$ are respectively the structural, absorber and aerodynamic damping matrices, $\mathbf{E}$, $\mathbf{E}_{ltva}$ and $\rho U^2\mathbf{F}$ are respectively the structural, absorber and aerodynamic stiffness matrices. $\mathbf{W}$ is the aerodynamic state matrix, $\mathbf{W}_1$ and $\mathbf{W}_2$ are the aerodynamic state equation matrices, $q_\theta k_{nl,3}\theta^3$ is the nonlinear restoring force in pitch and $q_\xi F_{nl}$ is the absorber nonlinear restoring force. The notation $\mathbf{I}_{3\times 3}$ denotes a unit matrix of size 3×3. The values of all the matrices are given in Appendix C.

The equations of motion feature six linear parameters and one nonlinear parameter that can be used to optimise the absorber. Firstly, the mass m_a, the length r_a and the position of the absorber r_θ and r_α are design constraints in practice. A non-dimensional mass $\overline{m}_a$ obtained by dividing m_a by 2.740 kg, the total mass of the wing, is also used as an indication of the relative increase in the full system mass due to the absorber. Then, the linear absorber's natural frequency f_{ltva} given by

$$f_{ltva} = \frac{1}{2\pi}\sqrt{\frac{k_a}{I_a}} = \frac{1}{2\pi}\sqrt{\frac{k_a}{m_a r_a^2}}$$

and the absorber modal damping, ζ_{ltva} which is written as

$$\zeta_{ltva} = c_a/(2\sqrt{k_a I_a})$$

are used rather than the stiffness and damping coefficients and can be tuned to optimise the absorber for any combination of the six linear design parameters. Finally, the nonlinear force F_{nl} can be added to improve the post-critical performance of the system.

3.3 Linear absorber optimisation

3.3.1 Effect of the absorber frequency and damping

The first case considered is $m_a = 64$ g, $r_\theta = 0.125$ m, $r_\alpha = 0.05$ m and $r_a = 0.1$ m. The goal of this first study is to understand how to tune the frequency and damping of a given absorber in order to optimise the linear flutter speed of the coupled system. This position and mass ratio correspond to those that are studied in the wind tunnel in Section 3.5.3.

Figure 3.2 depicts the flutter speed of the system with an absorber attached, for absorbers with damping ratios between 2.5% and 30% and frequencies between 0.5 and 4.5 Hz. The optimal LTVA features a frequency of 1.89 Hz and a modal damping of 14.5%. It increases the flutter speed to 15.63 m/s (an increase of approximately 36%). The system appears to be very sensitive to the LTVA frequency: a detuning of the absorber of just -0.09 Hz or $+0.11$ Hz leads to a flutter speed of only 14.2 m/s. The sensitivity in damping is much smaller as an absorber detuned in damping by $+12\%$ or -5% achieves a performance similar to those of an absorber detuned in frequency. In the following studies three LTVAs are considered in detail:

- The optimal LTVA provides the best flutter speed. It is tuned at $f_{ltva} = 1.89$ Hz and $\zeta_{ltva} = 14.5\%$. It is indicated by the white square in figure 3.2.
- The super-optimal LTVA is detuned by $+0.11$ Hz and therefore tuned at $f_{ltva} = 2$ Hz and $\zeta_{ltva} = 14.5\%$. It corresponds to the white cross in figure 3.2.
- The sub-optimal LTVA is detuned by -0.09 Hz and tuned at $f_{ltva} = 1.8$ Hz and $\zeta_{ltva} = 14.5\%$. It corresponds to the white triangle in figure 3.2.

Finally, it is interesting to notice that at low damping and high frequency, the LTVA can have a detrimental effect on the system. In this case, the addition of the absorber decreases the frequency of the pitch mode without adding significant damping to the system, causing the two natural frequencies to approach each other and reducing the flutter speed.

The explanation of the optimality of an absorber can be obtained by looking at the variation of the natural frequency and damping ratios of the modes of the system with

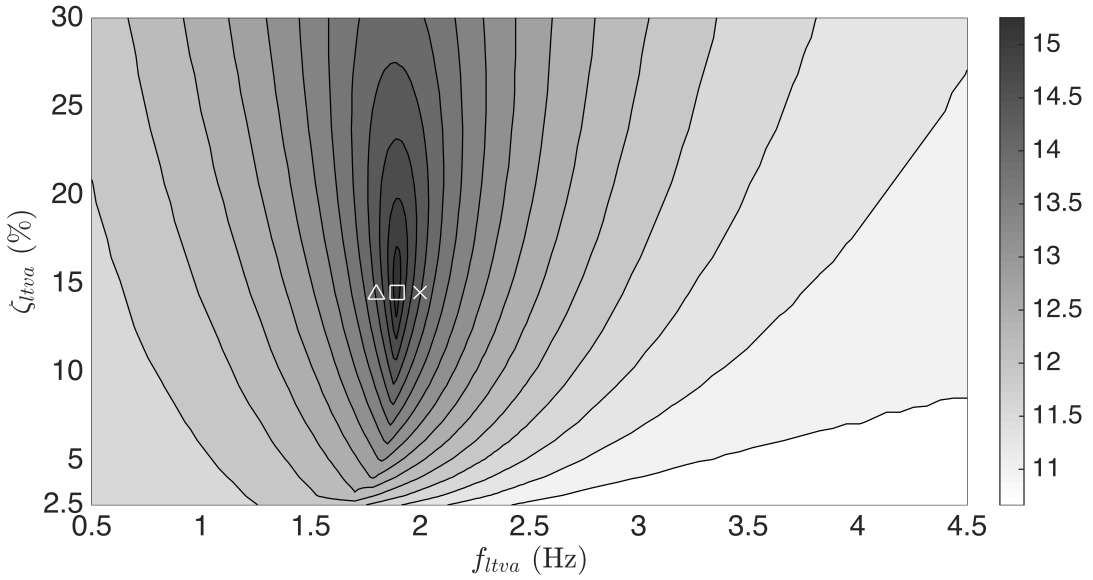

Figure 3.2: Flutter speed of the system with a LTVA of mass 64 grams as a function of the LTVA modal damping and frequency.

Absorber	U_{flut} [m/s]	F_{flut} [Hz]	Flutter mechanism
No absorber	11.5	2.55	Flap + Pitch
sub-Optimal	14.38	2.32	Flap + Out-of-phase Pitch-LTVA
super-Optimal	14.37	1.92	Flap + In-phase Pitch-LTVA
Optimal	15.63	2.01	Flap + In/Out-of-phase Pitch-LTVA

Table 3.1: Flutter characteristics of the system with a LTVA

airspeed. Figure 3.3 plots the system's modal parameters variation with airspeed without absorber and with the sub-Optimal, Optimal and the super-Optimal absorbers. Table 3.1 summarises the flutter frequency and mechanism of the 4 systems.

Figures 3.3(a) and 3.3(b) respectively display the variation of the modal frequencies and damping ratios of the primary system alone (grey) compared to those of the system with a sub-optimal absorber (black). At wind-off, the addition of the LTVA does not have much effect on the flap mode but splits the pitch mode into two pitch-LTVA modes. The first of these two modes (squares) involves an out-of-phase motion of the pitch DOF and of the absorber and is similar to the pitch mode of the primary system alone in terms of frequency but with a higher damping ratio. On the other hand, the second pitch-LTVA mode (triangles) features an in-phase motion of the wing and of the absorber, a very high damping and a frequency that lies between the frequencies of the pitch and flap modes of the primary system. The flap mode of the coupled system (circles) is practically unaf-

fected. The addition of the 1.8 Hz absorber slightly increases the frequency and damping of the initial pitch mode (squares), which delays flutter. On the damping curve, we can indeed see that it is still the same mode that flutters, only at a higher airspeed. On the flap mode, it is nearly impossible to distinguish the effect of the absorber as both the frequency and damping curves lie on top of each other. The flutter frequency, which is equal to the frequency of the mode whose damping reaches 0, is equal to 2.32 Hz while that of the primary system was 2.55 Hz.

Figures 3.3(c) and 3.3(d) respectively plot the same quantities for an optimal absorber. In this case, the in-phase and out-of-phase modes are identical at flutter and it is no longer possible to distinguish which mode flutters. A tiny increase in absorber frequency will result in an in-phase flutter mechanism while a tiny decrease will result in an out-of-phase flutter.

Figures 3.3(e) and 3.3(f) finally correspond to the super-optimal LTVA. In this configuration, it is not the out-of-phase pitch-LTVA mode that flutters but the in-phase one. As a result, the flutter frequency is only 1.92 Hz. Comparing these three absorbers clearly explains the origin of the optimal tuning: reducing the absorber frequency reduces the flutter speed of the out-of-phase pitch-LTVA mode while increasing it reduces the flutter speed of the in-phase pitch-LTVA mode so the optimal is reached when the two modes flutter simultaneously. Right after the flutter point, the damping of the in-phase mode becomes negative while that of the out-of-phase mode rapidly increases with airspeed. Finally, the negligible effect of the absorber on the flap mode is due to the fact that the former lies close to the flap axis, while the flap inertia is much higher than the pitch inertia.

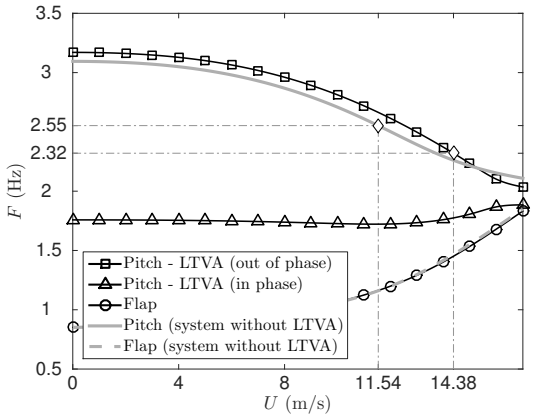

(a) $f_{ltva} = 1.8$ Hz and $\zeta_{ltva} = 14.5\%$

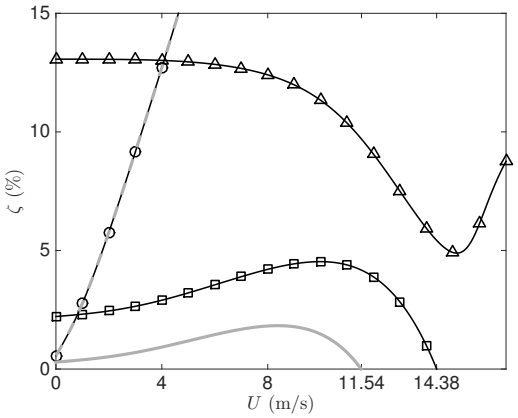

(b) $f_{ltva} = 1.8$ Hz and $\zeta_{ltva} = 14.5\%$

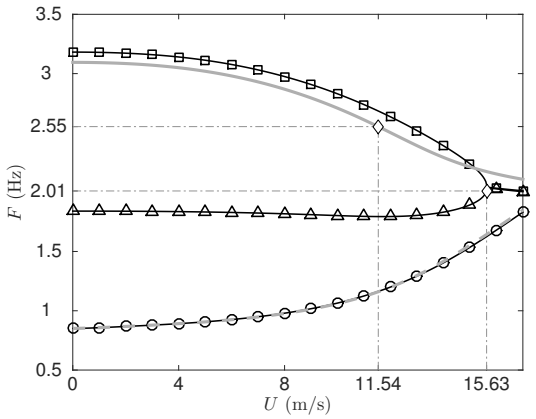

(c) $f_{ltva} = 1.89$ Hz and $\zeta_{ltva} = 14.5\%$

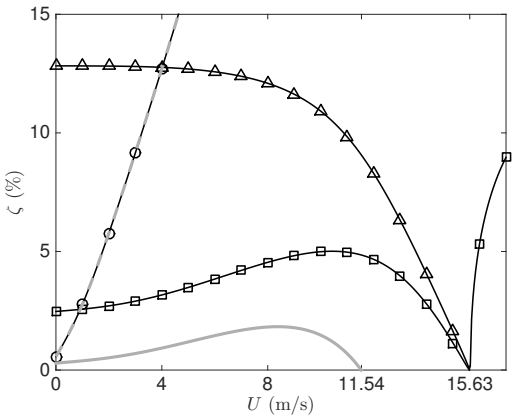

(d) $f_{ltva} = 1.89$ Hz and $\zeta_{ltva} = 14.5\%$

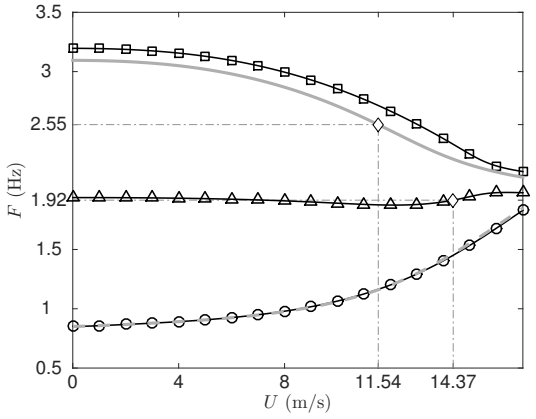

(e) $f_{ltva} = 2.0$ Hz and $\zeta_{ltva} = 14.5\%$

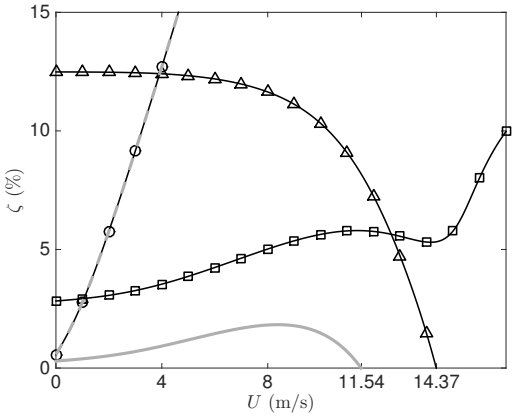

(f) $f_{ltva} = 2.0$ Hz and $\zeta_{ltva} = 14.5\%$

Figure 3.3: Variation of the modal parameters with airspeed of the system with absorbers tuned at $\zeta_{ltva} = 14.5\%$ and $f_{ltva} = 1.8$ Hz, 1.89 Hz and 2.0 Hz.

3.3.2 Effect of the absorber mass and length

The second case considered is still $r_\theta = 0.125$ m, $r_\alpha = 0.05$ m. This time, the mass is varied from 4 grams (0.14% mass ratio) to 160 grams (5.8% mass ratio), the length is varied form 0.05 m to 0.15 m and the frequency and damping are optimised for each configuration.

Figure 3.4 plots the optimal flutter speed, LTVA frequency and LTVA damping as functions of the absorber's mass ratio. The performance increases rapidly for small mass ratios then the growth becomes slower. Similar observations are made for the optimal LTVA frequency and damping, which respectively rapidly decrease and increase then vary at a slower rate as the mass ratio is increased. Increasing the absorber's length increases its inertia therefore increases the performance as well. As a result, the absorber mass and length should be made as large as possible. Nevertheless, design constraints such as space, mass requirements, frequency and damping may limit the performance.

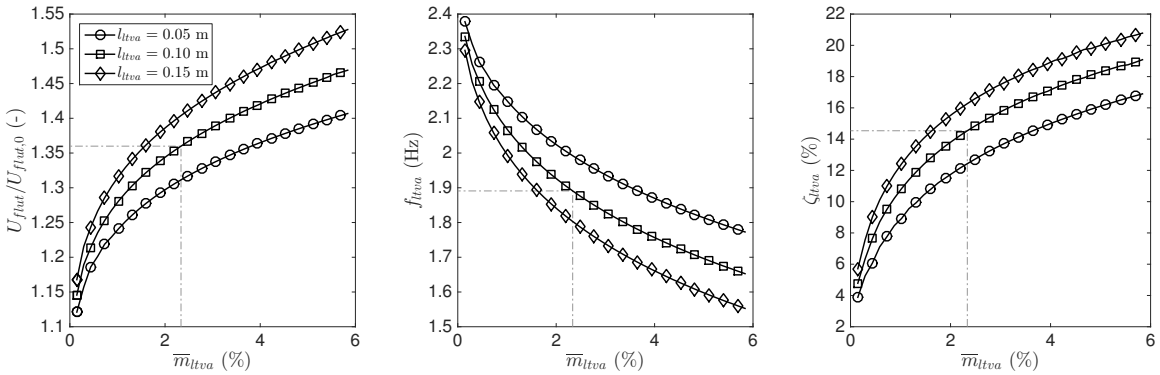

(a) Flutter speed (b) LTVA frequency (c) LTVA damping

Figure 3.4: Optimal flutter speed, LTVA frequency and damping ratio as a function of the absorber's mass ratio and length

Figure 3.5 depicts the optimal flutter speed, LTVA frequency and LTVA damping this time as a function of a combined pitch-LTVA inertia which is written as $m_a(r_\theta + r_a)^2$. The three curves almost lie on top of each other which, suggests that increasing the mass or the length of the absorber has a similar effect. The small difference in the curves is probably due to the effect of the absorber on the flap mode which, is not taken into account in the combined pitch-LTVA inertia.

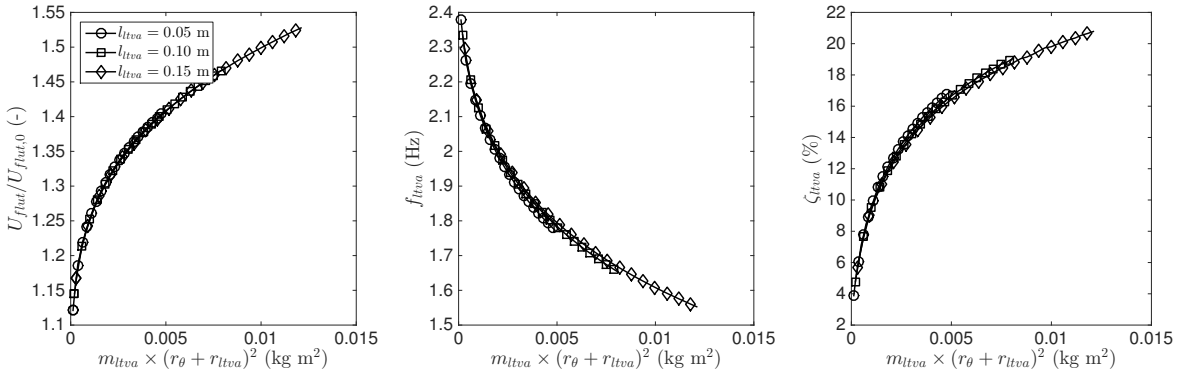

(a) Flutter speed (b) LTVA frequency (c) LTVA damping

Figure 3.5: Optimal flutter speed, LTVA frequency and damping ratio as a function of the absorber's inertia in pitch

3.3.3 Effect of the absorber position

The last parameter considered is the absorber's position. The LTVA's mass and length are respectively set to $m_a = 64$ g and $r_a = 0.1$ m. The chordwise LTVA attachment point, r_θ, is varied from the pitch flexural axis to the trailing edge of the wing while the spanwise attachment point is varied from the flap flexural axis to the wing tip. These positions were chosen because they would be the most convenient positions to attach an absorber in a real-life application.

Figure 3.6 depicts the flutter speed of the coupled system and the optimal LTVA frequency and damping as a function of the LTVA position. Each point of the colormap indicates the performance of the system with the LTVA defined above attached to this point. As expected, the further the absorber lies from the pitch and flap axis, the better the performance because it leads to a stronger coupling between the LTVA and the pitch and flap modes. Moving the absorber downstream improves the flutter speed more than moving it outboard because the pitch mode flutters and because the pitch inertia is lower than the flap inertia. Again, better performance requires lower frequency and higher damping which can lead to some limitations for practical implementations.

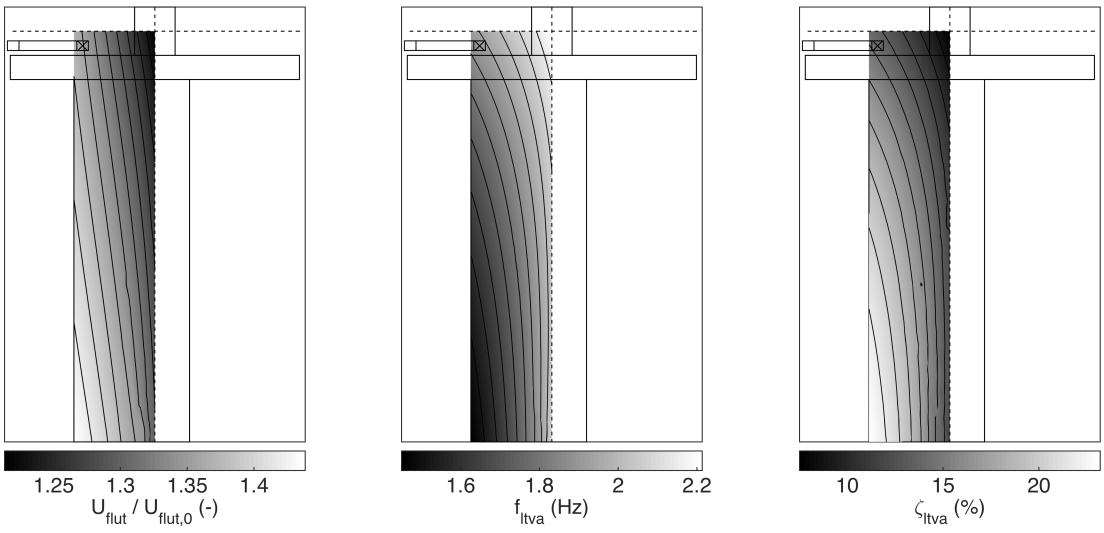

(a) Flutter speed (b) LTVA frequency (c) LTVA damping

Figure 3.6: Optimal flutter speed, LTVA frequency and damping ratio as a function of the absorber's position on the wing

3.4 Bifurcation analysis

The system's nonlinear response (i.e. at large amplitude and above the flutter speed) is computed by means of two different numerical continuation codes [26]. In section 3.4.1, the post-critical response of the linear absorbers designed in section 3.3.1 is investigated using a continuation code based on finite differences while in section 3.4.2, the beneficial effect of a nonlinear force added to the optimal LTVA is studied by means of a shooting continuation code.

The linear analyses performed in section 3.3.1 highlighted that the increase in flutter speed due to the attachment of the LTVA on the primary system is very sensitive to the absorber's natural frequency. Is this section, the full nonlinear system is considered, which means that the system's instantaneous response frequencies depend on the airspeed but also on the amplitude in pitch. As a result, the absorber can be effective (tuned) at a given airspeed when the amplitude is low but ineffective when the amplitude is large (detuned) because of the hardening nonlinearity. Throughout this work, the term detuned is used when the natural frequency of the LTVA becomes too small to maximise the energy exchange between the absorber and the primary system because of an increase in airspeed and/or in amplitude.

3.4.1 Post-critical response using linear absorbers

Figure 3.7 compares the post-critical LCO amplitude variation with airspeed of the primary system alone (circles), with the sub-optimal LTVA (dashed-dotted line), the optimal LTVA (dashed line) and the super-optimal LTVA (plain line). In all four cases, the stable solutions are displayed in black while the unstable ones are plotted in grey.

Figure 3.7(a) plots the pitch amplitude of the limit cycle oscillations against airspeed. The sub-optimal LTVA is already detuned when flutter occurs because the absorber's natural frequency is too low. Nevertheless, the LTVA is effective in increasing the Hopf speed (which is coincident with the flutter speed) so that the same LCO amplitudes as those of the primary system are encountered at higher airspeeds. The optimal absorber is only optimal at small pitch amplitudes, i.e. when the effects of the nonlinearity can be neglected. Under these circumstances it increases the flutter speed to 15.6 m/s. However, if the oscillation amplitude is increased, the equivalent linear stiffness in pitch increases because of the hardening nonlinearity and the absorber becomes sub-optimal. In that case, the flutter speed of the equivalent linear system decreases and LCOs can occur at airspeeds below the Hopf condition, which leads to a sub-critical bifurcation. The super-

optimal LTVA becomes optimal when the amplitude and, hence, the equivalent linear pitch stiffness increases. Past a certain amplitude it becomes sub-optimal and limit cycles become possible at lower airspeed, which is what causes the two folds. At this point, increasing the frequency of the absorber would reduce the flutter speed but would also delay the detuning.

Figure 3.7(b) displays the flap response. The bifurcation airspeeds are of course identical to those of figure 3.7(a) but the absorber has a detrimental effect on the flap amplitude. As the LTVA extracts energy from the pitch motion, it transmits a portion of it to the flap motion, so that the latter's amplitude increases faster than in the case without absorber. This is especially true for the super-optimal absorber, which decreases most the pitch amplitude before it is detuned. Once this absorber becomes sub-optimal, the flap amplitude decreases to the levels of the other absorbers.

Figure 3.7(c) finally plots the frequency of the limit cycles. All systems (with and without LTVA) undergo stable limit cycles whose frequencies lie between 2.1 and 3.5 Hz. The only exception is the system with the super-optimal LTVA. At airspeeds before the double fold, the limit cycles of this system are stable and have a lower frequency of about 2 Hz because the flutter mechanism involves the in-phase instead of the out-of-phase pitch-LTVA mode. After the two folds the LTVA becomes sub-optimal and the LCO frequency increases to values close to those of the other absorbers. The optimal LTVA has a flutter frequency of about 2.1 Hz but no stable LCOs occur at this frequency. After the fold the LTVA becomes sub-optimal and the LCO frequency increases to 2.3 Hz. Finally, the sub-optimal absorber features a frequency variation with airspeed similar to that of the primary system as it is already detuned at flutter.

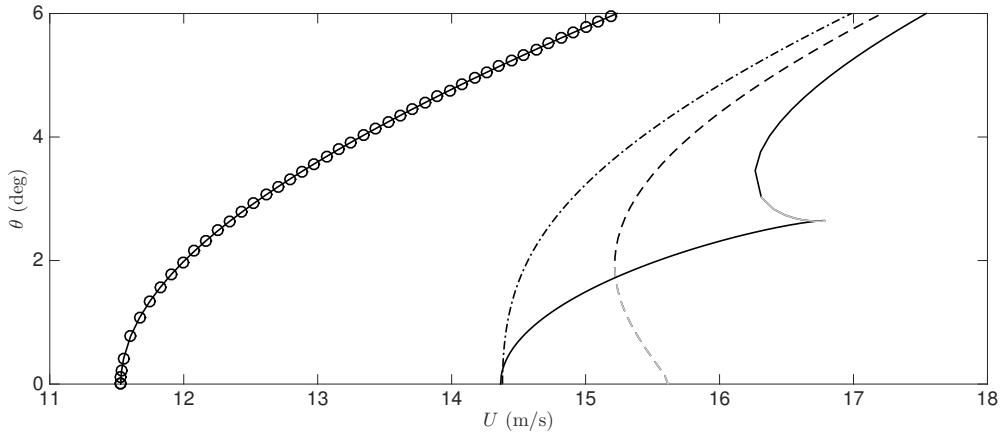

(a) Pitch LCO amplitude

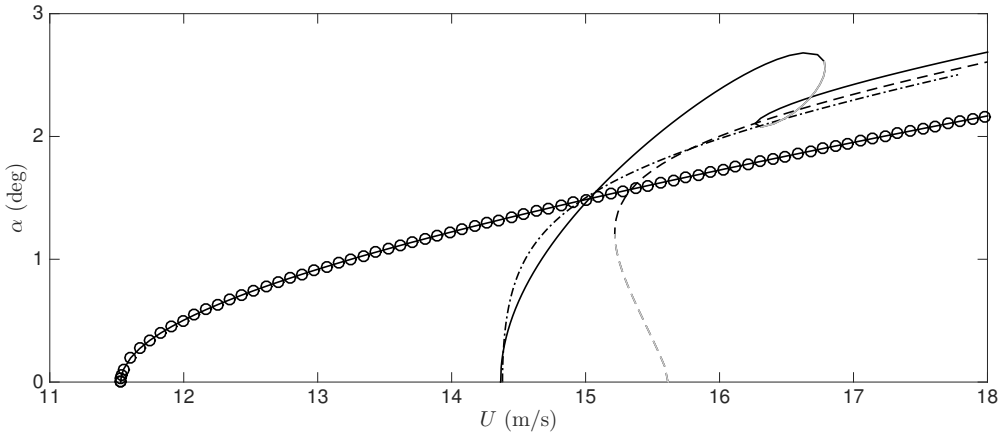

(b) Flap LCO amplitude

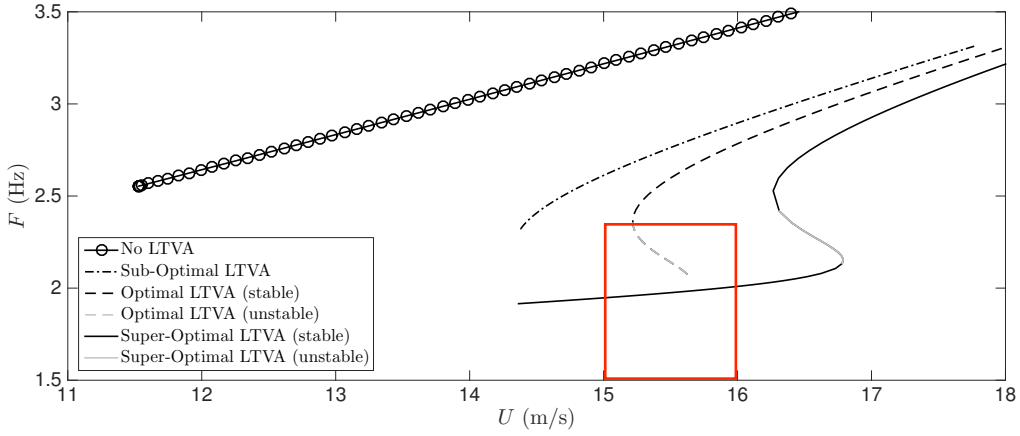

(c) LCO frequency

Figure 3.7: Numerical bifurcation diagrams of the system with different LTVA tunings: the sub-optimal is tuned at $f_{ltva} = 1.8$ Hz, the Optimal one at $f_{ltva} = 1.89$ Hz and the super-Optimal one at $f_{ltva} = 2.0$ Hz, with $\zeta_{ltva} = 14.5\%$ in all three cases.

3.4.2 Post-critical response using nonlinear absorbers

Several authors demonstrated that the addition of a nonlinear force to the absorber, making it a nonlinear tuned vibration absorber, can cancel the detuning effect that occurs at larger pitch amplitude, transforming the sub-critical bifurcation into super-critical [92, 107–109, 113, 114]. In this study, a nonlinear absorber of mass $m_a = 64$ g located in $r_\theta = 0.125$ m and $r_\alpha = 0$ m is considered rather than the absorber located in $r_\alpha = 0.05$ m studied earlier; the goal is to reduce the coupling between the flap mode and the absorber in order to simplify the system. At this location, the optimal LTVA frequency and damping ratios are respectively $f_{ltva} = 1.94$ Hz and $\zeta_{ltva} = 13.5\%$. A cubic nonlinear force written as

$$F_{nl} = c_{nl} \times k_a \times \xi^3$$

is chosen because Habib et al. [114] demonstrated that the nonlinearity in the absorber should mimic that of the primary system for optimal performance. The authors investigated a 1-DOF primary system with cubic, quintic and septic nonlinear restoring forces and combinations of these forces. The paper highlighted that the nonlinear forces included in the NLTVA need to have the same form as those chosen in the primary system in order to achieve equal peaks irrespective of the forcing amplitude, i.e. a cubic and quintic absorber has to be used on a cubic and quintic primary system etc.

Figure 3.8 depicts the bifurcation diagram of the system in pitch and flap for nonlinear coefficients, c_{nl}, ranging from 0 (top) to 1.6 (bottom). The following phenomena are observed:

- $c_{nl} = 0$: the nonlinear force is equal to zero. This bifurcation diagram is almost identical to that in figure 3.7: the absorber increases the linear flutter speed to 15.58 m/s however the bifurcation is sub-critical and LCOs can be observed at airspeeds as low as 15.15 m/s and the LCO onset amplitude is high.

- $c_{nl} = 0.9$: there are now two limit cycle branches, the main branch emanating from the Hopf point and an isolated solution branch. This nonlinear force is not sufficiently strong to turn the sub-critical Hopf bifurcation into super-critical but it reduces the span of the bi-stable region. An isolated solution branch is observed because of the added nonlinearity. It has low pitch amplitude and a high flap amplitude compared to those of the main branch.

- $c_{nl} = 1.1$: the bi-stable region shrinks even more because of the nonlinearity and the isola appears at a lower airspeed. Again this isola has a lower pitch amplitude than that of the main branch a higher flap amplitude.

- $c_{nl} = 1.28$: the nonlinearity has restored the super-criticality of the bifurcation. Surprisingly, the isola of the previous test cases has attached itself to the Hopf point, while the branch that emanated from the Hopf point for $c_{nl} < 1.28$ is now an isola. As a result, the main branch now has lower pitch amplitude and higher flap amplitude than those of the isola.

- $c_{nl} = 1.6$: this nonlinearity is too strong for the system. As a result, the Hopf bifurcation becomes sub-critical again and the isolated solution moves towards higher airspeeds. This absorber has an effect similar to that of the LTVA except that the pitch has lower amplitude and the flap has higher amplitude because of the isola/main branch inversion.

Computing many continuation curves similar to those in figure 3.8 for different values of c_{nl} and plotting the onset speed of the main and isolated branches as a function of c_{nl} yields the results displayed in figure 3.9. At $c_{nl} = 0$, the isola is located at infinity and the LCO onset speed is equal to that of the LTVA. As the nonlinear coefficient is increased, the LCO onset speed of the isola decreases and that of the main branch increases until they nearly merge around $c_{nl} = 1.25$ m^{-2}, where the Hopf bifurcation that gives rise to the main branch becomes super-critical. Increasing the nonlinear parameter further leads to an increase in the LCO onset speed of the isolated solution branch and to a decrease of that of the main branch. Note that unlike in a similar study performed on a wing with pitch and plunge DOFs [115], the LCO onset speed of the isola is never smaller than that of the main branch.

Similar observations are made in figure 3.10 which depicts the LCO onset amplitude variation with c_{nl}. Again, for small nonlinear parameters, the isola has very high onset amplitude and the main branch has high onset amplitude because the Hopf bifurcation is sub-critical. In the vicinity of $c_{nl} = 1.25$ m^{-2} the LCO onset amplitude of the main branch drops to zero because the bifurcation becomes super-critical and the LCO onset amplitude of the isolated branch almost drops to zero where it nearly merges with the main branch. For higher values of c_{nl}, the LCO onset amplitude increases because the bifurcation becomes sub-critical again. Note that the onset amplitude of the main branch jumps down to zero before the optimum while that of the isolated branch jumps up from zero after the optimum.

Figure 3.11 plots the basin of attraction of the system with $c_{nl} = 1.25$ at airspeeds of 16, 19 and 22 m/s. Initial conditions in pitch and flap ranging from -50 deg to 50 deg where considered, with the other 8 states set to zero. Surprisingly, none of the simulations

landed onto the main branch, which indicates that its basin of attraction is very small and that it is very unlikely to observe this branch in practice. Note that the main branch was found by computing hundreds of direct simulations with random initial conditions on all ten states.

Figures 3.12 depicts similar basins of attractions for a nonlinear coefficient of 2.0 at airspeeds of 18, 22 and 24 m/s. At 18 m/s, small initial conditions land onto the main branch while large ones land onto the isolated branch. At 22 m/s, the main branch attractor area close to the origin shrinks and narrow regions arise at higher initial angles. At 24 m/s, small initial angles are attracted by the isola and a complex shape is observed.

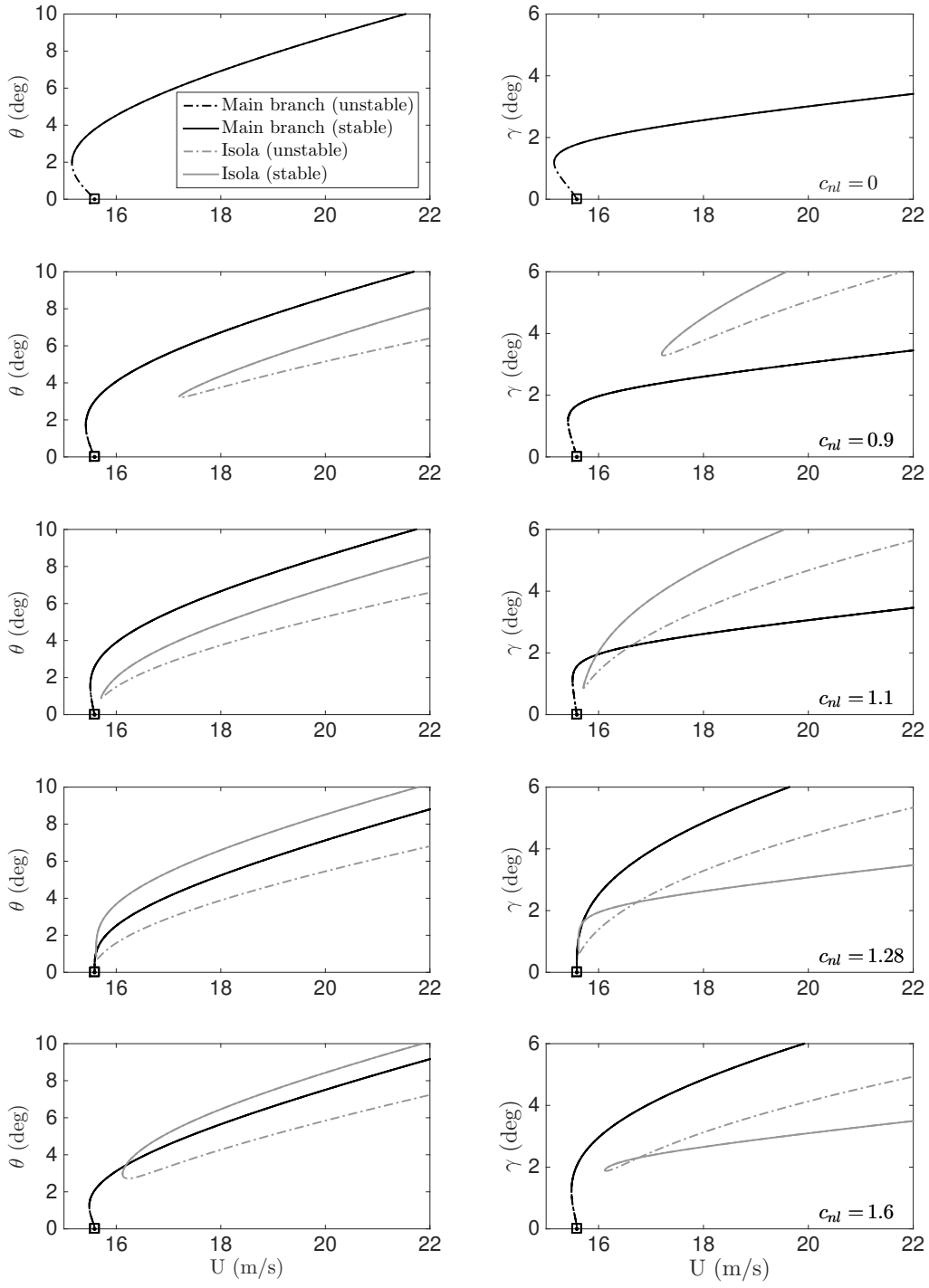

Figure 3.8: Bifurcation diagrams of the NLPFW with a NLTVA attached. Each row corresponds to one value of the nonlinear stiffness parameter.

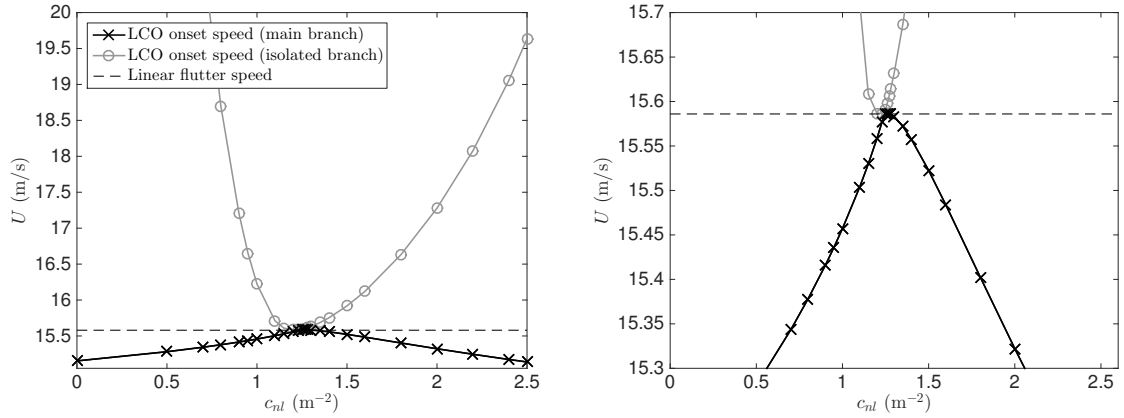

(a) Overview (b) Zoom

Figure 3.9: Variation of the onset speed of the main and isolated solution branches

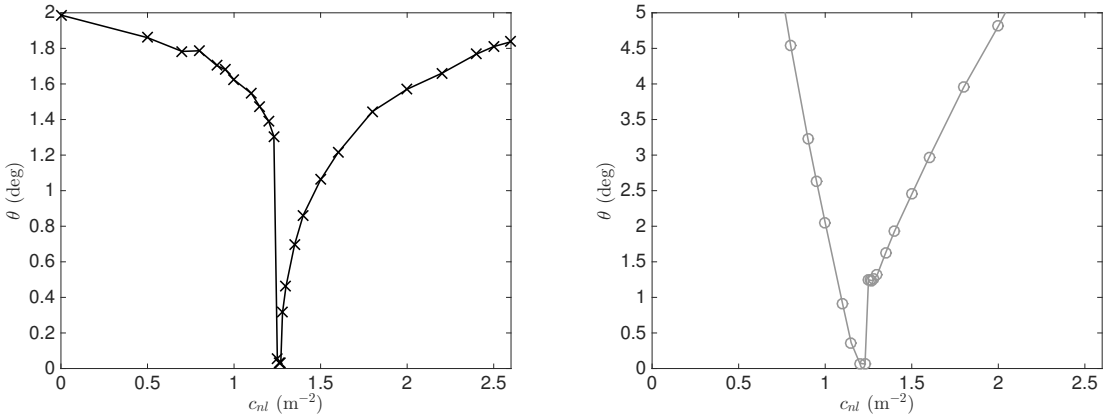

(a) Main branch (b) Isolated branch

Figure 3.10: Variation of the onset amplitude in pitch of the main and isolated solution branches

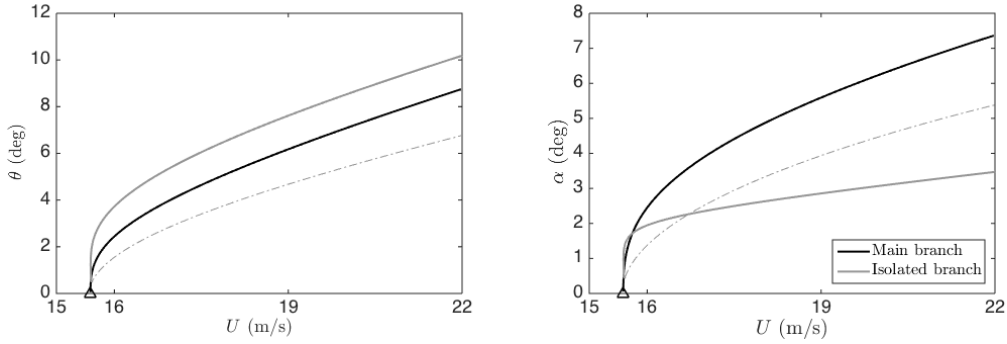

Figure 3.11: Basin of attraction of the system with $c_{nl} = 1.25$ m^{-2}. All the simulations with $|\alpha_0| < 50°$ and $|\gamma_0| < 50$ are attracted by the isolated solution branch.

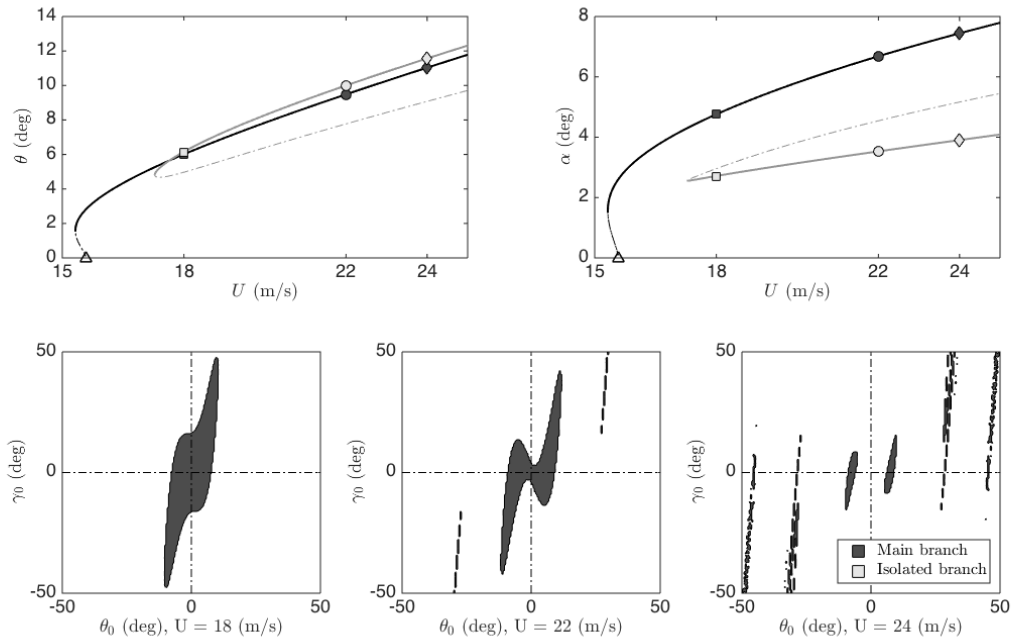

Figure 3.12: Basin of attraction of the system with $c_{nl} = 2.0$ m^{-2}

3.5 Experimental absorber validation

3.5.1 Linear absorber design and identification

Using the numerical results to design the absorber is very challenging. The model indeed underestimates the LCO frequency by 0.3 Hz and it showed that a very fine tuning of the absorber was needed in terms of frequency as a detuning of only 0.1 Hz lead to a decrease in performance of 30%. Nevertheless, the model provided design guidelines which are that the absorber should feature high modal damping ($\approx 15\%$) and relatively low frequency (≈ 1.9 Hz according to the model).

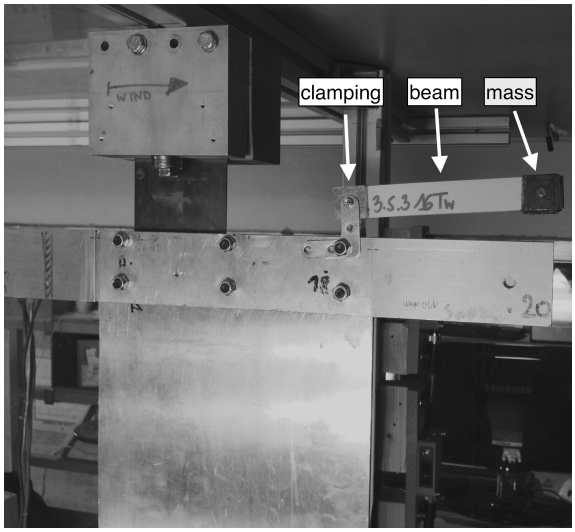

Figure 3.13: Picture of the system with a LTVA attached

To achieve such a low frequency with an absorber mass of 64 (or 70) grams, the LTVA has to provide a small restoring force and no Coulomb friction to avoid sticking phenomena. The adopted solution is a 100 mm long and 20 mm wide cantilever beam. It is made of a sandwich of three layers of PVC sheets of thicknesses of 0.3 or 0.5 mm, with up to 16 layers of viscoelastic tape around the central beam. This design avoids significant Coulomb friction as no bearings are used however frequencies lower than 2.5 Hz cannot be achieved because the beam buckles if its stiffness is too low. Moreover, the tape layers increase the thickness of the beam so the frequency and the damping could not be modified independently. The absorbers are attached to the primary system as displayed in figure 3.13, in a configuration similar to the one that was studied numerically i.e. 100 mm long beam, placed at 125 mm from the pitch axis and 50 mm from the flap axis.

Table 3.2 summarises the characteristics of the different absorbers tested, denoted by

Absorber	Beam sandwich [mm]	Tape layers [-]	Mass [grams]
A	$0.3 - 0.5 - 0.3$	10	70
B	$0.3 - 0.5 - 0.3$	10	64
C	$0.3 - 0.3 - 0.3$	16	64
D	$0.3 - 0.5 - 0.3$	16	64
E	$0.5 - 0.3 - 0.5$	16	64

Table 3.2: Characteristics of the experimental absorbers

A to E. LTVAs A and B use the same beam with a different mass while the other four feature different beams. The identification of the absorbers was performed using free decay signals with a peak-picking routine for the frequency measurements and the logarithmic decrement technique for the damping. As the damping was quite high, only short time-series could be measured so 20 free decays were induced for each absorber. Figures 3.14 and 3.15 respectively show examples of identifications performed on absorbers A and E. The signals measured (figures 3.14(a) & 3.15(a)) were separated in cycles whose durations were used to estimate the frequencies. The large asymmetry observed with absorber E is due to the high damping in the structure. To accurately apply the logarithmic decrement technique, an average cycle amplitude defined as half of the difference between the highest and the lower point of the cycle was used in lieu of the classical maximum tracking. Figures 3.14(b) & 3.15(b) and 3.14(c) & 3.15(c) respectively depict the frequency and damping rate of each cycle for absorbers A and E. All the periods have frequencies within less than 0.1 Hz and damping rates within less than 1% of each other which is sufficiently accurate for our application.

Figure 3.16 plots the results of the identification of all the absorbers, with the measurements in grey, and the average and standard deviations indicated in black. Absorber A exhibits a damping of 6.8% and a frequency of 2.65 Hz on average, while absorber B features a similar damping and a frequency around 2.8 Hz. Absorbers C, D and E contain 16 layers of tape which increase their damping by about 2% compared to the first two but which also increase their frequencies to 3, 3.2 and 4 Hz, respectively. This identification illustrates the difficulty of designing an absorber that features both high damping and low frequency, as the absorbers with 10 tape layers clearly have a lower frequency.

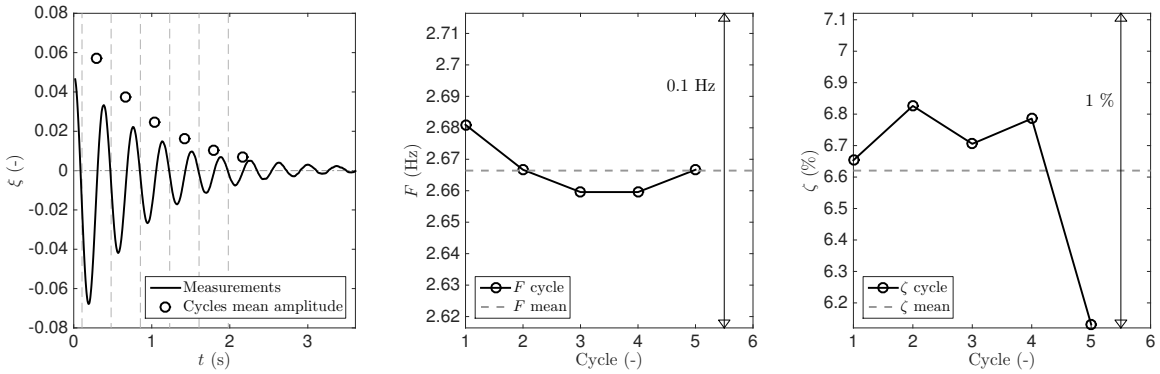

(a) Free-decay signal (b) Cycles frequency (c) Cycles damping

Figure 3.14: Experimental identification of absorber A

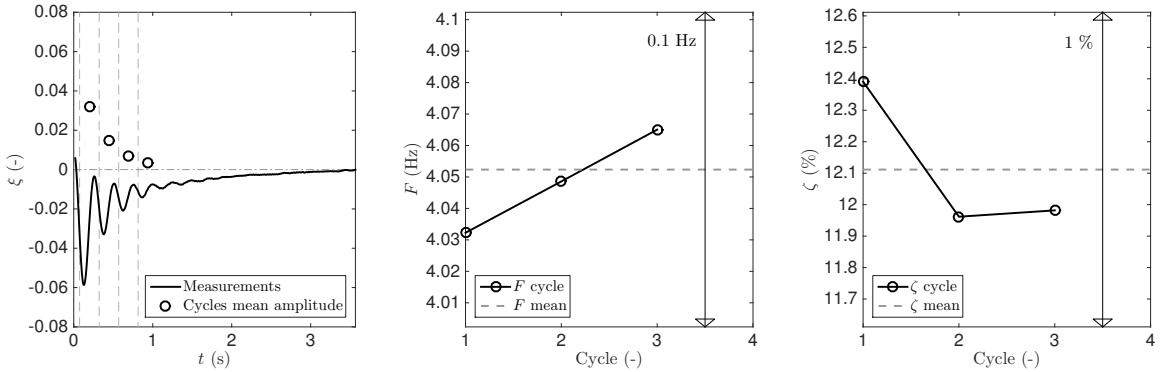

(a) Free-decay signal (b) Cycles frequency (c) Cycles damping

Figure 3.15: Experimental identification of absorber E

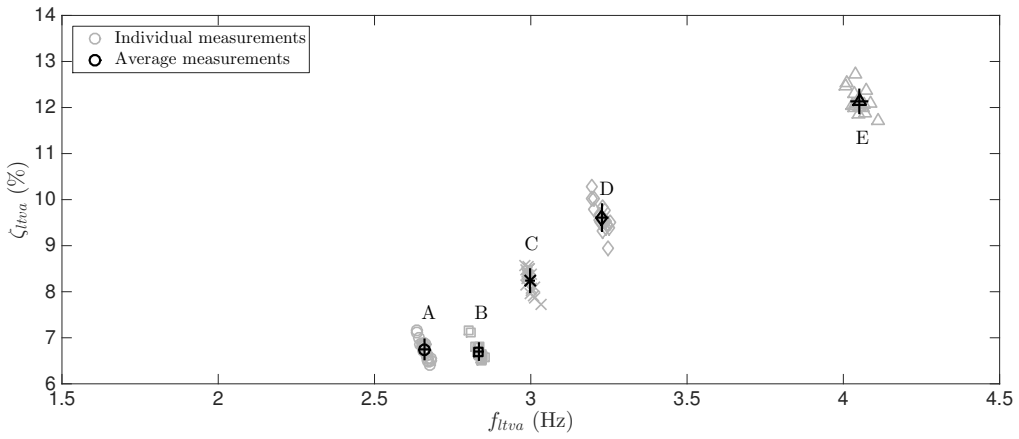

Figure 3.16: Experimental identification of the absorbers

3.5.2 Effect of the absorber on the flutter speed of the system

Figure 3.17 displays the ratio between the flutter speed of the system with and without absorber as a function of the LTVA's frequency, which is the most critical tuning parameter. The lines correspond to the numerical predictions of figure 3.2, where each curve was computed using a different damping value, while the points are related to the experimental measurements. In some cases, the wind tunnel controller induced a jump in the airspeed, thus decreasing the accuracy of the corresponding experimental flutter speed estimates. This phenomenon is indicated by the vertical error lines in the figure. The experiments showed that the lower the LTVA frequency, the higher the flutter speed irrespective of the damping. The best absorber tested increases the flutter speed by about 36%, which is similar to the numerical predictions. It is not known if this increase is optimal as it was not possible to build absorbers with lower frequencies. Besides the difference in optimal absorber frequency, the biggest difference between the model and the experiments is the beneficial effect of the absorbers even when considerably detuned. Absorber E indeed increases the flutter speed by 12.5% while, according to the model, an equally detuned absorber should lead to an improvement of only 4.4%, assuming the damping is properly tuned for that frequency.

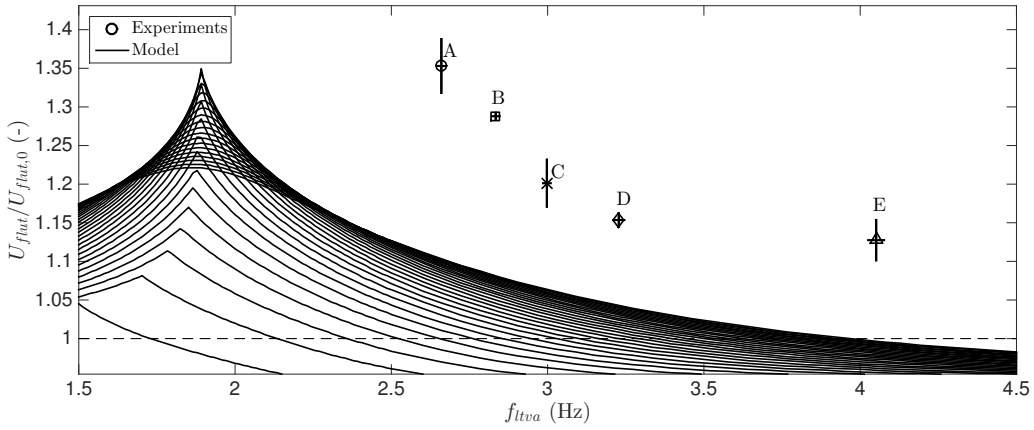

Figure 3.17: Effect of the LTVA on the system's flutter speed

3.5.3 Effect of the absorber on the post-critical response of the system

Figure 3.18 depicts experimentally measured pitch, flap and frequency bifurcation diagrams obtained with LTVAs A, B and C, compared to the bifurcation diagram of the baseline system without absorber.

The pitch bifurcation diagram (figure 3.18(a)) shows that absorber C (dashed dotted line and squares) delays flutter by 2 to 3 m/s then dramatically reduces the LCO amplitude compared to the baseline case (solid line and crosses). Absorber B (dashed line and circles) increases even more the flutter speed, ($\approx$ 14.9 m/s) because its frequency is lower than that of absorber C. Absorber A (solid line and triangles), which features the smallest frequency of all three absorbers, pushes flutter to about 15.5 m/s. Once the instability occurs, all three absorbers lead to a similar amplitude growth with airspeed, which is much slower than that of the reference case. This is consistent with the model predictions for super-optimal absorbers. No detuning was observed in the velocity range of the tests. This means that all the experimental absorbers are significantly superoptimal, which is logical since their frequencies were at least 0.5 Hz higher than those of the simulated absorbers. Absorbers D and E have an effect on the response similar to that of absorbers A, B and C except that flutter occurs at a lower airspeed. The bifurcation diagrams for these absorbers are not displayed to avoid overloading the figure. Finally, all five absorbers suppressed the hysteresis phenomenon and the amplitude jump in the airspeed range of the tests.

Figure 3.18(b) depicts the flap bifurcation diagram. The observations regarding the performance of the LTVAs are similar to those for the numerical model. The absorbers delay the LCOs however they lead to a faster growth in amplitude in flap compared to the baseline system. Again, this is consistent with the earlier observation that all absorbers are super-optimal.

Finally, the frequency bifurcation diagram is displayed in figure 3.18(c) and once again the observations are similar to the predictions of the model. All three absorbers dramatically reduce the LCO frequency and its growth with airspeed. Moreover the closer the absorber to the optimum, the lower the frequency.

In summary, all three absorbers increased the flutter speed by 20 to 36%, decreased the pitch LCO amplitude but increased the amplitude growth with airspeed of the flap.

All the absorbers also suppressed the amplitude jumps in the airspeed range of the tests. Even the worst absorber led to a decrease in LCO amplitude of 50 to 70% while the best one decreased the amplitude by a factor of 5 in the velocity range of the tests.

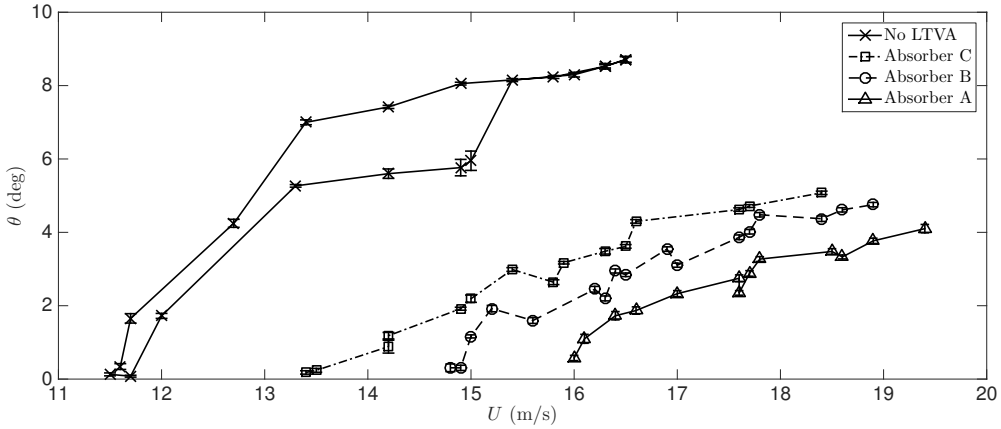

(a) Pitch LCO amplitude

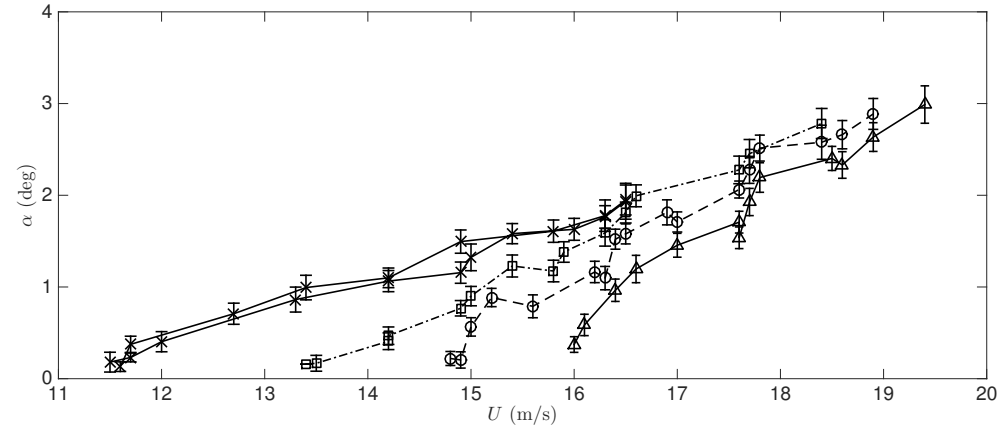

(b) Flap LCO amplitude

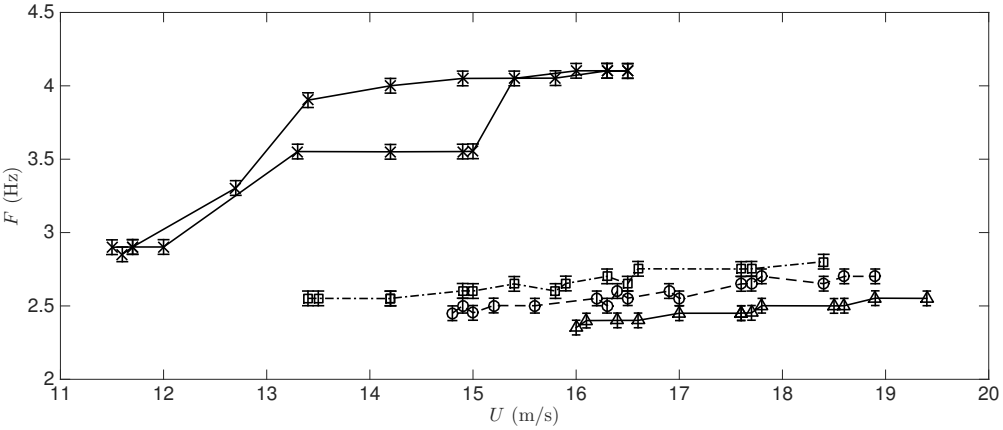

(c) LCO frequency

Figure 3.18: Experimental bifurcation diagrams of the system with different LTVA tunings.

3.6 Chapter summary

In this chapter, the beneficial effects of linear and nonlinear tuned vibration absorbers on the primary system's response are addressed.

Linear flutter analysis performed on the mathematical model suggests that the absorber considered in this study can increase the flutter speed by 35% for a mass ratio of only 2.37%. Optimal tuning is achieved when two of the system modes flutter at the same airspeed. Nevertheless, no simple tuning rule similar to that of Den Hartog for mechanical vibration was found because of the amount of relevant parameters. As expected, the model predicts that the absorber's mass and length should be as large as possible and that the absorber should be located as far as possible from the pitch and flap axes.

Nonlinear bifurcation analysis performed on the mathematical model highlighted that the optimally-tuned LTVA turns the super-critical Hopf bifurcation into sub-critical because the absorber is only effective at small amplitudes. The bi-stability introduced by the sub-critical bifurcation reduces the LCO onset speed and can be dangerous for practical applications because it leads to large LCO onset amplitudes. The addition of a properly tuned nonlinearity in the absorber can restore the super-criticality of the bifurcation and eliminate the bi-stability. However, the nonlinear force also gives rise to an isolated solution that can substantially increase the pitch or flap amplitude of the LCOs. Furthermore, this isolated branch has a basin of attraction much larger than that of the main branch and cannot therefore be neglected.

Finally, wind tunnel tests demonstrated experimentally the beneficial effect of the LTVA on the system response. The absorbers tested here increased the flutter speed by up to 35%, substantially decreased the LCO amplitude and suppressed the amplitude jump induced by stall flutter in the airspeed range of the tests. The flutter speed variation with LTVA frequency observed experimentally follows a trend similar to that of the numerical model however we were not able to design optimal and sub-optimal absorbers because buckling of the LTVA beam prevented us from building sufficiently soft absorbers. As a result, the bi-stability was not observed and the effect of the addition of a nonlinear force to the absorber could not be demonstrated.

Chapter 4

Analysis and modelling of a pitch-plunge-control wing

4.1 Introduction

Now that the performance and the tuning methodology of linear and nonlinear tuned vibration absorbers has been studied on one of the simplest nonlinear aeroelastic systems possible, the goal is to assess the performance of such absorbers in a more complex case: systems featuring freeplay. The system considered is a typical aeroelastic section similar to that introduced by Tang et al. and used in numerous studies since [40–47]. This wing features degrees of freedom in pitch, plunge and control surface deflection. In this work, however, the freeplay nonlinearity is located in the pitch DOF in lieu of the control surface.

This system is more challenging than the pitch and flap wing for several reasons. It features an additional DOF and therefore an additional vibration mode that might participate in the flutter mechanism. Up to three fixed points around which limit cycle oscillations can orbit might exist while the pitch and flap wing only had one fixed point. The nonlinearity is nonsmooth and generates impacts, leading to a broader frequency content than cubic nonlinearity. Furthermore, the time integration of the equations of motion of such systems requires appropriate numerical methods with event detection. Finally, the system is strongly nonlinear at small energy levels and weakly nonlinear at high energy levels while the pitch and flap wing was weakly nonlinear at small amplitudes of oscillation.

The chapter consists of three main parts. After a theoretical background, the experimental apparatus is described and tested in the wind tunnel of Duke University. Then a

mathematical model is proposed and compared to the experimental results.

4.2 Theoretical background

4.2.1 Equations of motion of an aeroelastic system with freeplay and preload

The pitch-plunge-control aeroelastic system is a 2D symmetric flat plate wing with a control surface. The entire wing is suspended by an extension spring with stiffness K_h and a rotational spring of stiffness K_θ from its pitch axis x_f. These two springs provide restoring forces in the plunge, h, and pitch, θ, DOFs respectively. The control surface deflection angle β is an additional DOF, restrained by a rotational spring with stiffness K_β. The control surface hinge lies at x_h and the total chord of the wing is denoted by c. The complete system is shown in figure 4.1

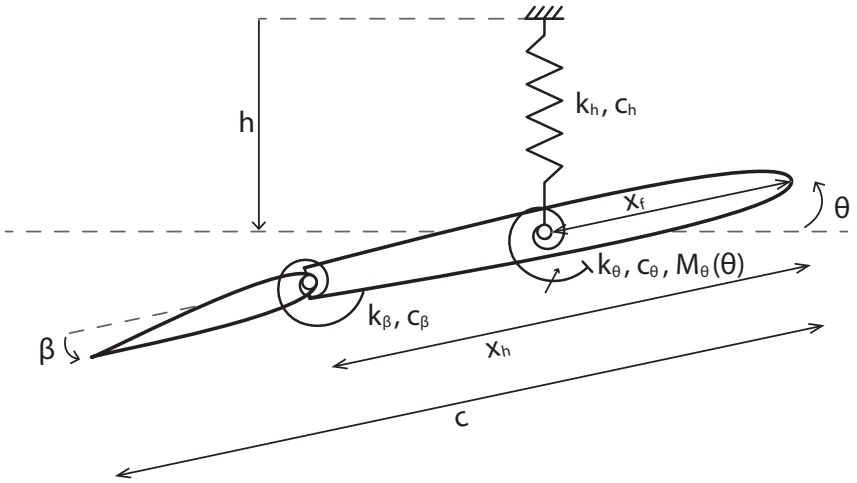

Figure 4.1: Pitch-plunge-control aeroelastic system

It is assumed that there is freeplay in the pitch DOF, such that the restoring force in the corresponding spring is zero while $|\theta| < \delta$, 2δ being the width of the freeplay region. Figure 4.2 shows a typical restoring force diagram for freeplay, whereby the stiffness is K if $|\theta| > \delta$ and zero otherwise. Note that the freeplay region is centred around the origin.

In the case of the pitch-plunge-control wing with freeplay in the pitch DOF, the stiffness outside the freeplay region is given by K_θ, while the stiffness inside the freeplay

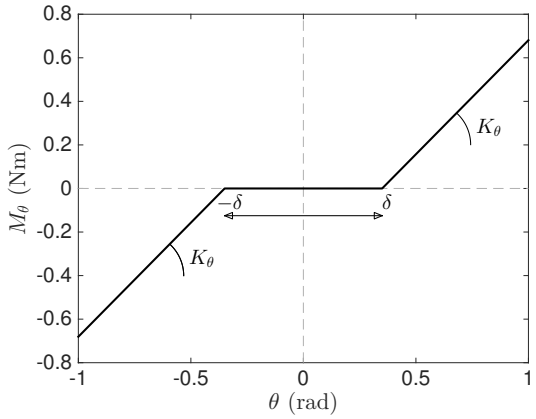

Figure 4.2: Freeplay stiffness diagram

region is zero. The restoring moment equation is

$$M_\theta(\theta) = \begin{cases} K_\theta(\theta + \delta) & \text{if} \quad \theta < -\delta \\ 0 & \text{if} \quad |\theta| \leq \delta \\ K_\theta(\theta - \delta) & \text{if} \quad \theta > \delta \end{cases} \tag{4.1}$$

where M_θ is the pitching moment provided by the freeplay spring.

In addition to the freeplay, an aerodynamic preload angle θ_p is considered. It models the fact that when the wing is perfectly centred in the freeplay region, it is not perfectly aligned with the airflow and vice versa. As a result, the structural moment, M_θ, depends on $\theta(t)$ while the aerodynamic moment, M_{aero}, depends on $\theta_{tot} = \theta_p + \theta(t)$, which introduces an asymmetry in the system.

The equations of motion of the system flying with airspeed U in air of density ρ can be developed using linear unsteady attached flow aerodynamic assumptions; a time-domain model can be written by means of Wagner function analysis [40, 116, 117]. The structural displacements are denoted by vector $\mathbf{y} = [h \quad \theta \quad \beta]$ while the six aerodynamic states are denoted by vector $\mathbf{w} = [w_1 \quad \dots \quad w_6]$. Then the complete state vector of the system is given by $\mathbf{x} = [\dot{\mathbf{y}} \quad \mathbf{y} \quad \mathbf{w}]^T$ and has dimensions 12×1. The equations of motion of the system with freeplay and aerodynamic preload in the pitch DOF are given by

$$\dot{\mathbf{x}} = \mathbf{Q}_1\mathbf{x} + \mathbf{q}_n M_\theta(\theta) + \mathbf{q}_p\theta_p \tag{4.2}$$

where

$$\begin{aligned}
\mathbf{Q}_1 &= \begin{pmatrix} -\mathbf{M}^{-1}(\mathbf{C}+\rho U\mathbf{D}) & -\mathbf{M}^{-1}(\mathbf{E}_1+\rho U^2\mathbf{F}) & -\rho U^3\mathbf{M}^{-1}\mathbf{W} \\ \mathbf{I}_{3\times3} & \mathbf{0}_{3\times3} & \mathbf{0}_{3\times6} \\ \mathbf{0}_{6\times3} & \mathbf{W}_1 & U\mathbf{W}_2 \end{pmatrix} \\
\mathbf{q}_n &= \begin{pmatrix} -\mathbf{M}^{-1}\begin{pmatrix} 0 \\ 1 \\ 0 \end{pmatrix} \\ \mathbf{0}_{9\times1} \end{pmatrix} \\
\mathbf{q}_p &= \begin{pmatrix} \rho U^2\mathbf{M}^{-1}\boldsymbol{P} \\ \mathbf{0}_{9\times1} \end{pmatrix}
\end{aligned} \tag{4.3}$$

and $\mathbf{E}_1$, is the value of the structural stiffness matrix inside the freeplay region $\pm\delta$, given by

$$\mathbf{E}_1 = \begin{pmatrix} K_h & 0 & 0 \\ 0 & 0 & 0 \\ 0 & 0 & K_\beta \end{pmatrix} \tag{4.4}$$

Matrix $\mathbf{C}$ is the structural damping matrix, $\rho U\mathbf{D}$ is the aerodynamic damping matrix, $\rho U^2\mathbf{F}$ is the aerodynamic stiffness matrix, $\mathbf{W}$ is the aerodynamic state matrix, $\mathbf{W}_1$ and $\mathbf{W}_2$ are the aerodynamic state equation matrices, $\mathbf{M} = \mathbf{A} + \rho\mathbf{B}$, $\mathbf{A}$ is the structural mass matrix and $\mathbf{B}$ is the aerodynamic mass matrix. Matrix $\mathbf{P}$ is an aerodynamic stiffness vector that takes into account the effect of preload angle θ_p on the loads acting on the system. The notation $\mathbf{I}_{3\times3}$ denotes a unit matrix of size 3×3. The values of all the matrices are given in Appendix D. Equation 4.2 can be written as

$$\dot{\mathbf{x}} = \begin{cases} \mathbf{Q}_1\mathbf{x} + \mathbf{q}_p\theta_p & \text{if} \quad |\theta| \le \delta \qquad \text{(a)} \\ \mathbf{Q}_2\mathbf{x} - \mathbf{q}_n K_\theta \operatorname{sgn}(\theta)\delta + \mathbf{q}_p\theta_p & \text{if} \quad |\theta| > \delta \qquad \text{(b)} \end{cases} \tag{4.5}$$

where $\mathbf{Q}_2\mathbf{x} = \mathbf{Q}_1\mathbf{x} + \mathbf{q}_n K_\theta\theta$.

In this work, we will define two linear sub-systems that are relevant to freeplay:

- Underlying linear system: the system without structural stiffness that is only valid inside the freeplay region (equation 4.5(a)).
- Overlying linear system: the nominal system without freeplay and with full stiffness

(equation 4.5(b) with $\delta = 0$).

4.2.2 Fixed points

The freeplay function of figure 4.2 splits the phase plane of the system responses into three piecewise linear subdomains, S_1 for $|\theta| \leq \delta$, S_2 for $\theta > \delta$ and S_3 for $\theta < -\delta$. Response trajectories can span one, two or all three of the subdomains. Furthermore, equation 4.2 has three fixed points given by

$$\begin{aligned} \mathbf{x}_{F_1} &= -\mathbf{Q}_1^{-1}\mathbf{q}_p\theta_p \quad \text{if} \quad |\theta| \leq \delta \\ \mathbf{x}_{F_2} &= \mathbf{Q}_2^{-1}\left(\mathbf{q}_n K_\theta \delta - \mathbf{q}_p\theta_p\right) \quad \text{if} \quad \theta > \delta \\ \mathbf{x}_{F_3} &= -\mathbf{Q}_2^{-1}\left(\mathbf{q}_n K_\theta \delta + \mathbf{q}_p\theta_p\right) \quad \text{if} \quad \theta < -\delta \end{aligned} \tag{4.6}$$

i.e. they depend on the aerodynamic preload θ_p, the freeplay gap δ and the airspeed U. These fixed points do not coexist; only one of them is an attractor at any instance in time, depending on which subdomain the response trajectory lies in. Dividing equations 4.6 throughout by δ we obtain non-dimensional fixed points $\bar{\mathbf{x}}_{F_i} = \mathbf{x}_{F_i}/\delta$ that only depend on the airspeed and the ratio of the aerodynamic preload divided by the freeplay gap, θ_p/δ.

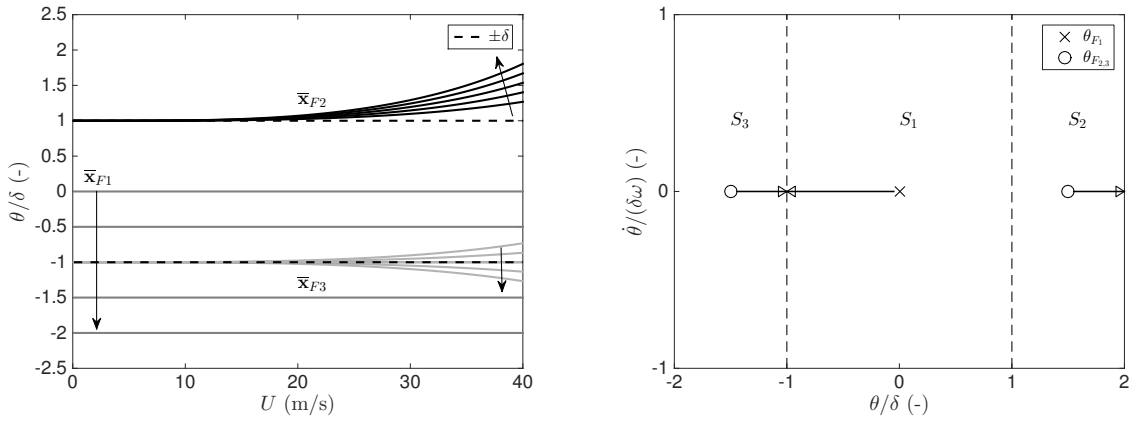

(a) Fixed points

(b) Boundary-equilibrium bifurcation

Figure 4.3: Positions of fixed points with varying airspeed and θ_p/δ ratio

Figure 4.3(a) plots the pitch component of the three fixed points for airspeeds between 0 and 40 m/s and for θ_p/δ ratios between 0 and 2. It can be seen that, as the aerodynamic preload ratio increases, fixed point $\overline{\mathbf{x}}_{F_1}$ moves from 0 to -1 and eventually exits the freeplay region. Similarly, $\overline{\mathbf{x}}_{F_3} = 1$ for all airspeeds when $\theta_p/\delta = 1$ and enters the freeplay

region for all $\theta_p/\delta > 1$. This means that only $\overline{\mathbf{x}}_{F_2}$ exists for $\theta_p/\delta > 1$, since $\overline{\mathbf{x}}_{F_1}$ and $\overline{\mathbf{x}}_{F_3}$ violate the conditions for existence given in equations 4.6.

As the aerodynamic preload increases, the system bifurcates from a system with three fixed points to a system with 1 fixed point. This bifurcation is known as a boundary-equilibrium bifurcation and occurs when $\theta_p = \delta$ and $\mathbf{x}_{F_1} = \mathbf{x}_{F_3} = -\delta$ for all airspeeds. The bifurcation can be more easily visualised in the phase plane plot of figure 4.3(b). The system's fixed points are plotted in the θ-$\dot{\theta}$ plane for $\theta_p = 0$ and $U \neq 0$. Symbols $\theta_{F_{1,2,3}}$ denote the pitch components of fixed points $\mathbf{x}_{F_{1,2,3}}$. The arrows denote the motion of the fixed points as θ_p is increased. As mentioned earlier, the freeplay region divides the phase plane into three subdomains: S_1 inside the freeplay boundaries at ± 1, S_2 and S_3 outside. Each fixed point is only defined inside its respective subdomain. The arrows show that, as θ_p increases, fixed points $\mathbf{x}_{F_1}$ and $\mathbf{x}_{F_3}$ collide with the $-\delta$ boundary and disappear. Another boundary-equilibrium bifurcation occurs at $U = 0$, where $\mathbf{x}_{F_2} = \delta$, $\mathbf{x}_{F_3} = -\delta$ for all values of the aerodynamic preload ratio.

The fixed points of systems with piecewise linear stiffness display a transient characteristic. In the present case there are three piecewise linear subdomains and three piecewise linear systems. The fixed point of each system exists and attracts the response trajectory while the latter lies in the corresponding subdomain. There are two types of fixed point:

- Fixed point of system in S_i that lies in subdomain S_i.
- Fixed point of system in S_i that lies in another subdomain.

The first type of fixed point can attract static solutions, i.e. the system response can decay towards it (or, if the response trajectory starts on the fixed point it will stay on it forever). The second type of fixed point cannot attract static solutions and therefore is not a fixed point in the classic sense. However, it can still attract dynamic solutions while the response trajectory travels through subdomain S_i. The present discussion of the boundary-equilibrium bifurcation only concerns static solutions. Indeed, when a fixed point crosses a discontinuity boundary into the wrong subdomain it cannot attract static solutions anymore. It disappears in a static sense but it still affects the response intermittently every time a trajectory enters the relevant subdomain.

4.2.3 Two-domain and three-domain limit cycles

It is reasonable to make the assumption that the overlying (i.e. nominal) linear system is flutter-free and divergence-free inside its flight envelope and that any aeroelastic instabilities are due to the freeplay. Furthermore, it will be assumed that the flutter speed of the underlying linear system U_{F_1} is lower than that of the overlying linear system, U_{F_2}. Two types of periodic solution are then possible:

- Circles: These exist entirely in the S_1 subdomain and can only occur at the flutter point of the underlying linear system, i.e. when $U = U_{F_1}$.
- Limit cycles: These must span at least two subdomains as they can only exist if the system response is nonlinear. They can exist at a range of airspeeds.

The circles and limit cycles are related; the circles bifurcate into limit cycles when their amplitude becomes equal to the width of the freeplay boundary, as displayed in figure 4.4(a). This bifurcation is known as a grazing bifurcation (see for example [118]). Limit cycles that span two domains, i.e. S_1 and S_2 or S_1 and S_3 are referred to as two-domain cycles. Limit cycles that span all three domains are referred to as three-domain cycles. Figure 4.4(b) plots both types of limit cycle. In the absence of aerodynamic preload, it can be seen that a three-domain cycle will orbit $\mathbf{x}_1$ and $\mathbf{x}_{2,3}$ if they exist. In contrast, a two-domain cycle can only orbit either $\mathbf{x}_2$ or $\mathbf{x}_3$. It follows that two-domain cycles can only exist if the fixed points $\mathbf{x}_{2,3}$ also exist.

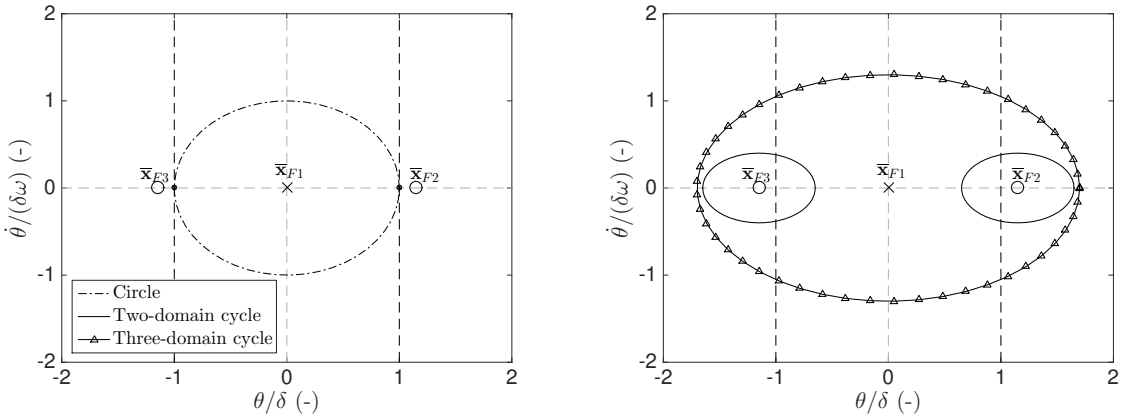

(a) Grazing bifurcation

(b) Two-domain and Three-domain cycles

Figure 4.4: Grazing bifurcation of the symmetric system

4.3 Experimental setup

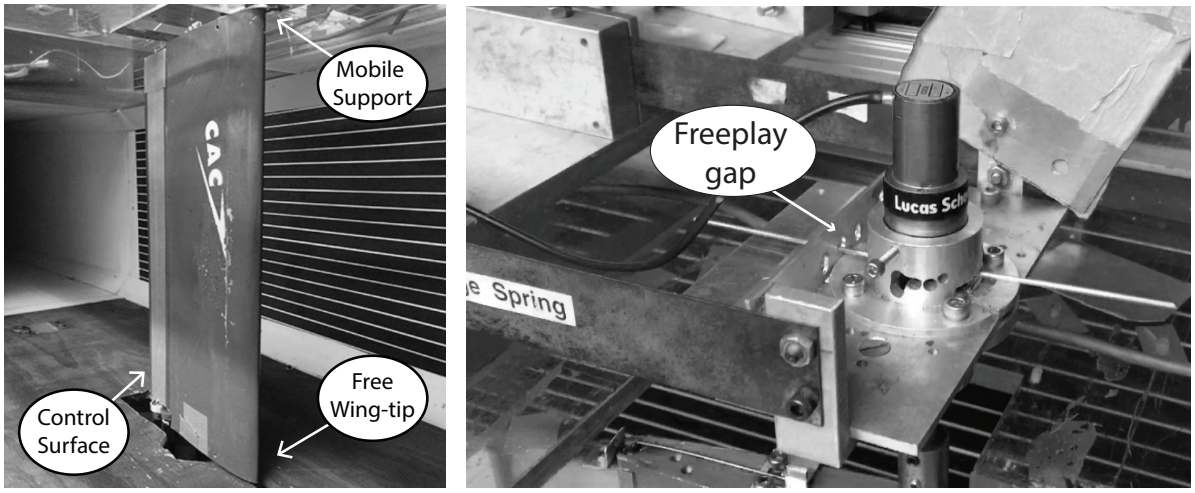

(a) Wing in the test section of the wind tunnel

(b) Mobile support structure

Figure 4.5: Photograph of the experimental apparatus

The experimental system consists of a wing with pitch, plunge and control DOFs mounted vertically in the low-speed wind tunnel of Duke University. The two tips of the wing lie very close to the tunnel wall, so that the flow can be considered quasi-2D. For this study, the freeplay is placed in the pitch DOF. The wing is a NACA 0012 with span 52cm and chord 19cm with a flap of chord 6.35cm mounted to the wing's trailing edge with micro-bearings and a pin. The model is quite similar to the one used by Conner et al. [40], however the support system and internal structures are also different so the dynamic behaviours of the two models are different. The restoring force in the control DOF is provided by a thin piano wire glued to the pin and clamped on the main wing. The wing is attached to the mobile support structure by means of a single spar located at $x_f = 0.25c$ and two bearings placed on the support. Tightening screws allow the user to change the alignment of the wing in the test section to modify the aerodynamic preload angle θ_p. In this paper, angles of approximately 0 and 5 degrees are considered. Another piano wire is used to provide the necessary restoring torque in pitch. Finally, the mobile support is clamped to the wind tunnel by means of two leaf springs that provide restoring force in the plunge DOF.

Five configurations of pitch restoring forces are considered. Firstly the wire was clamped without any freeplay in order to study the overlying linear system. Then the wire was inserted into plates with holes of different dimensions in order to introduce different amounts

of freeplay. The nominal freeplay ranges, defined as the nominal angular distance between the two ends of the freeplay range, considered in this study are given in table 4.1, along with the measured freeplay ranges and the corresponding values of δ. The freeplay range measurements were obtained using a pitch angular sensor, by moving the piano wire manually between the two ends of the freeplay range. This type of measurement is prone to experimental error therefore a range of values is given in the table.

Nominal freeplay (deg)	Measured freeplay (deg)	δ (deg)
1	0.6 - 0.9	0.3 - 0.45
2	1.8 - 2.0	0.9 - 1
3	3.1 - 3.2	1.55 - 1.6
8	7.4 - 7.6	3.7 - 3.8

Table 4.1: Nominal freeplay of the system

The structural parameters of the system, given in appendix B, were identified using different techniques. The inertia and stiffness of the different components were measured statically while dynamic tests were performed for validation and for damping computation. Modal analysis performed using the least squares complex exponential method [119] at several airspeeds on the overlying linear system highlighted the following modal characteristics:

- The plunge-dominated mode has a frequency of 2.9 Hz and a damping of 0.87 % at wind-off conditions. Increasing the airspeed has a hardening effect that makes it interact with the pitch mode.
- The pitch-dominated mode's wind-off frequency is 7.1 Hz and its damping is equal to 1.39 %. The airflow has a softening effect on this mode that helps the interaction with the plunge mode.
- The flap-dominated mode lies at 17 Hz at wind-off with a damping of 0.6 %. The airspeed has a softening effect on this mode, however its frequency is too high to allow interactions with any of the other modes in the airspeed range considered here.

A flutter test performed on the overlying linear system showed that hard flutter occurs at 27-28 m/s due to the interaction of the pitch and plunge modes. All the experiments with freeplay are performed at airspeeds between 8 and 20 m/s, which lie far below the flutter speed of the overlying linear system and are therefore safe.

The instantaneous pitch angle is measured using a meas-spec R30D rotation sensor with a sensitivity of 0.125 mV/deg. A meas-spec R30A angular sensor with sensitivity 0.02 mV/deg is used to measure the flap angle because of its smaller size. Finally an ultrasound sensor with a sensitivity of 10 V/m measures the plunge displacement. The airspeed in the wind tunnel is measured in real time using a hot wire probe. The data from all these instruments are acquired simultaneously on a NI CompactDAQ with a sampling frequency of 1 kHz. All the signals are 20 seconds long and low-pass filtered at 45 Hz in order to remove electrical noise.

4.4 Post-critical aeroelastic investigation

Figures 4.6(a) and 4.6(b) plot the pitch amplitude and frequency of the limit cycles obtained without aerodynamic preload ($\theta_p \approx 0$) for all airspeeds and freeplay cases. The largest three freeplay values (2, 3 and 8 deg) exhibit similar behaviour as all the amplitude and frequency results fall on a single curve for each of the three freeplay values, as already highlighted by numerous previous studies on freeplay. For the smallest freeplay gap (stars), the results are slightly different. In this case, the amplitude ratio and the LCO onset speed are higher than in the other cases and the LCO frequency is slightly lower. These differences are attributed to the nonlinear friction in the bearings and to the geometry of the freeplay gap. Marsden and Price observed a similar effect on a pitch-plunge system with freeplay and bearings in the pitch [32]. In all four cases, the system undergoes a slow and almost linear amplitude increase with airspeed once the oscillations have started. The LCO frequency features a main branch that starts at about 3.3 Hz and increases to up to 4.2 Hz. The points with frequencies under 3 Hz arise from a secondary peak observed in the Fast Fourier Transforms (FFT) of quasi-periodic oscillations.

The amplitude bifurcation diagram presented in fig. 4.6(a) plots the peak-to-peak amplitude of the measured response signals and misses an important part of the dynamics: the existence of two-domain and three-domain LCOs. Figure 4.7 plots pitch time history responses of the system with a freeplay gap of 3 deg and without aerodynamic preload. At 11.9 m/s, the system undergoes quasi-periodic limit cycle oscillations. The response switches from two-domain to three-domain oscillations and vice-versa in a quasi-periodic fashion because the system is attracted by both solutions. Increasing the airspeed to 12.5 m/s leads to a motion dominated by three-domain oscillations with less frequent occurrences of two-domain oscillations. Then at 12.9 m/s, the two-domain oscillations completely disappear and only three-domain quasi-periodic oscillations are observed up to 13.1 m/s where the system undergoes mono-harmonic limit cycles. Figure 4.7 clearly

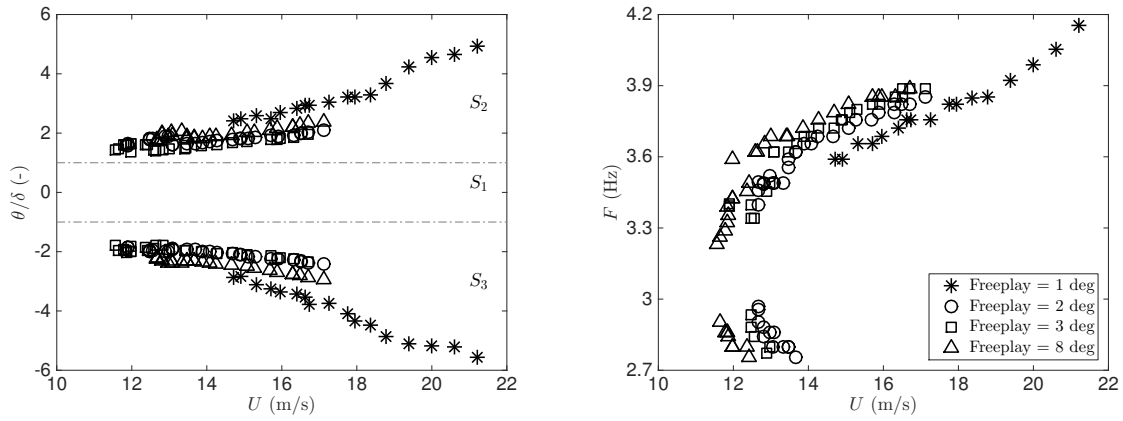

(a) Amplitude (b) Frequency

Figure 4.6: Bifurcation diagram of the system with $\theta_p = 0$

shows that two-domain cycles become less and less frequent as the airspeed is increased until they totally disappear and only three-domain mono-harmonic LCOs are observed.

The bifurcation diagrams of the system with an aerodynamic preload angle θ_p of 5 deg are shown in figure 4.8. Once again, the largest 3 freeplay values lead to similar results while the measurements from the case with the smallest freeplay are slightly different. This time, two-domain LCOs are clearly observed. They appear at around 11m/s and occur continuously, not intermittently as was the case for $\theta_p = 0$ deg. Their amplitude smoothly increases until approximately $U = 12$ m/s, where they are replaced by three-domain LCOs. The frequency diagram is similar to the one obtained without preload, the main LCO branch undergoes a frequency increase with airspeed while another branch, corresponding to the secondary peak of the FFT of quasi-periodic oscillations, features a decreasing frequency variation with airspeed.

Figure 4.9 highlights the transition from two-domain LCOs to three-domain LCOs with a freeplay of 8 deg and a preload angle of 5 deg. At 10.7 m/s, a clear two-domain LCO is observed. Its positive peak amplitude is constant in time while its negative peak amplitude varies unpredictably from cycle to cycle. At 11.4 m/s, two responses can be observed, depending on the initial condition. The first one, plotted in figure 4.9(b), is another two-domain limit cycle with a larger negative amplitude than in the lower-speed case. The second one, depicted in figure 4.9(c), is a quasi-periodic LCO where all the periods span the three domains. Finally, at 11.8 m/s only mono-harmonic three-domain LCOs are observed.

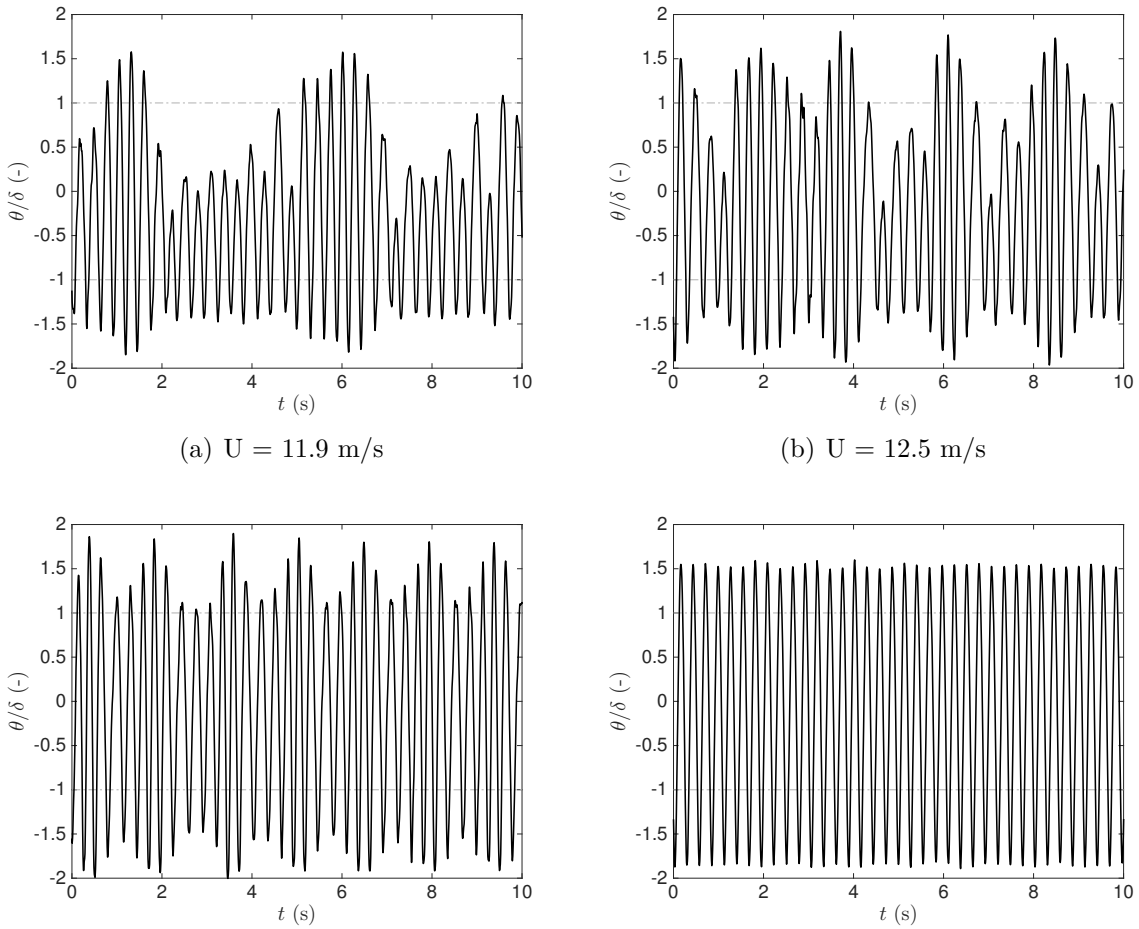

(a) U = 11.9 m/s

(b) U = 12.5 m/s

(c) U = 12.9 m/s

(d) U = 13.1 m/s

Figure 4.7: Pitch time history response of the system with freeplay = 3 deg and $\theta_p = 0$ deg at airspeeds of 11.9, 12.5, 12.9 and 13.1 m/s

Even though no clear two-domain LCOs were observed without aerodynamic preload, the system exhibited a smooth transition from a motion dominated (or influenced) by the two-domain LCOs to a purely three-domain LCOs motion where a single dominant harmonic was observed.

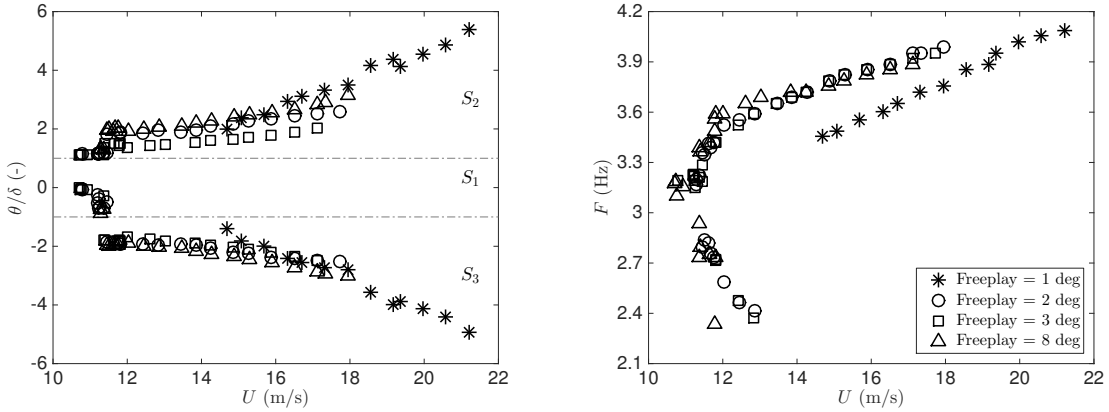

(a) Amplitude (b) Frequency

Figure 4.8: Bifurcation diagram of the system with $\theta_p = 5$ deg

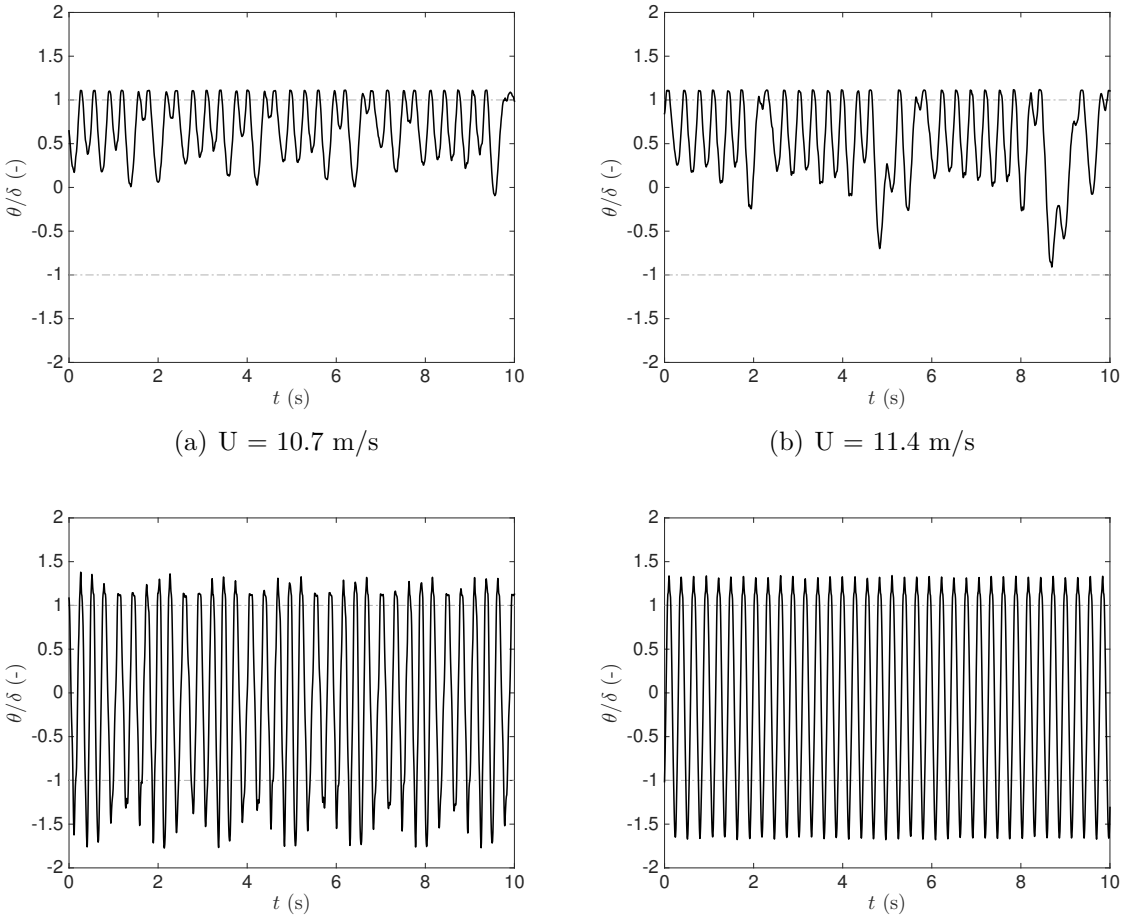

(a) U = 10.7 m/s (b) U = 11.4 m/s

(c) U = 11.4 m/s (d) U = 11.8 m/s

Figure 4.9: Pitch time history response of the system with freeplay = 8 deg and $\theta_p = 5$ deg at airspeeds of 10.7, 11.4, 11.4 and 11.8 m/s

4.5 Mathematical model of the experiment

The primary mathematical model of the experiment was based on equations 4.5. While care was taken to make the experiment as symmetric as possible (aside from the aerodynamic preload), neither the wing nor its placement in the tunnel were perfectly symmetric. In particular, it was impossible to ensure that the wing was perfectly vertical, which means that gravity played a small role in introducing additional asymmetry. The mathematical model of the experiment represented all the sources of asymmetry as a gravity effect due to imperfect verticality. Therefore, a gravity term was added to equation 4.5; for a constant roll angle η, the pitch torque due to gravity is written as

$$T_{grav} = \sin(\eta)\cos(\theta)Sg \approx \sin(\eta)(1 - \frac{\eta^2}{2})S \approx \sin(\eta)Sg \tag{4.7}$$

where $S = (x_{cg} - x_f)m$ is the static imbalance of the wing and g is the acceleration due to gravity. Assuming small pitch angles and neglecting second order terms yields a constant torque that depends on the roll angle of the setup. The constant moment of force is then multiplied by $\mathbf{q}_n$ (see equation 4.3) and added to equation 4.5 to obtain the full equations of motion of the model.

$$\dot{\mathbf{x}} = \begin{cases} \mathbf{Q}_1\mathbf{x} + \mathbf{q}_p\theta_p + \mathbf{q}_n T_{grav} & \text{if} \quad |\theta| \leq \delta \\ \mathbf{Q}_2\mathbf{x} - \mathbf{q}_n K_\theta \operatorname{sgn}(\theta)\delta + \mathbf{q}_p\theta_p + \mathbf{q}_n T_{grav} & \text{if} \quad |\theta| > \delta \end{cases} \tag{4.8}$$

The values of the structural parameters of the equations of motion are those given in appendix D.

4.6 Bifurcation analysis using equivalent linearisation

According to the previous discussion, both two-domain and three-domain limit cycles will be asymmetric for $\theta_p > 0$. In order to apply equivalent linearisation [26, 106] (also known as the describing function or Krylov and Bogoliubov method) we must look for limit cycles of the form

$$\theta(t) = A\sin\omega t + \theta_0 \tag{4.9}$$

where A is the amplitude, ω is the frequency and θ_0 is the centre of the limit cycle. Three types of limit cycle can occur:

- Three-domain cycles, spanning S_1, S_2 and S_3
- Two-domain cycles spanning S_1 and S_2
- Two-domain cycles spanning S_1 and S_3

In all cases, the nonlinear restoring moment of equation 4.1 is approximated as a Fourier series of the form

$$M_\theta(\theta) = a_0 + a_1\cos\omega t + b_1\sin\omega t \tag{4.10}$$

where

$$\begin{aligned} a_0 &= \frac{\omega}{2\pi}\int_{-\pi/\omega}^{\pi/\omega} M(A\sin\omega t + \theta_0)\mathrm{d}t \\ a_1 &= \frac{\omega}{\pi}\int_{-\pi/\omega}^{\pi/\omega} M(A\sin\omega t + \theta_0)\cos\omega t\mathrm{d}t \\ b_1 &= \frac{\omega}{\pi}\int_{-\pi/\omega}^{\pi/\omega} M(A\sin\omega t + \theta_0)\sin\omega t\mathrm{d}t \end{aligned} \tag{4.11}$$

For a three-domain cycle, A must be large enough that $\theta(t)$ spans all three domains. Figure 4.10 plots the pitch variation in time and the corresponding freeplay load for the case $\theta_0 = 0.3$, $\delta = 0.5$, $A = 1$ and $\omega = 1$. The integrals of equation 4.11 must be carried out in the intervals $[-\pi, t_1]$, $[t_1, t_2]$, $[t_2, t_3]$, $[t_3, t_4]$ and $[t_4, \pi]$. These time instances are given by $t_1 = -\pi + \sin^{-1}(\delta + \theta_0)/A$, $t_2 = -\sin^{-1}(\delta + \theta_0)/A$, $t_3 = \sin^{-1}(\delta - \theta_0)/A$, $t_4 = \pi - \sin^{-1}(\delta - \theta_0)/A$.

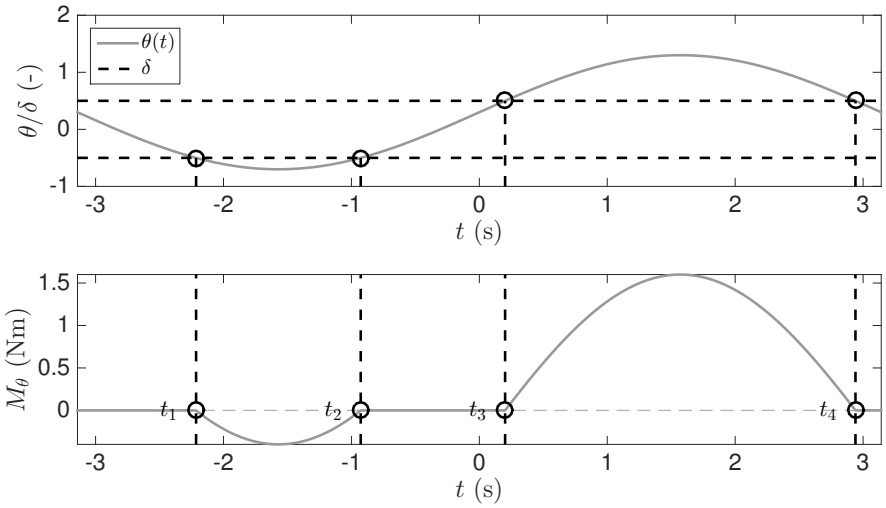

Figure 4.10: Sinusoidal displacement (top) and corresponding freeplay load (bottom), three-domain cycle case

As an example, after defining

$$\sigma_1 = \sin^{-1}\left(\frac{\delta - \theta_0}{A}\right) \tag{4.12}$$

$$\sigma_2 = \sin^{-1}\left(\frac{\delta + \theta_0}{A}\right) \tag{4.13}$$

the equation for b_1 becomes

$$b_1 = \frac{1}{\pi}\int_{-\pi+\sigma_2}^{-\sigma_2} K_\theta(A\sin t + \delta)\sin t\mathrm{d}t + \frac{1}{\pi}\int_{\sigma_1}^{\pi-\sigma_1} K_\theta(A\sin t - \delta)\sin t\mathrm{d}t \tag{4.14}$$

After working out the integrals and repeating for a_0 and a_1, equations 4.11 become

$$\begin{aligned} a_0 &= \frac{K_\theta}{\pi}(\pi\theta_0 - \theta_0(\sigma_1+\sigma_2) + \delta(\sigma_1-\sigma_2) + A(\cos\sigma_1 - \cos\sigma_2)) \\ a_1 &= 0 \\ b_1 &= \frac{AK_\theta}{2\pi}(2\pi - (\sin 2\sigma_1 + \sin 2\sigma_2) - 2(\sigma_1+\sigma_2)) \end{aligned} \tag{4.15}$$

Looking back at equation 4.9, it can be re-arranged as

$$\sin\omega t = \frac{\theta - \theta_0}{A} \tag{4.16}$$

so that, after setting $a_1 = 0$, equation 4.10 becomes

$$M_\theta(\theta) = a_0 + b_1 \frac{\theta - \theta_0}{A} = a_0 - \frac{b_1 \theta_0}{A} + \frac{b_1}{A}\theta \tag{4.17}$$

In this expression, there is a constant term and a term proportional to θ, i.e. a linear stiffness term. An equivalent linear stiffness can be defined as $K_{eq} = b_1/A$, or

$$K_{eq} = \frac{K_\theta}{2\pi} \left(2\pi - (\sin 2\sigma_1 + \sin 2\sigma_2) - 2(\sigma_1 + \sigma_2)\right) \tag{4.18}$$

Replacing the nonlinear function in equations 4.5 by the equivalent linear function of equation 4.10, the complete equivalent linear system for three-domain cycles is obtained as

$$\dot{\mathbf{x}} = \mathbf{Q}_{eq}\mathbf{x} + \mathbf{q}_n \left(a_0 - K_{eq}\theta_0\right) + \mathbf{q}_p \theta_p \tag{4.19}$$

for different values of A and θ_0, where $\mathbf{Q}_{eq}\mathbf{x} = \mathbf{Q}_1\mathbf{x} + \mathbf{q}_n K_{eq}(A, \theta_0)\theta$. Note that the fixed point of the equivalent linearised system is given by

$$\mathbf{x}_{eq} = -\mathbf{Q}_{eq}^{-1} \left(\mathbf{q}_n \left(a_0 - K_{eq}\theta_0\right) + \mathbf{q}_p \theta_p\right) \tag{4.20}$$

The equivalent linearised system can only exist if both σ_1 and σ_2 are real. This means that

$$\begin{aligned} |\delta - \theta_0| &\leq A \\ |\delta + \theta_0| &\leq A \end{aligned} \tag{4.21}$$

simultaneously. If θ_p is not equal to zero then θ_0 is also not equal to zero and is it not possible to obtain a symmetric response. Under these circumstances, three-domain limit cycles with amplitude $A = \delta$ cannot exist because they would violate one of the conditions of existence.

The case $K_{eq} = 0$ reflects the bifurcation condition for the symmetric system, i.e. $\theta_p = 0$. A limit cycle with the lowest possible amplitude $A = \delta$ appears at U_{F_1}, the flutter speed of the underlying linear system. However, for an asymmetric system this limit cycle cannot occur, as explained earlier. Therefore, $K_{eq} = 0$ is not the bifurcation condition for asymmetric systems and limit cycles will start appearing at airspeeds higher than U_{F_1}.

The equivalent linearisation problem consists in determining the values of A and θ_0 that result in periodic solutions at each airspeed value of interest. The solution process is identical to the one developed in [26]. First, the flutter speed of the equivalent lin-

earized system, $U_{F_{eq}}(K_{eq})$, is calculated for all values of K_{eq} from 0 to K_θ. Then, for each $U_{F_{eq}}(K_{eq})$, we calculate the values of A and θ_0 that give the correct value of the equivalent linearised stiffness when substituted into equation 4.18 and for which θ_0 is equal to the pitch component of the fixed point of the equivalent linearised system. The nonlinear algebraic system

$$\begin{aligned} K_{eq} - \frac{K_\theta}{2\pi}\left(2\pi - (\sin 2\sigma_1 + \sin 2\sigma_2) - 2(\sigma_1 + \sigma_2)\right) &= 0 \\ \theta_{F_{eq}} - \theta_0 &= 0 \end{aligned} \tag{4.22}$$

can be set up and solved using Newton iterations, where $\theta_{F_{eq}}$ is the pitch component of $\mathbf{x}_{eq}$ from equation 4.20. The starting point of the limit cycle branch is $K_{eq} = 0$, $U = U_{F_1}$. Initial guesses are chosen as $A = \delta$ and $\theta_0 = 0$.

Once a converged limit cycle is obtained, its stability can be investigated by evaluating a new equivalent linearized system at the same airspeed but with slightly higher amplitude, i.e. $A + \delta A$, where $\delta A << 1$. We calculate the new value of θ_0 that corresponds to this amplitude and the resulting K_{eq}. Finally, we set up the new equivalent linearised system using equations 4.19. If all of its eigenvalues have negative real part, then the limit cycle at A is stable. If any of the eigenvalues have a positive real part then the limit cycle is unstable.

Two-domain limit cycles can be approximated using the same equivalent linearisation scheme. The only difference lies in the values of K_{eq} and θ_0, which are different for two-domain cycles. Applying the Fourier series procedure to two-domain cycles gives the following expressions for a_0, a_1 and b_1 [26]

$$\begin{aligned} a_0 &= \frac{K_2\theta_0}{2} - \frac{K_2\delta}{2} + \frac{AK_2}{\pi}\left(\sigma_1 \sin\sigma_1 + \cos\sigma_1\right) \\ a_1 &= 0 \\ b_1 &= A\frac{K_2}{2} - A\frac{K_2}{2\pi}\left(2\sigma_1 + \sin 2\sigma_1\right) \end{aligned} \tag{4.23}$$

so that K_{eq} becomes

$$K_{eq} = \frac{K_2}{2} - \frac{K_2}{2\pi}\left(2\sigma_1 + \sin 2\sigma_1\right) \tag{4.24}$$

Two-domain limit cycles can exist as long as $|\delta - \theta_0| \leq A$, i.e. σ_1 is real. Furthermore, they must only span two domains so that,

$$\begin{aligned} \text{if} \quad \theta_0 + A \geq \delta \quad \text{then} \qquad \theta_0 - A \geq -\delta \\ \text{if} \quad \theta_0 - A \leq -\delta \quad \text{then} \qquad \theta_0 + A \leq \delta \end{aligned} \tag{4.25}$$

This means that neither the upper nor the lower bound of the cycle can cross a freeplay boundary. For example, a two-domain cycle spanning S_1 and S_2 will disappear if either of the two bounds crosses $+\delta$. Note that σ_1 takes values between $-\pi/2 \leq \sigma_1 \leq \pi/2$, while $\delta - \theta_0$ spans $-A \leq \delta - \theta_0 \leq A$.

For the right limit $\sigma_1 = \pi/2$, $\delta - \theta_0 = A$, substituting into equations 4.23 and 4.24 yields

$$a_0 = 0, \quad K_{eq} = 0, \tag{4.26}$$

while for the left limit $\sigma_1 = -\pi/2$, $\delta - \theta_0 = -A$ we obtain

$$a_0 = K_\theta(\theta_0 + \delta), \quad K_{eq} = K_\theta \tag{4.27}$$

In other words, two-domain limit cycles appear when the equivalent stiffness is equal to the stiffness of the underlying linear system and disappear when K_{eq} is equal to the stiffness of the overlying linear system. Again, these conclusions are only true if $\theta_p = 0$; in the presence of aerodynamic preload the $K_{eq} = 0$ and $K_{eq} = K_\theta$ appearance and disappearance bounds are modified.

4.7 Numerical model validation

4.7.1 Pre-critical response

Figure 4.11 plots the variation of the natural frequencies and damping ratios of the overlying linear system with airspeed. Modal estimates from the wind tunnel tests are compared to the predictions of the three models. Clearly the predictions of the models are in good agreement with each other and with the experimental measurements.

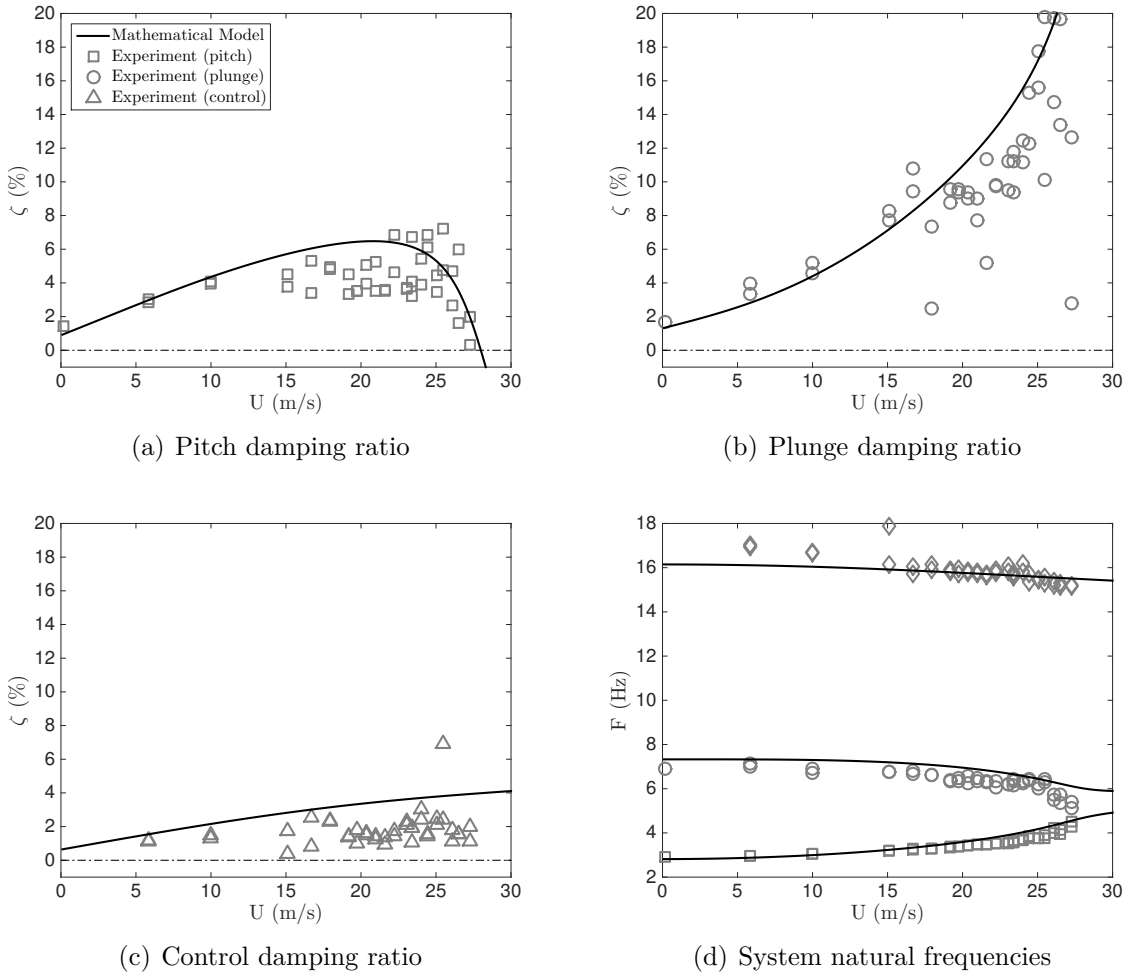

(a) Pitch damping ratio

(b) Plunge damping ratio

(c) Control damping ratio

(d) System natural frequencies

Figure 4.11: Flutter plots for overlying linear system. The legend in subfigure 1 applies to all 4 subfigures.

4.7.2 Post-critical response

A comparison of the theoretical and experimental limit cycle amplitude variation with airspeed for $\theta_p = 0$ is plotted in figure 4.12. For all the freeplay gaps considered, the

mathematical model predicts two-domain LCOs, which were not observed in practice. In contrast, the amplitudes of the three-domain cycles are predicted with satisfactory accuracy. In all four cases, the predicted two-domain limit cycle branch lies in the airspeed range where quasi-periodic motion was observed in the experiment. That is consistent with the fact that the quasi-periodicity is due to the co-existence of nearby limit cycles at the same airspeed. In all four cases, the model predicts limit cycles at airspeeds lower than the experimental LCO onset speed. Again, it is believed that this disparity is due to the nonlinear damping present in the bearings of the experimental system, which suppressed small amplitude oscillations.

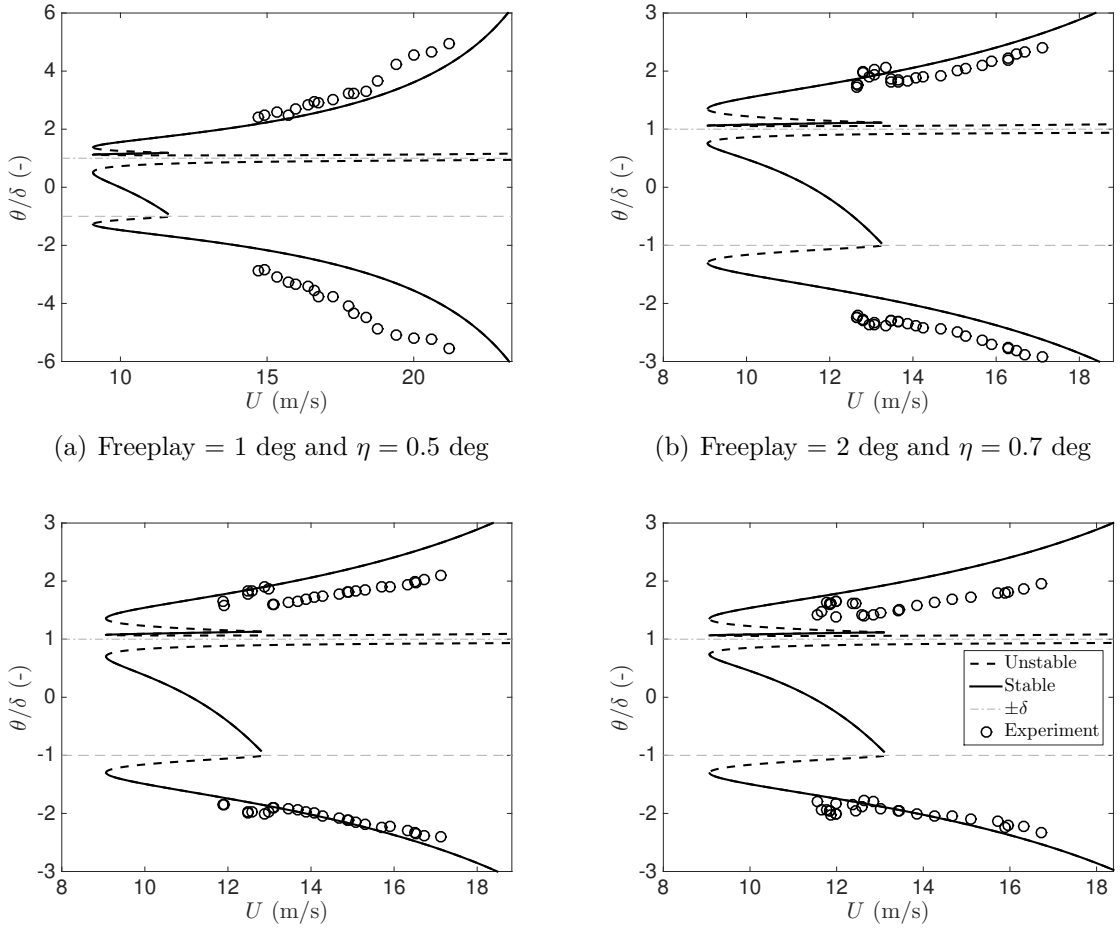

(a) Freeplay = 1 deg and $\eta = 0.5$ deg

(b) Freeplay = 2 deg and $\eta = 0.7$ deg

(c) Freeplay = 3 deg and $\eta = 1.5$ deg

(d) Freeplay = 8 deg and $\eta = 3$ deg

Figure 4.12: Pitch amplitude bifurcation diagram of the system with a preload angle of 0 deg

The frequency bifurcation diagram for the system with $\theta_p = 0$ is depicted in figure 4.13. The model accurately predicts the three-domain limit cycle frequency for all the freeplay

values. However, the predicted two-domain frequencies (i.e. the part of the branch below 3 Hz) are slightly lower than those observed experimentally.

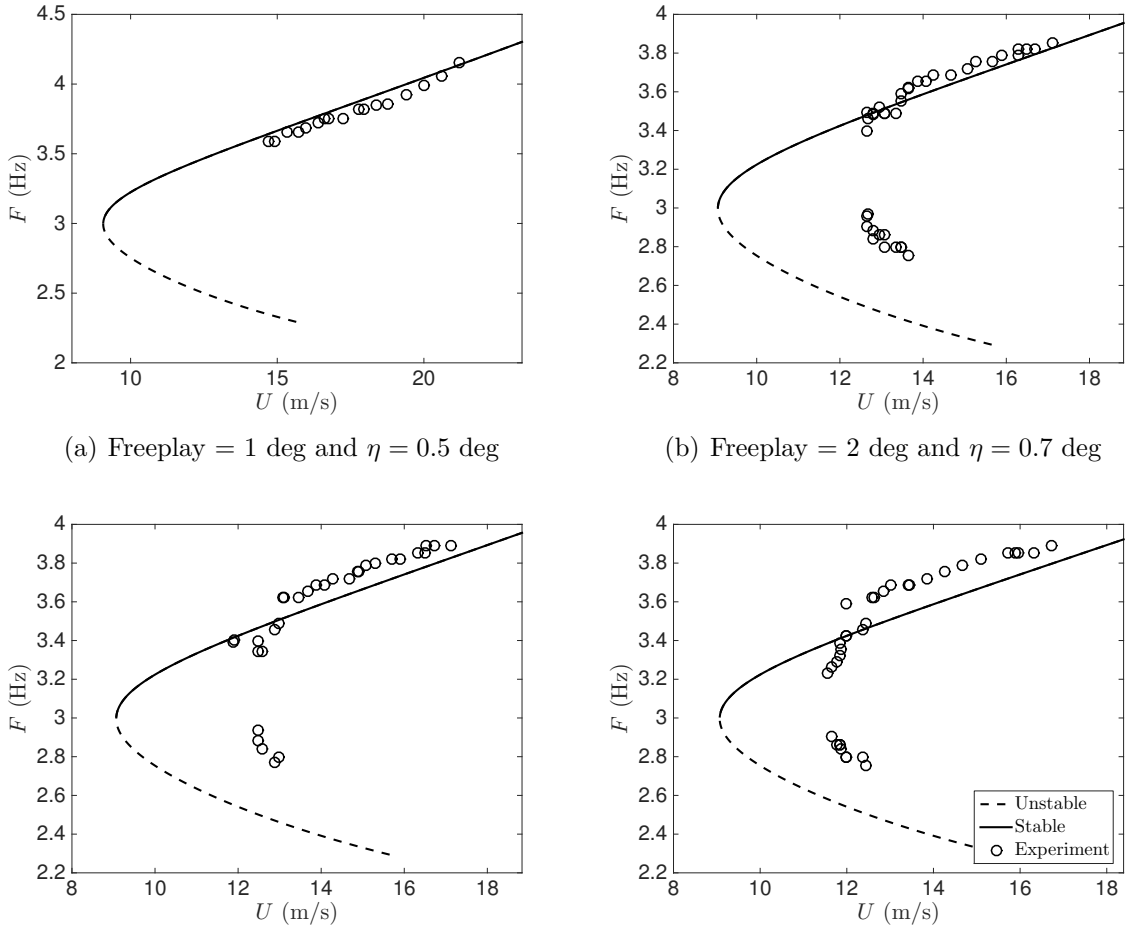

(a) Freeplay = 1 deg and $\eta = 0.5$ deg

(b) Freeplay = 2 deg and $\eta = 0.7$ deg

(c) Freeplay = 3 deg and $\eta = 1.5$ deg

(d) Freeplay = 8 deg and $\eta = 3$ deg

Figure 4.13: Frequency bifurcation diagram of the system with a preload angle of 0 deg

Figure 4.14 displays the experimental and mathematical pitch amplitude bifurcation diagrams of the system with an aerodynamic preload angle of 5 deg. The model estimates well both the two-domain and the three-domain LCO amplitudes for freeplay gaps of 2 and 3 deg, slightly underestimates the amplitude when the freeplay gap is 1 degree and slightly overestimates the top branch for 8 degrees of freeplay gap. In all four cases, the model predicts limit cycles at airspeeds lower than those observed in the experiment. These small amplitude vibrations are once again damped by the nonlinear friction in the bearings. This is especially noticeable in the 1 deg freeplay cases because the gap is so small that all LCOs have low amplitude. It is important to note that, for freeplay gaps of 2, 3 and 8 deg, the model predicts with satisfactory accuracy the amplitudes of both

the two-domain and three-domain limit cycles.

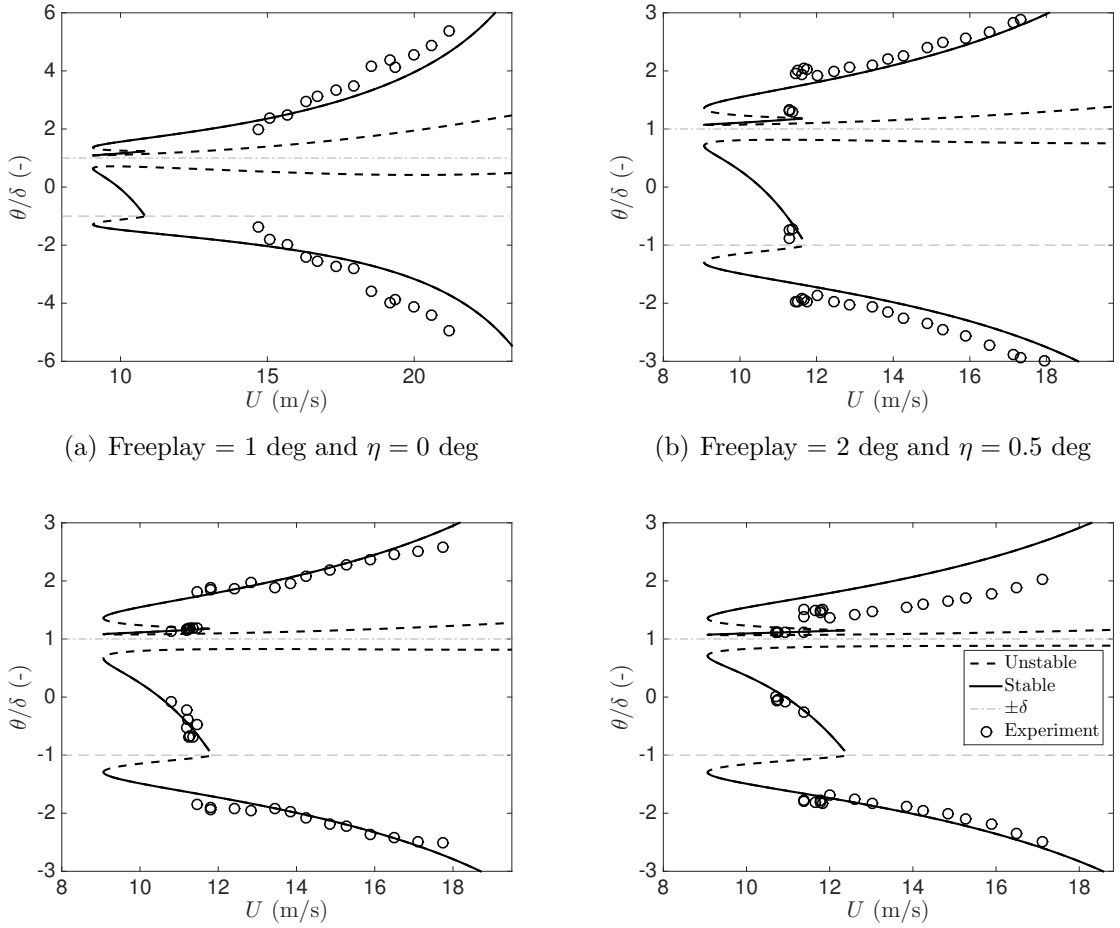

(a) Freeplay = 1 deg and $\eta = 0$ deg

(b) Freeplay = 2 deg and $\eta = 0.5$ deg

(c) Freeplay = 3 deg and $\eta = 1.25$ deg

(d) Freeplay = 8 deg and $\eta = 3$ deg

Figure 4.14: Pitch amplitude bifurcation diagram of the system with a preload angle of 5 degrees

The observed and predicted frequency variations with airspeed for $\theta_p = 5$ deg are compared in figure 4.15. In this case, the frequencies of both the two-domain and three-domain limit cycles are predicted with satisfactory accuracy, although the lowest airspeed at which LCOs can occur is still under-predicted.

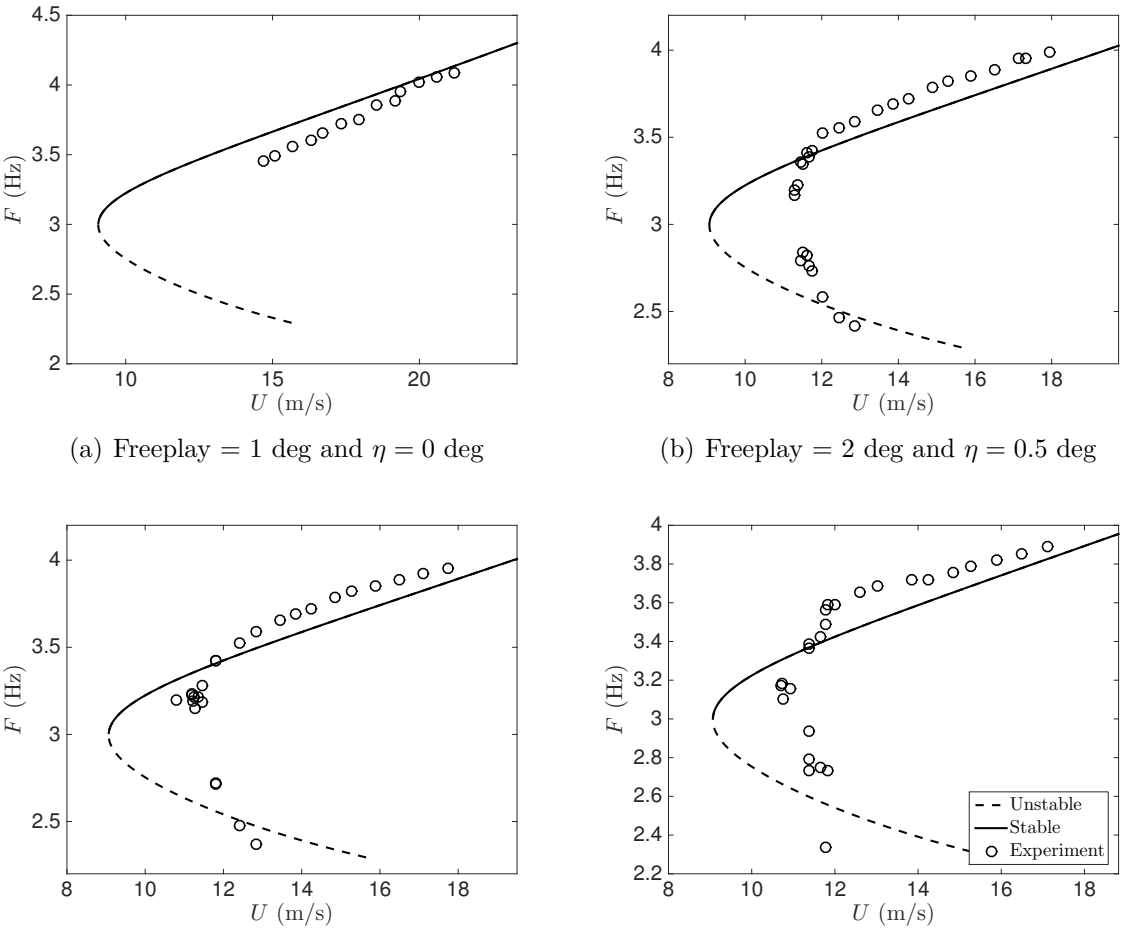

(a) Freeplay = 1 deg and $\eta = 0$ deg

(b) Freeplay = 2 deg and $\eta = 0.5$ deg

(c) Freeplay = 3 deg and $\eta = 1.25$ deg

(d) Freeplay = 8 deg and $\eta = 3$ deg

Figure 4.15: Frequency bifurcation diagram of the system with a preload angle of 5 degrees

4.8 Chapter summary

In this chapter, a typical aeroelastic section with degrees of freedom in pitch, plunge and control surface deflections and with freeplay in pitch is studied in the wind tunnel. Then a mathematical model is proposed and its predictions are compared to the experimental observations.

The experimental results showed that this system undergoes limit cycle oscillations from airspeeds as low as 9 m/s while the flutter speed of the system without freeplay is approximately 28 m/s. The freeplay nonlinearity splits the phase space into three linear sub-regions and, depending on the airspeed, LCOs that span two or three of these sub-regions could be observed. As expected, varying the size of the freeplay gap did not lead to any significant change in the observed phenomena provided the gap was sufficiently large to overcome the nonlinear damping regime in the bearings. Conversely, considering aerodynamic preload angles of 0 and 5 degrees allowed the identification of two different regimes: without preload, no stable 2-domain limit cycle oscillation was observed however the two-domain LCO branch clearly affected the response which was aperiodic and attracted by both two-domain and three-domain cycles. With 5 degrees of preload, on the other hand, small amplitude 2-domain LCOs were observed and smoothly transitioned to 3-domain LCOs as the airspeed was increased.

A simple numerical model based on Wagner aerodynamics and solved using equivalent linearisation was used to accurately predict the existence, the amplitude and the frequency of both the three-domain limit cycles and the two-domain limit cycles for all the freeplay gaps and the aerodynamic preload angles considered.

Chapter 5

LCO suppression on a pitch-plunge-control wing

5.1 Introduction

The aim of this penultimate chapter is the investigation of the effects of linear and nonlinear absorbers on the pitch-plunge-control wing with freeplay in the pitch DOF that was studied in chapter 4. One of the major differences between this system and the NLPFW is that the freeplay nonlinearity leads to LCOs at airspeeds much smaller (approximately 33%) than the system's linear flutter speed. As a result, it is not unlikely for such LCOs to occur inside an aircraft's flight envelope which can reach up to 85% of the aircraft's linear flutter speed [7] (80% for civil aircraft [6]).

Linear absorbers are first considered. LTVAs tuned on the underlying linear system (no stiffness), the overlying linear system (full stiffness) and full nonlinear system are considered and compared. A focus is made on the linear flutter speed of the system and on the LCO amplitude and onset speed.

Then, NLTVAs based on the LTVA tuned on the full nonlinear system are investigated. Cubic and freeplay nonlinearities are considered. The latter was chosen because is was already investigated on the absorber of the NLPFW (chapter 3) and because it would be convenient to build for a practical implementation while the latter was chosen to respect the principle of similarity [114], which states that, in forced vibrations problems, the nonlinearity in the absorber should mimic the nonlinearity in the primary system.

5.2 Mathematical model

Depicted in figure 5.1, the system considered is based on the wing with pitch, plunge and control surface deflection DOFs and with freeplay in the pitch DOF studied in chapter 4. This time, a mechanical absorber of mass m_a is attached to the primary system at a distance x_a from the flexural axis by means of a dashpot of damping c_a, a linear spring of stiffness k_a and a nonlinear spring that provides a nonlinear restoring force F_{nl}. Cubic hardening and freeplay springs are considered in this study. The absorber can be tuned by adjusting the stiffness and the damping of the sub-system while the absorber mass and position are set to 4% of the total mass, m, and $0.25 \times c$, respectively. This absorber's displacement is described by means of an additional DOF ξ.

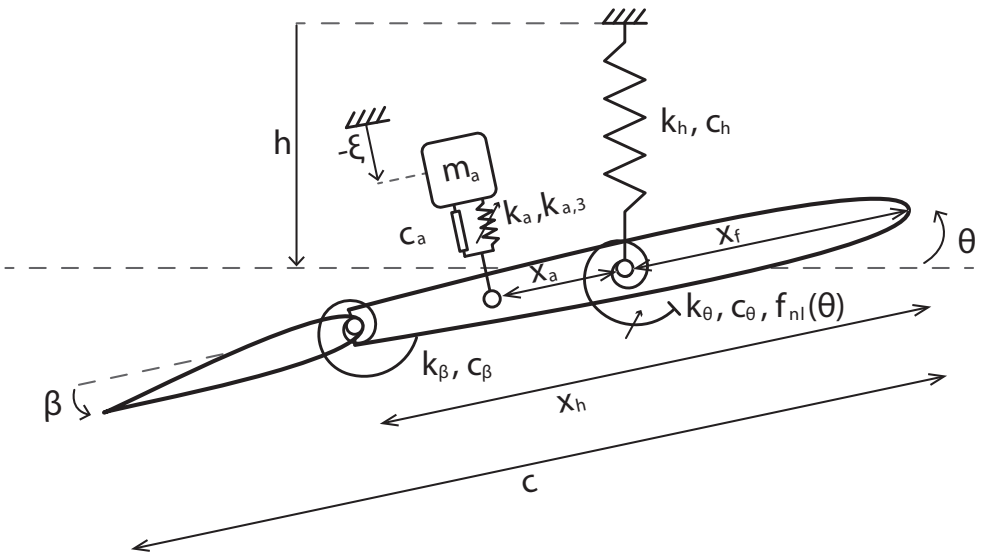

Figure 5.1: Aeroelastic system with freeplay in pitch and an absorber attached

The absorber's natural frequency is given by

$$f_{ltva} = \frac{1}{2\pi}\sqrt{\frac{k_a}{m_a}}$$

while its damping is written as

$$\zeta_{ltva} = \frac{c_a}{2\sqrt{m_a k_a}}$$

Assuming the absorber is isolated from the airflow, the equations of motion of the system flying with airspeed U in air of density ρ are almost identical to equation 4.8 where the

roll angle and aerodynamic preload are neglected for simplicity. The freeplay gap is set to $\delta = 5$ deg. The structural displacements are denoted by the vector $\mathbf{y} = [h \quad \theta \quad \beta \quad \xi]$ while the six aerodynamic states are denoted by the vector $\mathbf{w} = [w_1 \quad \dots \quad w_6]$. Then the complete state vector of the system is given by $\mathbf{x} = [\dot{\mathbf{y}} \quad \mathbf{y} \quad \mathbf{w}]^T$ and has dimensions 14×1. The equations of motion of the system coupled with an absorber and with freeplay in the pitch DOF are given by

$$\dot{\mathbf{x}} = \mathbf{Q}_1 \mathbf{x} + \mathbf{q}_\theta M_\theta(\theta) + \mathbf{q}_{nl} F_{nl}(\Delta\xi, k_a, c_{nl}) \tag{5.1}$$

where

$$\begin{aligned}
\mathbf{Q}_1 &= \begin{pmatrix} -\mathbf{M}^{-1}\left(\mathbf{C} + \mathbf{C}_{ltva} + \rho U \mathbf{D}\right) & -\mathbf{M}^{-1}\left(\mathbf{E}_1 + \mathbf{E}_{ltva} + \rho U^2 \mathbf{F}\right) & -\rho U^3 \mathbf{M}^{-1}\mathbf{W} \\ \mathbf{I}_{4\times4} & \mathbf{0}_{4\times4} & \mathbf{0}_{4\times6} \\ \mathbf{0}_{6\times4} & \mathbf{W}_1 & U\mathbf{W}_2 \end{pmatrix} \\
\mathbf{q}_\theta &= \begin{pmatrix} -\mathbf{M}^{-1}\begin{pmatrix} 0 \\ 1 \\ 0 \\ 0 \end{pmatrix} \\ \mathbf{0}_{10\times1} \end{pmatrix} \\
\mathbf{q}_{nl} &= \begin{pmatrix} -\mathbf{M}^{-1}\begin{pmatrix} -1 \\ -x_a \\ 0 \\ 1 \end{pmatrix} \\ \mathbf{0}_{10\times1} \end{pmatrix} \qquad (5.2) \\
\mathbf{M} &= \mathbf{A} + \mathbf{A}_{ltva} + \rho\mathbf{B} \qquad (5.3) \\
\Delta\xi &= \theta x_a + h - \xi \qquad (5.4)
\end{aligned}$$

and $\mathbf{E}_1$, is the value of the structural stiffness matrix inside the freeplay region $\pm\delta$, given by

$$\mathbf{E}_1 = \begin{pmatrix} K_h & 0 & 0 & 0 \\ 0 & 0 & 0 & 0 \\ 0 & 0 & K_\beta & 0 \\ 0 & 0 & 0 & 0 \end{pmatrix} \tag{5.5}$$

Matrices $\mathbf{A}$, $\mathbf{A}_{ltva}$ and $\mathbf{B}$ are the structural, absorber and aerodynamic mass matrices, respectively. $\mathbf{C}$, $\mathbf{C}_{ltva}$, $\rho U\mathbf{D}$ are the structural, absorber and aerodynamic damping matrices, respectively. $\mathbf{E}_{ltva}$ and $\rho U^2\mathbf{F}$ are the absorber and aerodynamic stiffness matrices,

respectively. $\mathbf{W}$ is the aerodynamic state matrix, $\mathbf{W}_1$ and $\mathbf{W}_2$ are the aerodynamic state equation matrices, M_θ is the freeplay restoring torque described in equation 4.1 and F_{nl} is the nonlinear absorber restoring force. The notation $\mathbf{I}_{4\times4}$ denotes a unit matrix of size 4×4. The values of all the matrices are given in appendix D.

Equation 5.1 can be written as

$$\dot{\mathbf{x}} = \begin{cases} \mathbf{Q}_1\mathbf{x} + \mathbf{q}_{nl}F_{nl}(\Delta\xi, k_a, c_{nl}) & \text{if} \quad |\theta| \leq \delta \qquad \text{(a)} \\ \mathbf{Q}_2\mathbf{x} - \mathbf{q}_\theta K_\theta \operatorname{sgn}(\theta)\delta + \mathbf{q}_{nl}F_{nl}(\Delta\xi, k_a, c_{nl}) & \text{if} \quad |\theta| > \delta \qquad \text{(b)} \end{cases} \tag{5.6}$$

where $\mathbf{Q}_2\mathbf{x} = \mathbf{Q}_1\mathbf{x} + \mathbf{q}_\theta K_\theta \theta$.

Again, two sub-systems relevant to freeplay are defined:

- Underlying linear system: the system without structural stiffness that is only valid inside the freeplay region (equation 5.6(a)).
- Overlying linear system: the nominal system without freeplay and with full stiffness (equation 5.6(b) with $\delta = 0$).

5.3 Response without absorber

Figure 5.2 depicts the bifurcation diagram of the system without absorber computed using a shooting algorithm [26]. Subfigures 5.2(a) & 5.2(c) plot the pitch amplitude variation with airspeed and a close-up in the vicinity of the LCO onset speed of the system (lowest airspeed where LCOs can be observed), respectively. Subfigures 5.2(b) & 5.2(d) display the variation of the LCO frequency and a close-up in the vicinity of the LCO onset speed of the system, respectively. Finally, subfigures 5.2(e) & 5.2(f) correspond to the plunge amplitude and control surface deflection amplitude variation with airspeed. As all the LCOs are symmetric, subfigures 5.2(c) to 5.2(f) only depict the positive amplitude. Note that in systems with freeplay, the LCO amplitude depends linearly on the freeplay gap so all the amplitudes are divided by δ.

A symmetric unstable LCO branch arises at $U_{F,0} = 15.67$ m/s, the flutter speed of the underlying system, because of a grazing bifurcation. The continuation code does not reach the grazing point because this unstable branch is very difficult to track close to the freeplay boundary. The unstable branch propagates in the decreasing airspeed direction until $U_{\mathrm{LCO}} = 9.16$ m/s where it folds back and becomes stable. Then, the pitch and control LCO amplitude and the LCO frequency increase rapidly with airspeed while the plunge LCO amplitude decreases then increases until 10.01 m/s where quasi-periodic solutions are observed because of a Neimark-Sacker bifurcation. At airspeeds higher than 11.05 m/s, only stable LCOs are observed, whose amplitude increases smoothly with airspeed and becomes asymptotically infinite at $U_{F,1} = 27.99$ m/s, the flutter speed of the overlying linear system. Military aircraft flight envelopes can reach up to 85% of the plane's linear flutter speed [7] so should freeplay suddenly occur, it is not unlikely to be at an airspeed close to $U_{F,1}$, i.e. where the LCO amplitude is large. Two-domain small amplitude LCOs can also be observed close to either boundary of the freeplay region however they do not occur at airspeeds smaller than the large amplitude LCOs studied here and they are less critical because of their small amplitude. Such LCOs are studied in detail in chapter 4.

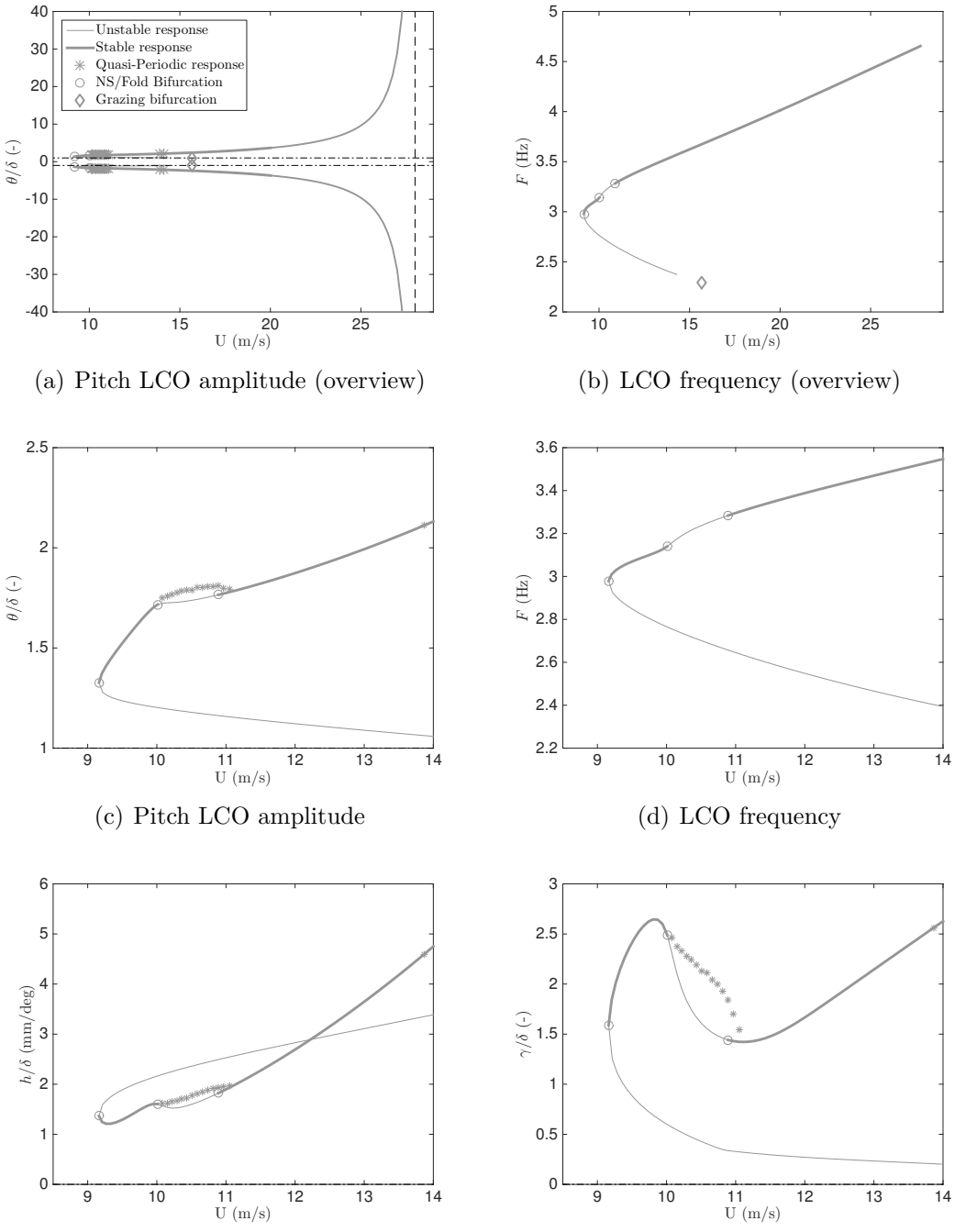

(a) Pitch LCO amplitude (overview)

(b) LCO frequency (overview)

(c) Pitch LCO amplitude

(d) LCO frequency

(e) Plunge LCO amplitude

(f) Control LCO amplitude

Figure 5.2: Bifurcation diagram of the system without absorber

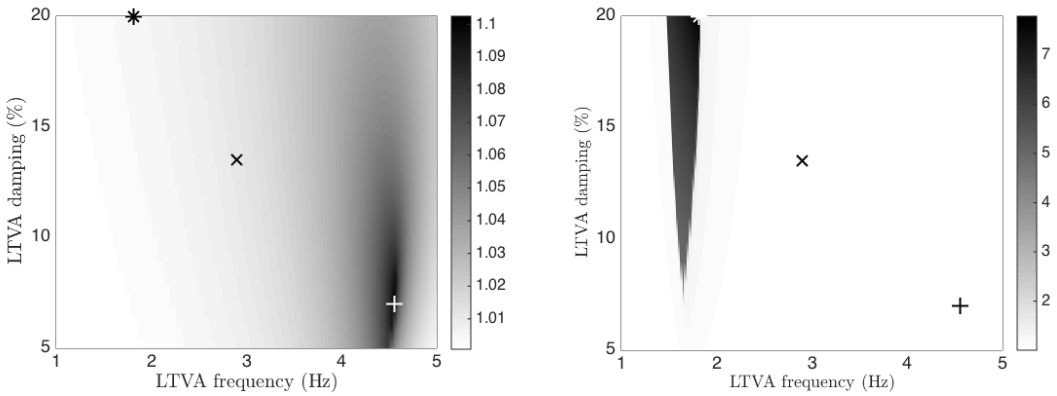

(a) Overlying linear system relative flutter speed (b) Underlying linear system relative flutter speed

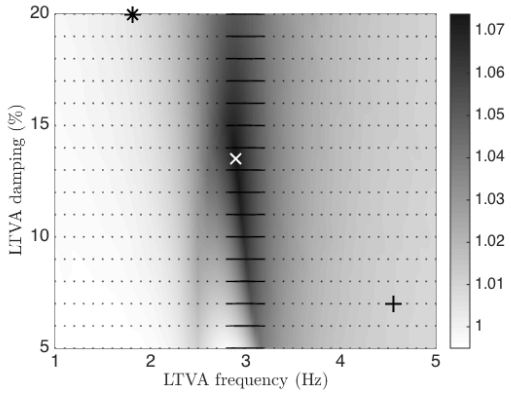

(c) Relative LCO onset speed

Figure 5.3: Critical airspeeds of the system depending on the absorber tuning. The LTVA is attached in $x_a = 0.25 \times c$.

5.4 Linear tuned vibration absorbers investigation

5.4.1 Critical airspeed optimisation

As demonstrated in the previous section, the system without absorber features three critical velocities that one can try to optimise by means of a LTVA. The flutter speed of the underlying linear system, $U_{F,0}$, is the airspeed at which the unstable LCO branch arises because of the grazing bifurcation. The flutter speed of the overlying linear system, $U_{F,1}$, is the flutter speed of the system without freeplay, i.e. in normal operational conditions. Finally, the LCO onset speed, U_{LCO} is the lowest airspeed at which limit cycles can be observed on the system with freeplay. For linear absorbers ($F_{nl} = 0$), the first two airspeeds are linear flutter speeds and can therefore be computed using simple stability analysis while the LCO onset speed is computed from continuation curves similar to those of figure 5.2 for many absorber configurations.

Figures 5.3(a-c) plot the relative flutter speed of the overlying linear system, the relative flutter speed of the underlying linear system and the relative LCO onset speed, respectively, as a function of the LTVA frequency and modal damping. Each relative airspeed is defined as the ratio of the critical airspeed of the system with absorber to the same critical airspeed of the system without absorber and therefore provides information on the beneficial effect of the absorbers. Each dot of subfigure 5.4(b) corresponds to one continuation curve while the mesh is not displayed in figures 5.3(a) and 5.3(b) because it is much finer.

Comparing the three figures shows that a single absorber cannot be tuned to increase all three airspeeds at the same time so three different absorbers are considered; their characteristics and performance are given in table 5.1. In the tuning region considered, no absorber leads to a decrease in any critical airspeed and a high sensitivity in absorber frequency is observed close to each optimal tuning.

Absorber 1 (+) is optimised for the overlying linear system. It increases the flutter speed of the overlying system by 10%, the grazing airspeed by 6.4% and does not have significant effect on the LCO onset speed.

Absorber 2 (∗) is tuned on the underlying linear system. It increases the grazing airspeed by approximately 673% but has a negligible effect on the LCO onset speed and on the linear flutter speed of the system without freeplay. This suggests that the LCO onset speed is not related to the flutter speed of the underlying linear system.

-	No LTVA	LTVA 1	LTVA 2	LTVA 3
symbol		+	*	×
F_{ltva} [Hz]	-	4.56	1.81	2.90
ε_{ltva} [%]	-	7	20	13.5
$U_{F,0}$ [m/s]	15.67	16.68 (+6.4%)	121.24 (+673%)	16.20 (+3.4%)
$U_{F,1}$ [m/s]	27.99	30.86 (+10%)	28.12 (+0.5%)	28.3 (+1.1%)
U_{LCO} [m/s]	9.16	9.31 (+1.6%)	9.26 (+0.99%)	9.87 (+7.7%)

Table 5.1: Optimal absorber tunings and performance

Absorber 3 (×) is designed for the full nonlinear system. It increases the LCO onset speed by 7.7% and does not have a significant effect on the overlying and underlying flutter speeds.

The relatively poor performance of the LTVA (about one third of that achieved on the NLPFW) is probably due to the fact that the absorber is located close to the primary system's center of mass. Figure 5.4 depicts the relative increase in overlying linear system flutter speed and LCO onset speed as a function of the LTVA natural frequency and damping ratio for an absorber located at the wing's leading edge at $x_a = -0.25 \times c$ rather than in the middle of the wing. In this case, a LTVA with a frequency of 7 Hz and a damping ratio of 15% increases the linear flutter speed of the overlying linear system by 30.3% however it leads to a decrease in LCO onset speed of 2.0%. Conversely, a LTVA with a natural frequency of 2.65 Hz and a damping ratio of 6.5% leads to a increase in LCO onset speed of 13.9% but to a decrease in flutter speed of 5.5%. Only the initial absorber position ($x_a = 0.25 \times c$) has been investigated in the rest of this work.

5.4.2 Bifurcation analysis

Figure 5.5 compares the bifurcation diagram of the system without absorber (grey) to those of absorbers 1, 2 and 3. Subfigures 5.5(a) to 5.5(d) correspond to the pitch LCO amplitude, plunge LCO amplitude, control surface deflection LCO amplitude and LCO frequency, respectively, in the neighbourhood of the LCO onset speed.

Absorber 1 (black) increases the LCO onset speed to 9.31 m/s (+1.6%), reduces the pitch LCO amplitude between airspeeds 9.31 m/s and 10.76 m/s but has a detrimental effect on the response from 10.76 m/s to 13.01 m/s even though it suppresses the Neimark-Sacker bifurcation. At higher airspeeds, a reduction in LCO amplitude is observed and the airspeed of the vertical asymptote is increased to 30.86 m/s (+10%), the flutter speed

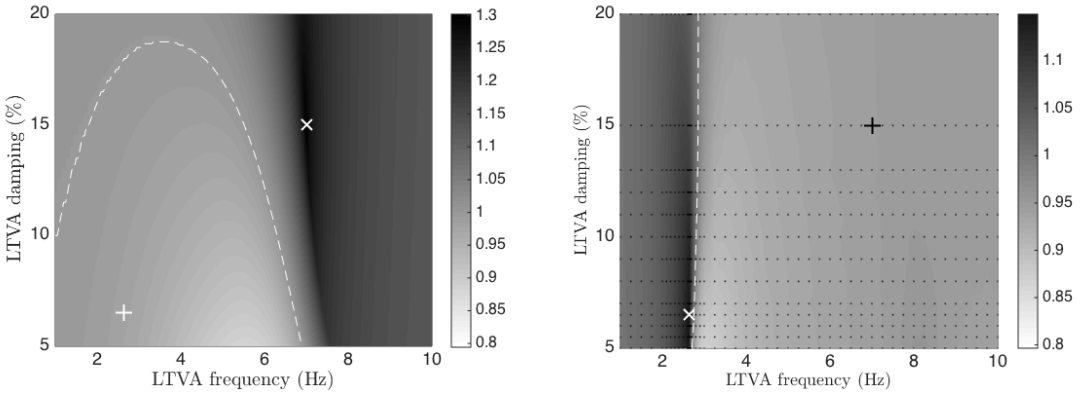

(a) Overlying linear system relative flutter speed (b) Relative LCO onset speed

Figure 5.4: Critical airspeeds of the system depending on the absorber tuning. The LTVA is attached in $x_a = -0.25 \times c$.

of the overlying linear system. Furthermore, this absorber decreases the LCO frequency.

Absorber 2 (orange) increases the LCO onset speed to 9.27 m/s (+0.99%) and slightly reduces the LCO amplitude in all three DOFs. The frequency variation with airspeed is not significantly affected by the absorber. Even though the grazing airspeed is increased by 673%, the LCO onset speed is not significantly increased, which indicates that tuning the absorber on the underlying linear system is not a good option.

Absorber 3 (blue) is optimised for the nonlinear system. The LCO onset speed is increased to 9.87 m/s (+7.7%) and the LCO amplitude is decreased on all three DOFs. Moreover, the airspeed range where large amplitude control surface deflections are observed is reduced from [9.16 − 11.05] m/s to [9.87 − 10.32] m/s. Such an absorber also increases the LCO frequency and leads to an abrupt frequency variation with airspeed close to the LCO onset speed.

Figure 5.6 plots the relative LCO amplitude reduction due to the addition of the absorber as a function of the airspeed. At each stabilised airspeed considered, direct numerical simulations with large initial conditions were performed on the system with and without absorber and the amplitude of the stabilised LCOs were compared. A positive value means the addition of the absorber leads to a reduction in LCO amplitude while a negative value corresponds to an increase in LCO amplitude. The vertical dashed lines indicate 85% of the linear flutter speed of the system without absorber, i.e. the worst case limits of the flight envelope of a military aircraft flying without LTVA.

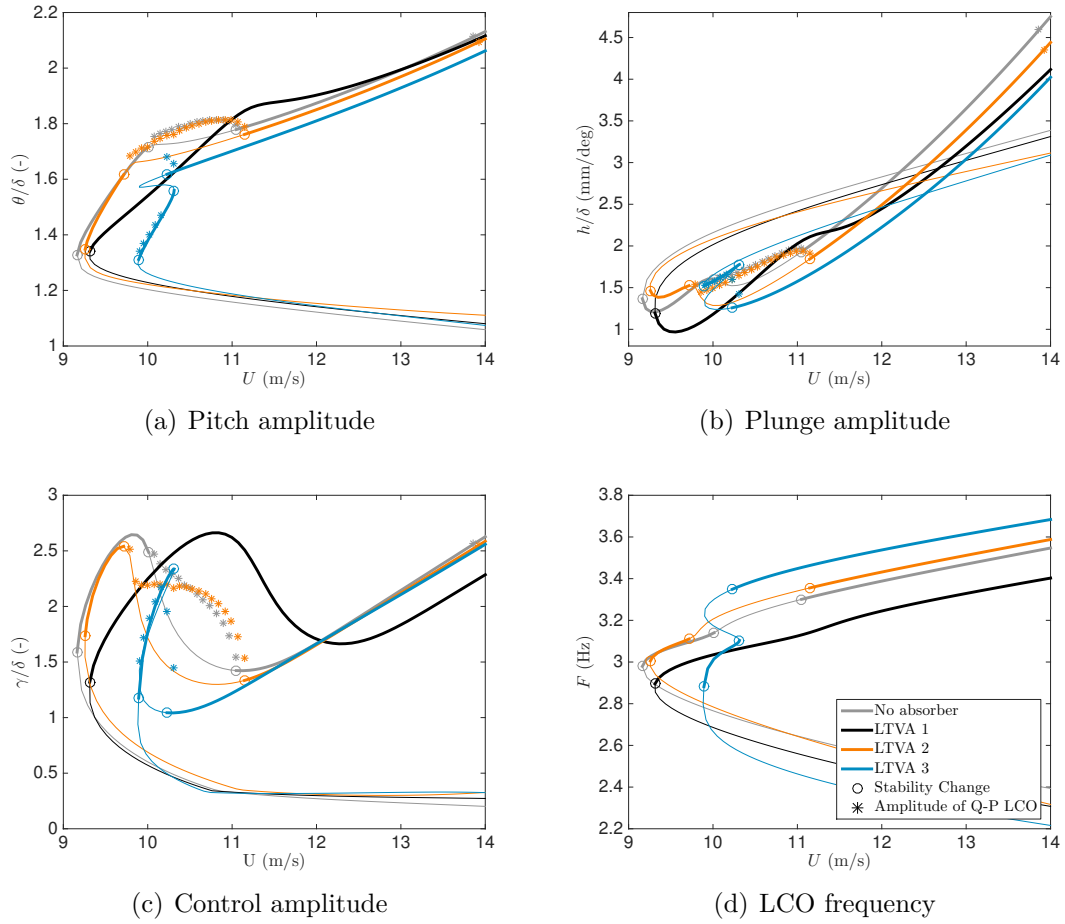

(a) Pitch amplitude

(b) Plunge amplitude

(c) Control amplitude

(d) LCO frequency

Figure 5.5: Bifurcation diagram of the system with linear absorbers

As demonstrated in figure 5.5, absorber 1 has a detrimental effect on the system's response in a narrow airspeed range close to the LCO onset speed. Nevertheless, this detrimental effect occurs when the airspeed and the LCO amplitude are small. As the airspeed (and therefore the LCO amplitude) is increased, the equivalent linear stiffness of the system is increased and the absorber's performance is improved. The reduction in pitch, plunge, and control surface deflection LCO amplitude reach 20%, 40% and 40%, respectively, at the boundary of the flight envelope. LTVA 2 is not stiff enough to affect the system's response and is practically useless over the whole airspeed range, which further indicates that it is not a good option. Finally, absorber 3 decreases pitch plunge and control surface LCO amplitude by 5% to 8%, 8% to 18% and 4%, respectively, throughout the flight envelope without any detrimental effect. Moreover a large control surface deflection amplitude reduction is observed below airspeeds of 11.25 m/s because of the

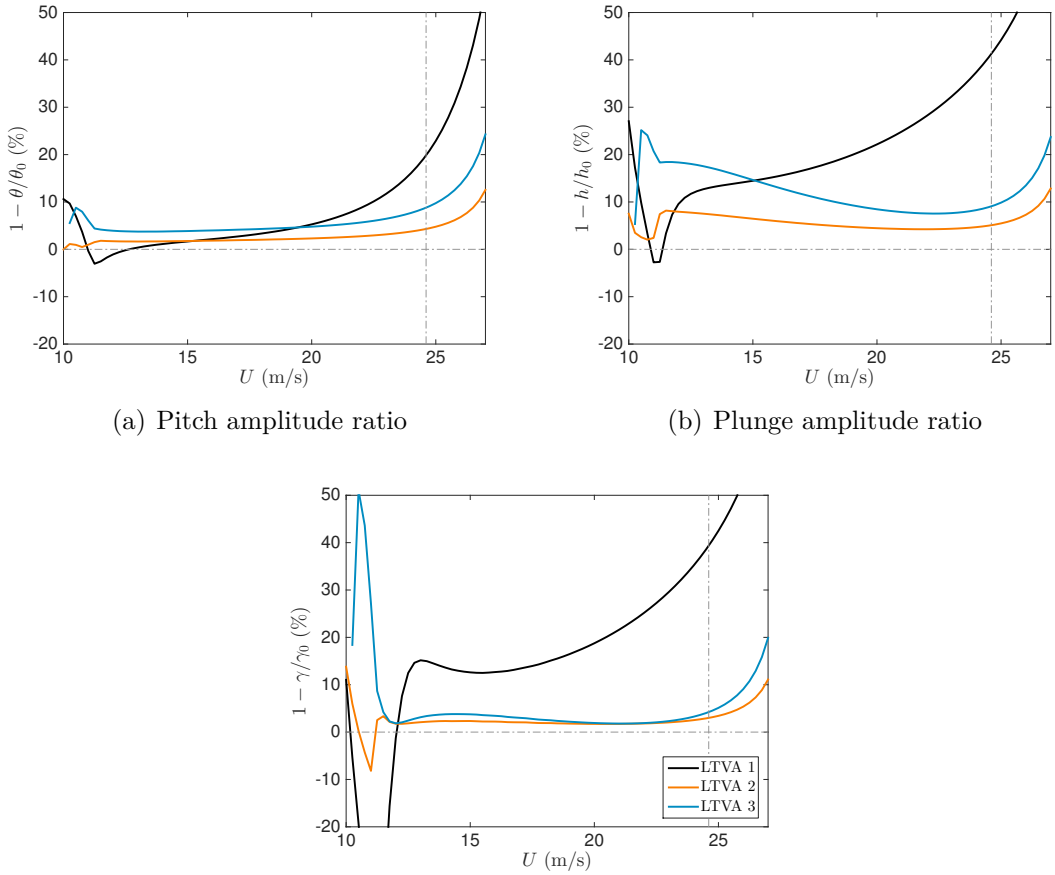

(a) Pitch amplitude ratio

(b) Plunge amplitude ratio

(c) Control surface amplitude ratio

Figure 5.6: Overview of the performance of the linear absorbers

shrinking of the large amplitude lobe observed in figure 5.5(c). Because the frequency of LTVA 3 is lower than that of LTVA 1, it is more effective close to the LCO onset speed but less effective at higher airspeeds.

5.5 Nonlinear tuned vibration absorber investigation

Linear absorbers are very sensitive to the primary system's frequency, which varies with airspeed and amplitude in the present case. A potential option for improving the performance of absorbers in such systems is the addition of a nonlinear restoring force. Habib et al. [114] demonstrated that for optimal performance in forced vibration, the nonlinearity in the absorber should mimic that of the primary system. In this work, cubic and freeplay nonlinearities are tested and compared. The former nonlinearity is smooth and therefore simpler while the latter respects the principle of similarity. The NLTVA's linear parts are set to the values of LTVA 3 and the goal is to achieve performance similar or higher than LTVA 1 at high speed while maintaining the good performance of LTVA 3 in the vicinity of the LCO onset speed.

Unlike the LTVA, the NLTVA's performance depends on the LCO amplitude, i.e. on the freeplay gap δ. As a result, the predictions in this section are only valid for $\delta = 5$ deg. A robustness study should be performed with different values of freeplay gap or absorbers with variable nonlinear stiffness should be designed however this is beyond the scope of this thesis.

5.5.1 Cubic hardening NLTVA

The cubic NLTVA is an absorber whose linear components are identical to those of LTVA 3 but which also features a cubic hardening spring of restoring force

$$F_{nl}(\Delta\xi) = c_{nl} \times k_a \times \Delta\xi^3 \tag{5.7}$$

where c_{nl} has to be tuned to achieve the best performance.

Figure 5.7 plots the bifurcation diagram of the system with four NLTVAs based on LTVA 3. Subfigures 5.7(a) to 5.7(d) correspond to bifurcation diagrams in LCO pitch, plunge, and control surface deflection amplitude and in LCO frequency, respectively. The grey, orange, blue and black lines correspond to $c_{nl} = 0$, $c_{nl} = 100$, $c_{nl} = 200$ and $c_{nl} = 300$, respectively. The thin lines correspond to unstable responses while the thick ones are related to stable solutions.

Previous research on systems with continuous nonlinearities [108, 109, 114] found optimal nonlinear parameters to suppress the sub-criticality that is introduced by the linear absorber in the system. In this more complex system, no clear optimal nonlinear parame-

ter was found. The nonlinearity has a very small effect on the LCO onset speed and each nonlinear parameter has a beneficial effect in one airspeed speed range and a detrimental effect in another.

At airspeeds close to the LCO onset speed, the nonlinearity reduces the rapidity of the pitch, plunge and control surface amplitude growth however it delays the point where the response jumps down to lower levels. This is especially noticeable on the plunge and control surface bifurcation diagrams. At intermediate airspeeds ($12 < U < 20$), all three nonlinear absorbers reduce the LCO amplitude compared to the LTVA and it is very difficult to define an optimal absorber as each absorber is optimal on a given DOF in a given airspeed range. At higher airspeeds ($U > 20$), all three nonlinear absorbers have similar detrimental effect on the response and lead to a LCO amplitude slightly higher than the linear absorber.

Figure 5.8 plots the relative LCO amplitude reduction due to the addition of the absorber as a function of the airspeed. At each stabilised airspeed considered, direct numerical simulations with large initial conditions were performed on the system with and without absorber and the amplitudes of the stabilised LCOs were compared. A positive value means the addition of the absorber leads to a reduction in LCO amplitude while a negative value corresponds to an increase in LCO amplitude. The vertical dashed lines indicate 85% of the linear flutter speed of the system without absorber, i.e. worst case limits of the flight envelope of a military aircraft flying without LTVA. All three nonlinear absorbers outperform the LTVA in most of the flight envelope, especially on the plunge and control surface DOFs where the LCO amplitude reduction reach up to 36% and 45%, respectively. Nevertheless, such nonlinear absorbers increase the large amplitude control surface deflection area (see figure 5.7(c)) and increase the pitch LCO amplitude for airspeeds above approximately 20 m/s and therefore have a negative impact on the system in some airspeed regions. The airspeed region where each absorber performs best depends on the nonlinear coefficient and no clear optimal value was found. As a result, the absorber should be tuned according to the flight region of interest.

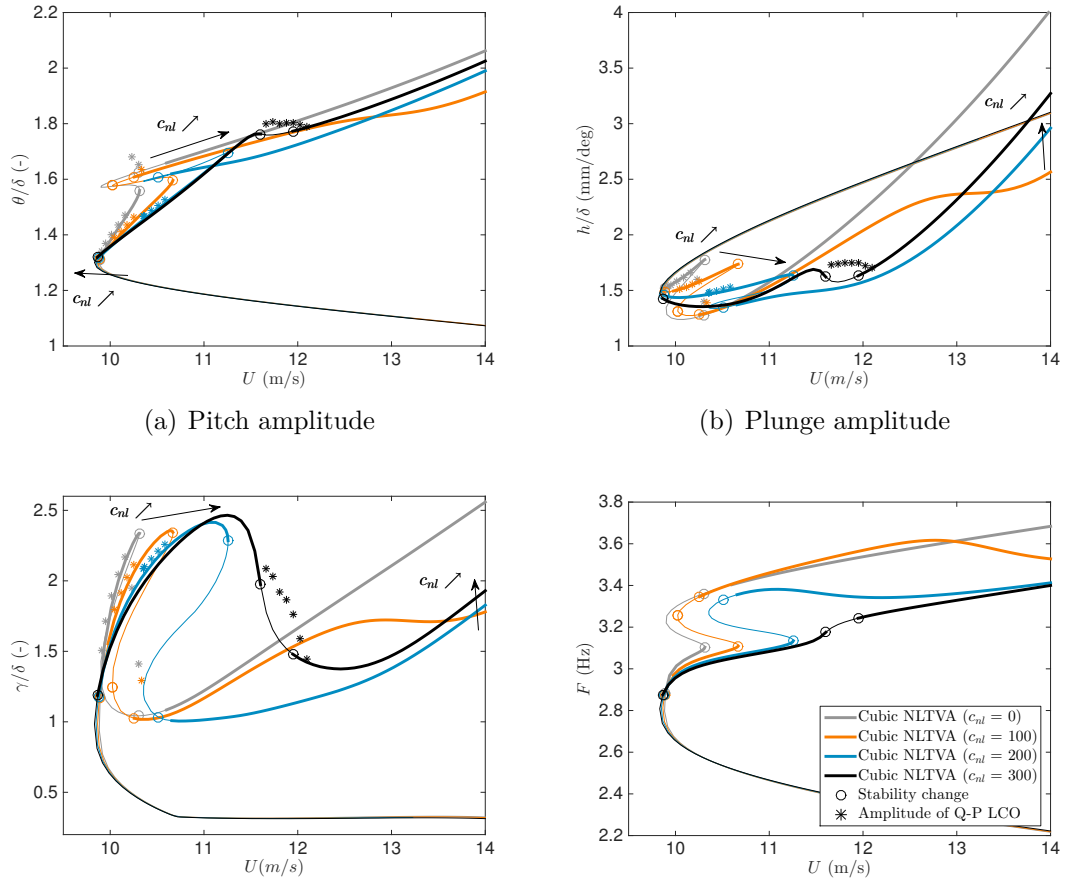

(a) Pitch amplitude

(b) Plunge amplitude

(c) Control amplitude

(d) LCO frequency

Figure 5.7: Bifurcation diagram of the system with cubic nonlinear absorbers based on LTVA 3

5.5.2 Freeplay NLTVA

The freeplay NLTVA has all the linear features of LTVA 3 with a nonlinear spring of restoring force given by

$$F_{nl}(\Delta\xi) = \begin{cases} c_{nl} \times k_a \times (\Delta\xi + \Delta\xi_0) & \text{if} \quad \Delta\xi < -\Delta\xi_0 \\ 0 & \text{if} \quad |\Delta\xi| \leq \Delta\xi_0 \\ c_{nl} \times k_a \times (\Delta\xi - \Delta\xi_0) & \text{if} \quad \Delta\xi > \Delta\xi_0 \end{cases} \tag{5.8}$$

added in parallel to the linear spring of stiffness k_a. The clearance is $\Delta\xi_0$ and the hardening outside the freeplay gap is given by c_{nl}. Note that this nonlinear freeplay spring is attached in parallel to the linear spring of the absorber so the total restoring force is actually bi-linear rather than a pure freeplay force.

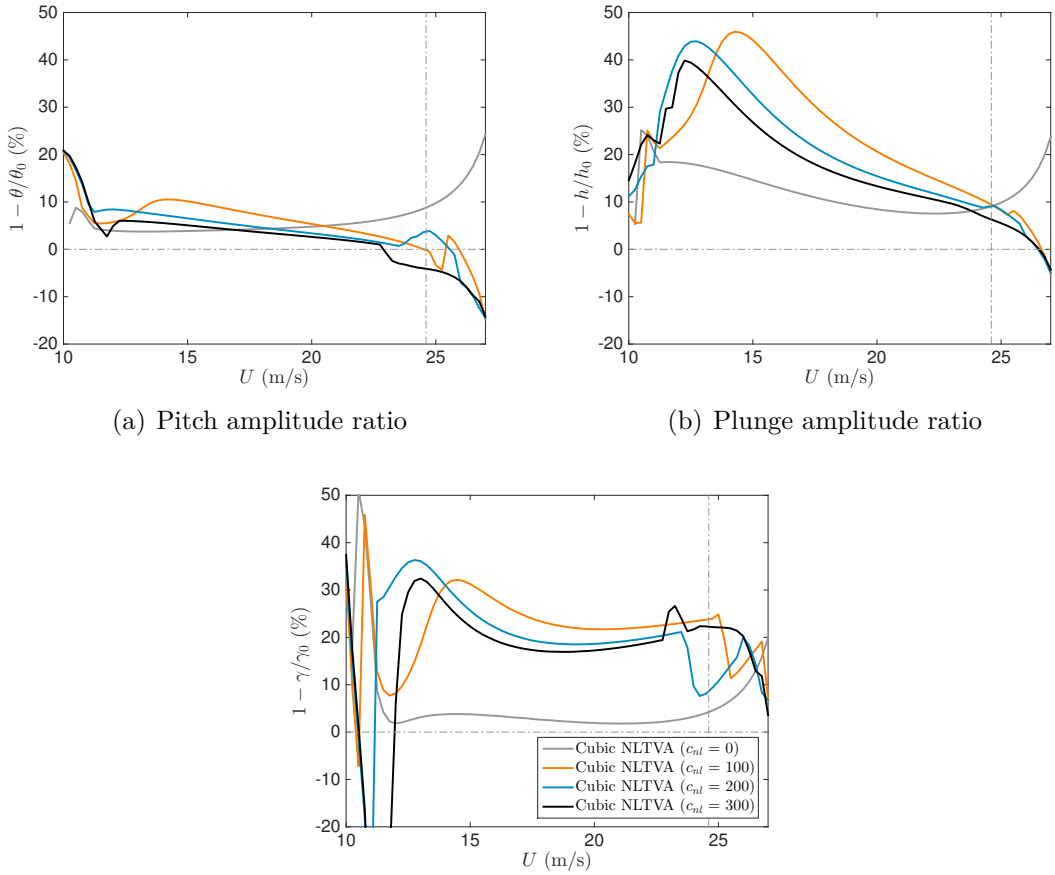

(a) Pitch amplitude ratio

(b) Plunge amplitude ratio

(c) Control surface amplitude ratio

Figure 5.8: Overview of the performance of cubic nonlinear absorbers based on LTVA 3

The first freeplay NLTVA considered is tuned in order to keep the large amplitude control surface deflection region as narrow as with the LTVA. The nonlinear parameters are $\Delta\xi_0 = 0.03$ & $c_{nl} = 1$ (i.e. the stiffness is doubled outside the freeplay range). A second absorber is tuned in order to have an effect similar to that of the cubic absorber with $c_{nl} = 200$ at low airspeeds. The nonlinear parameters of this NLTVA are $\Delta\xi_0 = 0.02$ & $c_{nl} = 0.7$.

Figure 5.9 plots the bifurcation diagram of the system with the LTVA (grey), with a cubic NLTVA with $c_{nl} = 200$ (blue), with the first freeplay NLTVA (orange) and with the second freeplay NLTVA (black). Subfigures 5.9(a) to 5.9(d) correspond to bifurcation diagrams in LCO pitch, plunge, and control surface deflection amplitude and in LCO frequency, respectively. The thin lines correspond to unstable responses while the thick

ones are related to stable solutions.

The first freeplay NLTVA (black, larger clearance) has a clearance that is not reached close to the LCO onset speed. As a result, the absorber behaves like a LTVA which leads to a rapid increase in pitch LCO amplitude but also keeps the airspeed range where large amplitude control surface deflection oscillations are observed narrow. At higher airspeeds, this absorber outperforms all the others considered.

The second freeplay NLTVA (orange, smaller clearance) has an effect very similar to that of the cubic hardening absorber close to the LCO onset speed thanks to its small clearance. The main difference is that a small region of quasi-periodic response is observed close to 11 m/s.

The two bilinear absorbers considered offer a reduction in plunge and control surface LCO amplitude similar to that of the cubic absorber but over a much wider airspeed range. Moreover, the addition of the freeplay force greatly improves the reduction in pitch LCO amplitude, which reaches up to 29%, while the LTVA had a negligible effect and the cubic NLTVA led to an increase in LCO amplitude at the boundary of the flight envelope. As a result, the proposition of Habib et al. [114] that the nonlinearity in the absorber should mimic that of the primary system appears to be valid for this system. Nevertheless, the clearance of the absorber has been tuned for $\delta = 5$ deg and the performance might be diminished for other freeplay gaps. As a result, prior to potential tests, a robustness study should be performed or adaptable absorbers should be designed.

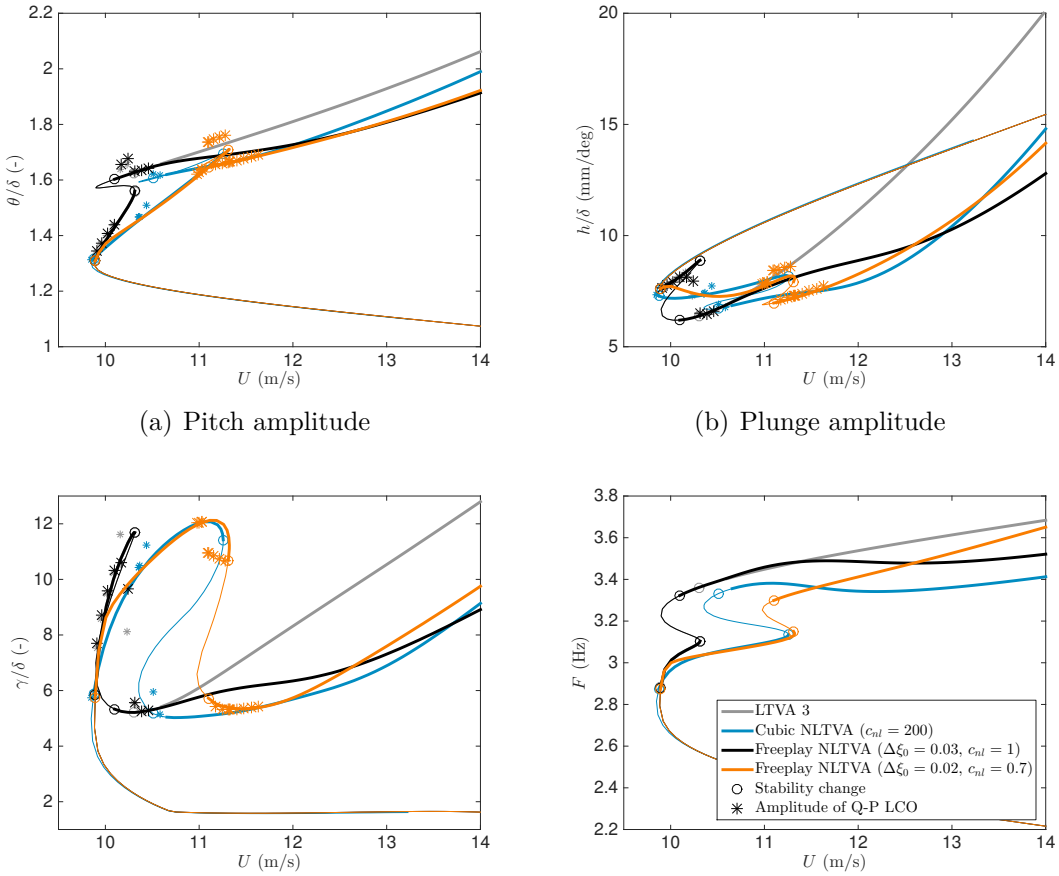

(a) Pitch amplitude

(b) Plunge amplitude

(c) Control amplitude

(d) LCO frequency

Figure 5.9: Bifurcation diagram of the system with freeplay and cubic nonlinear absorbers based on LTVA 3

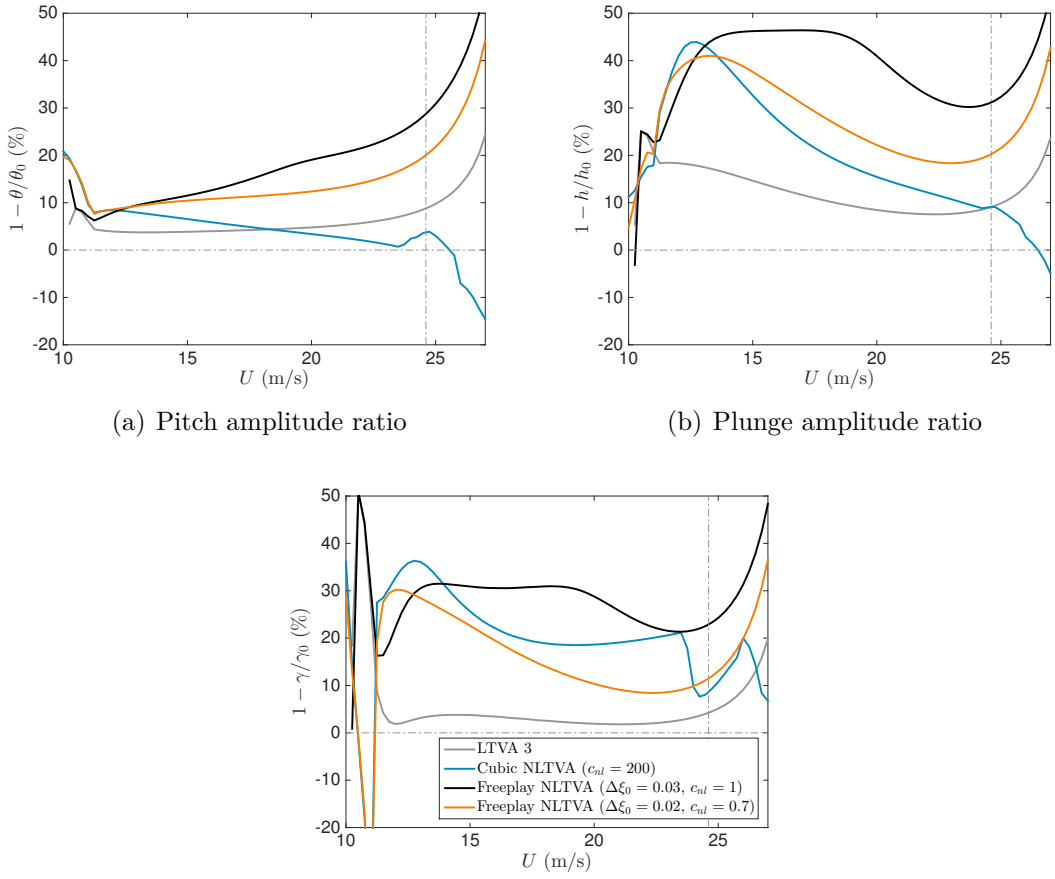

(a) Pitch amplitude ratio

(b) Plunge amplitude ratio

(c) Control surface amplitude ratio

Figure 5.10: Overview of the performance of cubic and bilinear nonlinear absorbers based on LTVA 3

5.6 Chapter summary

This chapter demonstrates that linear and nonlinear tuned vibration absorbers can have a beneficial effect on a wing with pitch, plunge and control surface deflection DOFs, with and without freeplay.

The linear absorbers considered can either increase the flutter speed of the system without freeplay by 10% or delay the LCO onset speed by 7.7% and reduce the LCO amplitude of the nonlinear system but never both at the same time. This mediocre increase in linear flutter speed compared to other studies is due to the position of the absorber, which lies very close to the pitch axis and to the wing's center of mass. Nevertheless, freeplay induced LCOs occur at airspeeds so much smaller than the linear flutter speed of the system that it is difficult to repel them outside the flight envelope. As a result, the emphasis should be placed on the reduction in LCO amplitude rather than in the increase in LCO onset speed. In this respect, LTVAs 1 and 3 offered good performance.

The addition of a cubic nonlinear force to the absorber optimised for the system with freeplay (LTVA 3) did not further increase the LCO onset speed but led to a substantial reduction in LCO amplitude in a given airspeed region and to an increase in LCO amplitude in another airspeed region, irrespective of the value of the nonlinear parameter. As a result no clear optimal tuning was found and such cubic absorbers should be set up depending on the critical airspeed range of the application. Conversely, the addition of a freeplay nonlinear force to the absorber led to a substantial reduction in LCO amplitude in a large airspeed range without any drawback. This is consistent with the assertion by Habib et al. [114] that the nonlinearity in the absorber should mimic the nonlinearity in the primary system. Nevertheless, nonlinear absorbers are sensitive to the width of the freeplay gap and should therefore either be able to adapt themselves or a sensitivity study should be performed.

Chapter 6

Conclusions

The main thrust of this thesis was to demonstrate numerically and experimentally the performance of linear and nonlinear tuned vibration absorbers for flutter and LCO suppression in nonlinear aircraft-like aeroelastic systems. They were achieved on two archetypical aeroelastic systems following the four-phase NLTVA design and validation procedure depicted in figure 6.1:

1. The aeroelastic response of the nonlinear systems is investigated in the wind tunnel.

2. Mathematical models using 2 or 3 DOFs are derived using linear unsteady aerodynamics and the model predictions are compared to wind tunnel data.

3. The mathematical models are used to design optimal linear and nonlinear absorbers and to investigate their effect on the LCO branches.

4. The absorbers designed in step 3 are built and tested in the wind tunnel in order to demonstrate their performance.

Experiments and computations on a pitch-flap wing with a hardening nonlinearity in pitch demonstrated the potential of the (N)LTVA for linear flutter and LCO suppression. The mathematical models indeed predicted an increase in flutter speed of 36% and an increase in LCO onset speed of 32% using a LTVA, the difference between the two being due to detuning of the absorber at large enough pitch angles because of the hardening nonlinearity. The addition of a nonlinearity mimicking that of the primary system to the absorber restored the super-critical nature of the bifurcation at the cost of increased complexity and isolated solution branches. Experiments confirmed the predicted increase in flutter speed with a LTVA, which increased the system's flutter speed by 36% and suppressed a jump induced by stall flutter. However, the effect of the NLTVA could not be demonstrated because no LTVA with a stiffness sufficiently small to experience a detuning could be built.

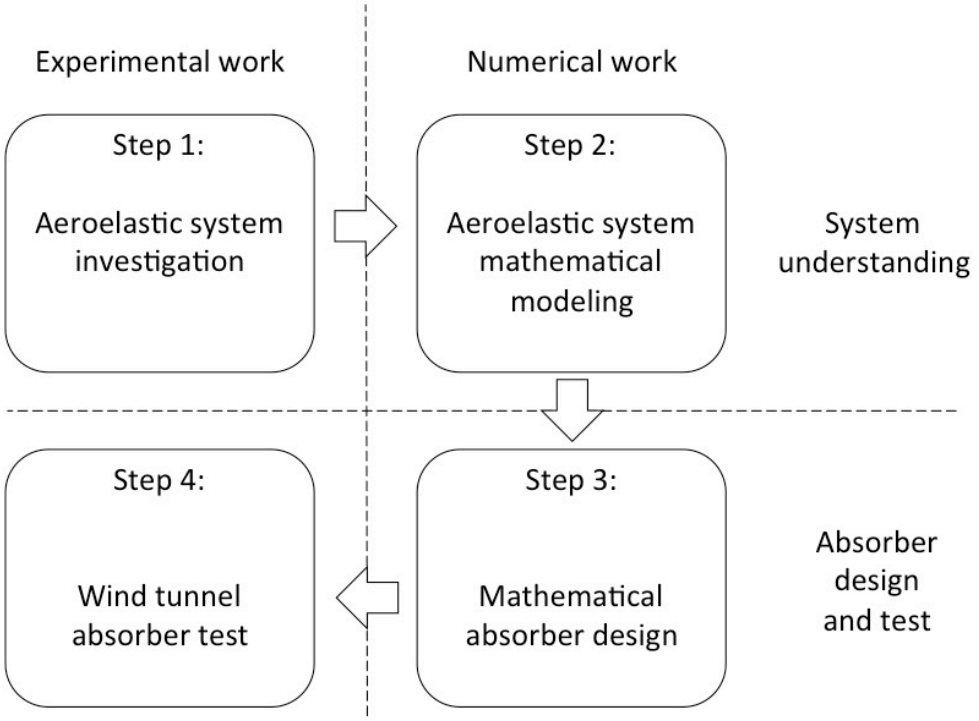

Figure 6.1: Flow chart of the NLTVA design procedure

Computations on a pitch-plunge-control wing with freeplay in pitch yielded quite different results. In this case, the LTVA offered, depending on its location, an increase in LCO and linear flutter speed of only 7.7% and 1.1%, respectively. This poor performance compared to that achieved in the first case is probably due to the large variation of stiffness that the system is experiencing. The equivalent linear stiffness of this system indeed varies between 0 at the grazing point (underlying linear system) to k_θ (overlying linear system) when the amplitude is large, i.e. close to the flutter speed of the overlying linear system, while a much lower stiffness variation was observed in the pitch-flap wing. In spite of this poor performance for LCO delay, a reduction in LCO amplitude of the order of 5% to 10% was achieved using a LTVA and of the order of 10% to 45% using a bilinear NLTVA (i.e. a nonlinearity that mimics that of the primary system).

In spite of the promising results achieved on these two systems, the absorber's frequency had to be tuned with an accuracy lower than 0.1 Hz for optimal flutter delay on both systems. This sensitivity combined to that fact that aircraft fly with different payloads and burn fuel means that either the LTVA can be tuned on the worst case scenario or that LTVAs able to modify their natural frequency have to be designed for potential real life

applications. The latter would mean that the absorber is not longer fully passive. Moreover, the very different results obtained on the two systems means that the conclusions of the present work can probably not be extrapolated to other nonlinear flutter phenomena such as transonic buzz or store-induced LCOs, which would required dedicated (N)LTVA studies.

In summary, this thesis contains the following achievements:

- The most complete investigation to date of the performance of LTVAs and NLTVAs on aeroelastic systems with continuously hardening, bilinear and dynamic stall nonlinearities.
- The first ever experimental demonstration of the fact that a LTVA can not only delay classical flutter but also delay/suppress stall flutter.
- A thorough linking of the performance of both LTVAs and NLTVAs to the complete bifurcation behaviour of uncontrolled and controlled systems.
- A discussion of the effect of LTVAs and NLTVAs on the shape of the limit cycle branches of the system and on the appearance of isolated branches.
- The first experimental observation of the co-existence of two-domain LCOs, three-domain LCOs and fixed points in systems with freeplay.

6.1 Suggestions for future work

Experimental NLTVA demonstration

Only the performance of the linear absorber was demonstrated in the wind tunnel. Further work should aim to demonstrate experimentally the performance of the NLTVA and to verify the existence of the isolated solution branches observed in chapter 3. A rigid wing with pitch and plunge DOFs and a hardening nonlinearity in the pitch DOF is currently ready for testing at the University of Liège and a nonlinear absorber is ready to be attached. The wing, depicted in figure 6.2(a), consists of a composite skin with an aluminium internal structure attached to mobile supports by means of bearings and a leaf spring that provides a strongly hardening pitch restoring torque. Additional leaf springs suspend the wing / mobile supports assembly and provide a linear plunge DOF. The absorber, displayed in figure 6.2, is made of a mass attached to the primary system by means of a carriage, two linear traction springs and an adjustable dashpot. The absorber's natural frequency can be adjusted by changing the linear springs and can be finely tuned

by varying the mass from 125 g to 207 g while the damping can be adjusted by means of a screw that regulates the pressure losses in the dashpot. Finally, a transverse wire inspired by experimental work on the NES [80–82] is attached to provide a mostly cubic restoring force. This nonlinear force can be adjusted by changing the wire length, diameter and material.

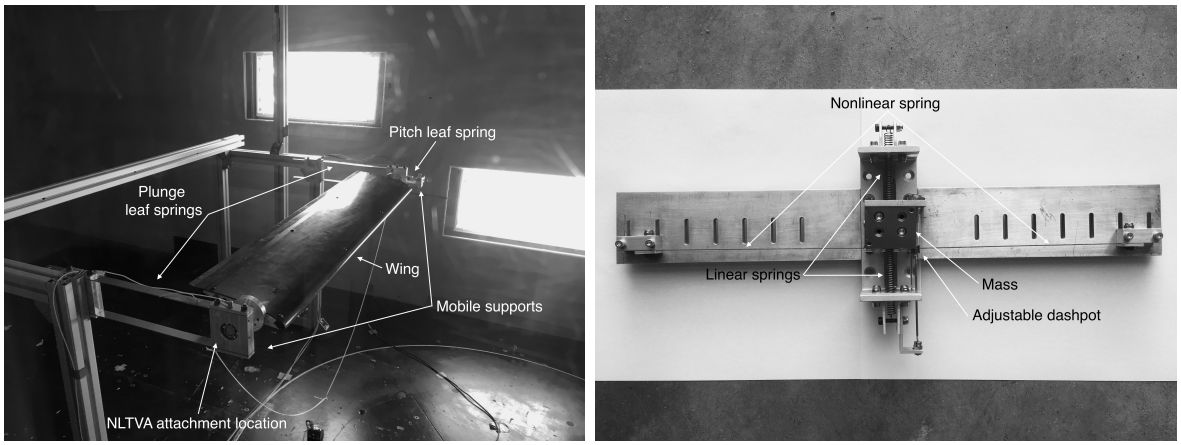

(a) Pitch and plunge wing (b) NLTVA

Figure 6.2: Photographs of the pitch and plunge wing and of the NLTVA

Realistic aeroelastic systems

This thesis only demonstrated the potential of the absorbers on two and three DOF systems with freeplay and hardening nonlinearities. More realistic structures should be considered both numerically and in the wind tunnel. First dimensional analysis should be applied in order to upscale the results to larger and heavier structures. Such a study might also lead to the derivation of tuning rules similar to those of Den Hartog for forced vibration systems, allowing to by-pass steps 2 and 3 of the flow chart proposed in figure 6.1. Then, full linear aircraft configurations should be investigated. With the advent of efficient unsteady CFD techniques (using the Harmonic Balance method for instance), the performance of the absorbers for mitigating other nonlinear aeroelastic phenomena such as transonic buzz could also be investigated. One of the initial goals of the ERC project that funded this thesis was the suppression of the store-induced LCOs observed on the F-16 fighter aircraft which are, up to this day, still not fully understood. Nevertheless, in 2016, Denegri et al. [120] proposed a numerical model that accurately represents one of the many types of LCOs observed on this aircraft using transonic aerodynamics and nonlinear friction in the junction between the wing and the external payload. Similar models could be used to assess the effectiveness of the absorber in this particular case.

Adaptative and piezoelectric absorbers

The present mathematical models and experiments showed that the LTVA can significantly increase the flutter speed of aeroelastic systems but the absorber's performance is closely related to the natural frequencies of both the absorber and the primary system. The mass and flight conditions of most aircraft change from one mission to another and during flights because they burn fuel and may carry and release different kinds of payload. As a result, their natural frequencies vary, which may (or may not) significantly reduce the absorber's effectiveness. A thorough robustness study using a full aircraft model with variable mass should be carried out. Such a study would either demonstrate that the absorber should be tuned for the most critical case or that the absorber is not robust enough to sufficiently increase the flutter speed in all the possible aircraft configurations. In the latter case, absorbers that adapt their natural frequency or their nonlinearity could be designed. One potential way of designing such absorbers would be using piezoelectric transducers and a RLC resonant shunt circuit with an inductance simulated by means of operational amplifiers and a micro-controller. Such RLC circuits indeed exhibit a behaviour similar to that of the mechanical LTVA, with the resistor playing a role similar to that of the dashpot, the capacitor playing a role similar to that of the spring and the inductor mimicking the absorber's mass. Using a micro-controller to simulate the inductance requires a power supply however it allows the system to adapt its inductance in real time and to deliver any desired nonlinearities including freeplay. Experiments on such a RLC circuit are currently being carried out in the Space Structures and Systems Lab (S3L) at the University of Liège on a nonlinear beam (see figure 6.3).

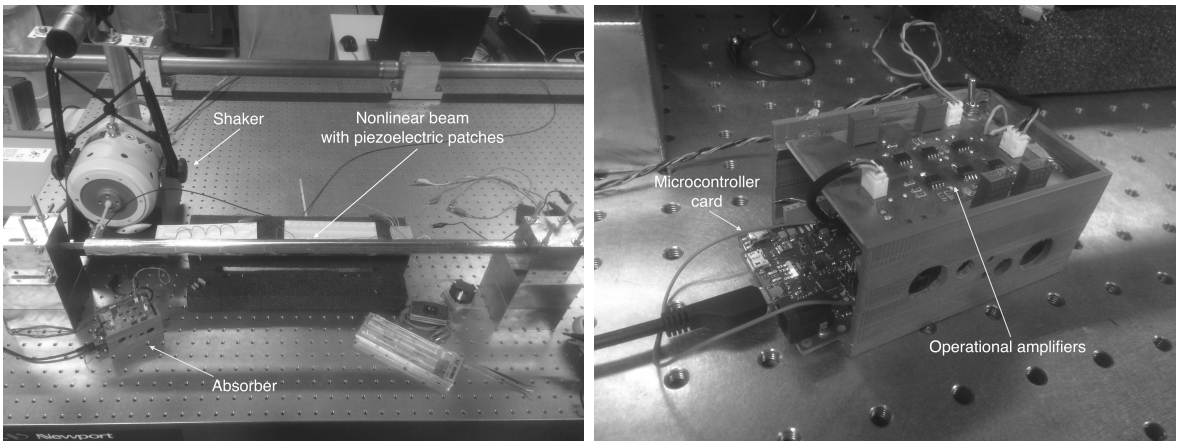

(a) Nonlinear beam (b) Microcontroller

Figure 6.3: Photographs of the nonlinear beam and the RLC resonant shunt at S3L

Appendix A

Wind tunnel of the University of Liège

The wind tunnel of University of Liège was built in 1999 in the Sart-Tilman campus, with funding from the Walloon Region and the European Commission. It is a low speed multidisciplinary wind tunnel that can be operate in closed loop or in open loop, under atmospheric pressure. Furthermore, experiments can be carried-out in two test sections, depending on the size of the model:

- Aeronautical test section (TS1)
- Wind engineering test section (TS2)

The main characteristics of the two sections are specified in table A.1.

Characteristics	TS1	TS2
Dimensions (Width x Height x Length)	2m x 1.5m x 5m	2.5m x 1.8m x 5m
Airspeed Range (Closed/Open loop)	2-65m/s / 2:40m/s	2-40m/s / 2-30m/s
Test section turntable diameter	1.5m	2.0m
Thermal stability	$1°C$	$1°C$
Streamwise static pressure gradient	0.3% per meter	0.5% per meter
Mean angle divergence	$< 0.2\%$	$< 0.2\%$
Speed non-uniformity	$< 0.5\%$	$< 0.8\%$
Turbulence level	0.15%	$< 0.23\%$

Table A.1: Characteristics of the wind tunnel of ULg

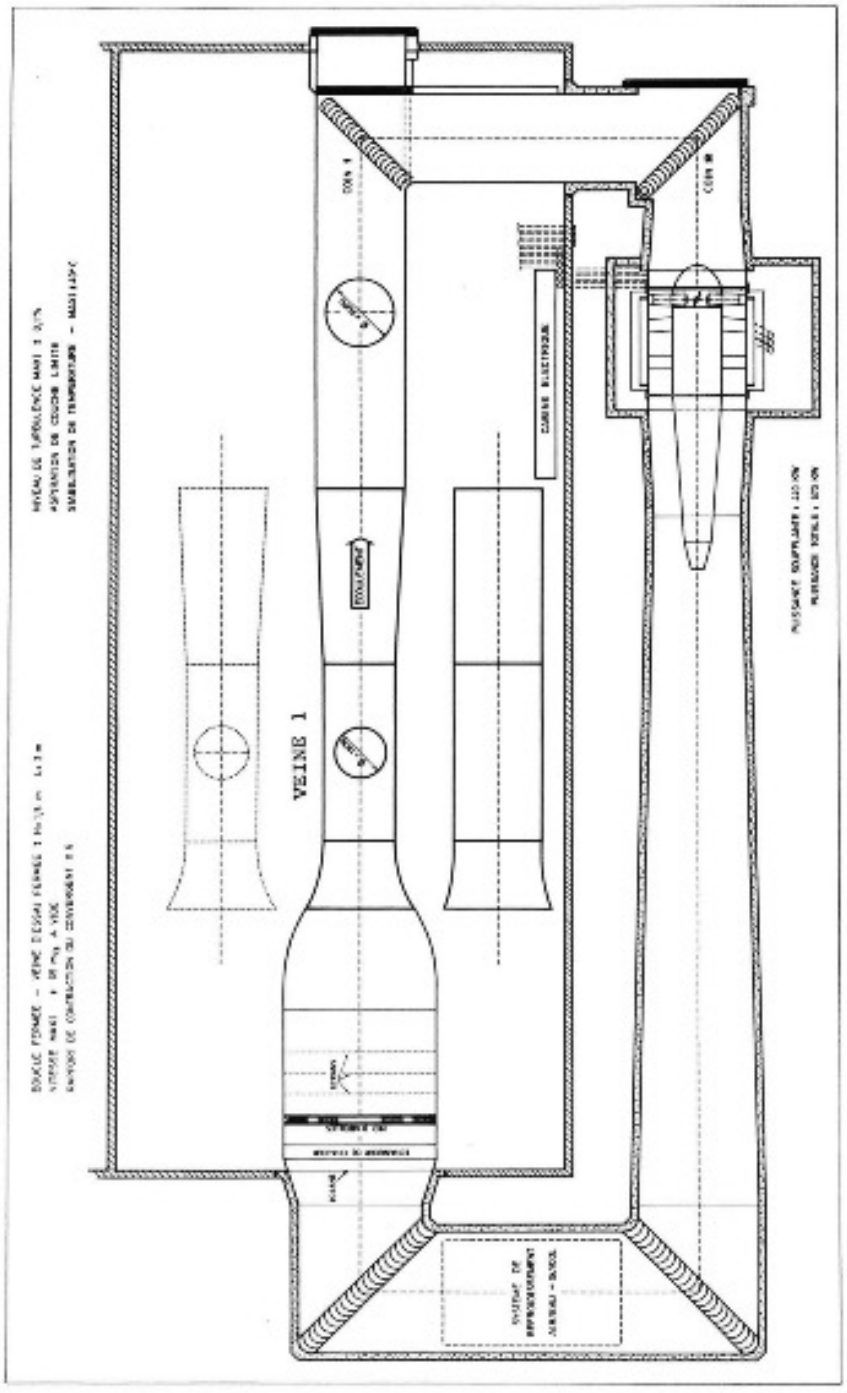

Figure A.1: Wind Tunnel of ULg: schematic view

Figure A.2: Wind Tunnel of ULg: aeronautical test section (TS1)

Figure A.3: Wind Tunnel of ULg: wind engineering test section (TS2)

Appendix B

Wind tunnel of the University of Duke

The wind tunnel of Duke University is located in the Hudson building of the West campus. It is a low speed wind tunnel that operates in closed loop under atmospheric pressure. The test section is 0.701 m wide, 0.506 m high and 1.219 m long. The airspeed, measured by means of a hot wire anemometer, can reach 89 m/s thanks to a 75 hp electric motor. The stagnation temperature of the airstream is held constant over the range 15 to 38° C by means of an external air-exchange system, and tunnel stagnation pressure equals the atmospheric pressure at the low Reynolds number operating conditions. Figure B.1 shows the test section of the wind tunnel with a model and the anemometer.

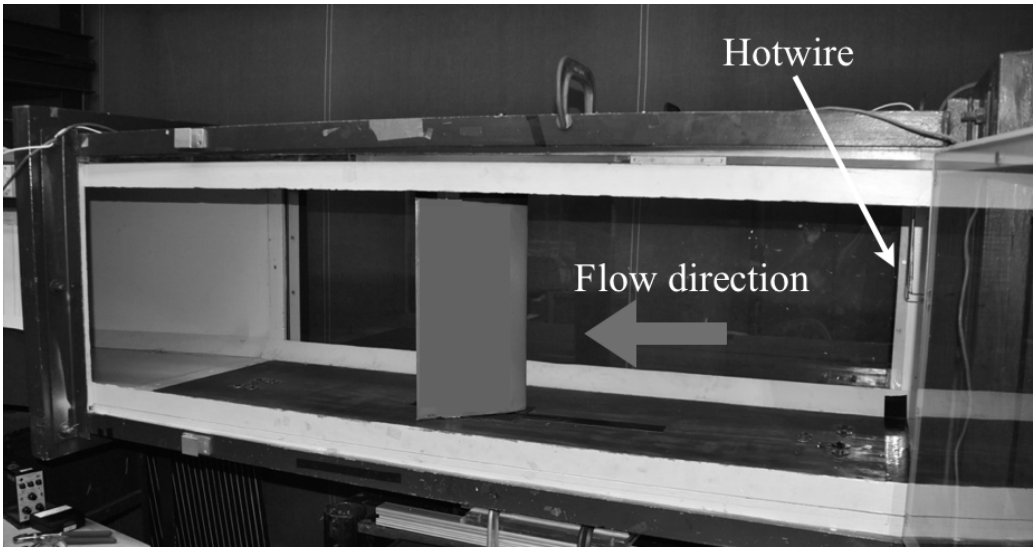

Figure B.1: Duke University Wind tunnel

Appendix C

Equations of motion of the pitch-flap wing

The structural and aerodynamic matrices appearing in equations 2.13 and 3.2 are given in the following appendix, and the values of all the relevant parameters are detailed in table C.1.

Structural matrices

The structural inertia, **A**, damping, **C**, and stiffness, **E**, matrices are respectively given by

$$\mathbf{A} = \begin{pmatrix} I_\alpha & S \\ S & I_\theta \end{pmatrix}$$

$$\mathbf{C} = \begin{pmatrix} c_\alpha & c_{\alpha\theta} \\ c_{\alpha\theta} & c_\theta \end{pmatrix}$$

$$\mathbf{E} = \begin{pmatrix} k_\alpha & k_{\alpha\theta} \\ k_{\alpha\theta} & k_\theta \end{pmatrix}$$

LTVA matrices

Adopting the Euler-Lagrange equation and assuming small displacements, the equations of motion of the NLPFW coupled to a rotational LTVA of mass m_a, stiffness k_a, damping c_a, rod length r_a located in r_θ and r_α are derived. The resulting LTVA inertia, damping

and stiffness matrices are given by

$$\mathbf{A}_{ltva} = m_a \begin{pmatrix} r_\alpha^2 & r_\alpha(r_\theta + r_a) & r_\alpha r_a \\ r_\alpha(r_\theta + r_a) & (r_\theta + r_a)^2 & (r_\theta + r_a)r_a \\ r_\alpha r_a & (r_\theta + r_a)r_a & r_a^2 \end{pmatrix}$$

$$\mathbf{C}_{ltva} = c_a \begin{pmatrix} 0 & 0 & 0 \\ 0 & 0 & 0 \\ 0 & 0 & 1 \end{pmatrix}$$

$$\mathbf{E}_{ltva} = k_a \begin{pmatrix} 0 & 0 & 0 \\ 0 & 0 & 0 \\ 0 & 0 & 1 \end{pmatrix}$$

Aerodynamic matrices

The aerodynamic inertia, $\mathbf{B}$, damping, $\mathbf{D}$, and stiffness, $\mathbf{F}$, matrices are written as

$$\mathbf{B} = \pi b^2 \begin{pmatrix} \Lambda_3/3 & -ab\Lambda_2/2 \\ -ab\Lambda_2/2 & b^2\Lambda_1(a^2 + 1/8) \end{pmatrix}$$

$$\mathbf{D} = \pi b \begin{pmatrix} \frac{2}{3}\Phi(0)\Lambda_3 & b\Lambda_2[1/2 - \Phi(0)(1 - a/2)] \\ -b\Lambda_2\Phi(0)(a + 1/2) & -\Lambda_1 b^2(a - 1/2)[1 + 2\Phi(0)(a + 1/2)] \end{pmatrix}$$

$$\mathbf{F} = \pi \begin{pmatrix} \frac{2}{3}\Lambda_3[\frac{b\dot{\Phi}(0)}{U}] & b\Lambda_2[\Phi(0) + \frac{b\dot{\Phi}(0)}{U}(1/2 - a)] \\ -b\Lambda_2[\frac{b\dot{\Phi}(0)}{U}(a + 1/2)] & -2\Lambda_3(a + 1/2)[\Phi(0) - \frac{b\dot{\Phi}(0)}{U}(a - 1/2)] \end{pmatrix}$$

respectively. The aerodynamic states matrix, $\mathbf{W}$, is written as

$$\mathbf{W} = \pi \begin{pmatrix} -2\varepsilon_1^2\psi_1\Lambda_3/3b & \varepsilon_1^2\psi_1\Lambda_2(2a + 1)/2 \\ -2\varepsilon_2^2\psi_2\Lambda_3/3b & \varepsilon_2^2\psi_2\Lambda_2(2a + 1)/2 \\ \Lambda_2(\varepsilon_1\psi_1 - \varepsilon_1^2\psi_1/2 + a\varepsilon_1^2\psi_1) & -2b\varepsilon_1\psi_1\Lambda_1(a + 1/2)(\varepsilon_1(a - 1/2) + 1) \\ \Lambda_2(\varepsilon_2\psi_2 - \varepsilon_2^2\psi_2/2 + a\varepsilon_2^2\psi_2) & -2b\varepsilon_2\psi_2\Lambda_1(a + 1/2)(\varepsilon_2(a - 1/2) + 1) \end{pmatrix}^T$$

$\Phi(t)$, the Wagner function, approximates the growth of circulation around the airfoil after an impulsive change in angle of attack. It is given by

$$\Phi(t) = 1 - \psi_1 \exp(-\varepsilon_1 bt/U) - \psi_2 \exp(-\varepsilon_2 bt/U)$$

where $\Psi_1 = 0.165$, $\Psi_2 = 0.335$, $\varepsilon_1 = 0.0455$ and $\varepsilon_2 = 0.3$.

Finally, the aerodynamic state equations are given by

$$\mathbf{W}_1 = \begin{pmatrix} 1 & 0 \\ 1 & 0 \\ 0 & 1 \\ 0 & 1 \end{pmatrix}$$

$$\mathbf{W_2} = \begin{pmatrix} -\varepsilon_1/b & 0 & 0 & 0 \\ 0 & -\varepsilon_2/b & 0 & 0 \\ 0 & 0 & -\varepsilon_1/b & 0 \\ 0 & 0 & 0 & -\varepsilon_2/b \end{pmatrix}$$

	Wing dimensions		
Span	s	800	mm
distance (flap axis - wing root)	s_1	65	mm
distance (flap axis - wing tip)	s_2	865	mm
Pseudo span	Λ_j	$s_2^j - s_1^j$	mm^j
Chord	c	200	mm
Half Chord	b	100	mm
Thickness	t	4	mm
Position of the center of mass	x_{cg}	$0.5c$	mm
Flexural axis position	x_f	$0.3c$	mm
Relative position of x_f and x_{cg}	a	$\frac{x_f - x_{cg}}{b}$	-
	Inertial parameters		
Flap inertia	I_α	0.42	kg m^2
Pitch inertia	I_θ	0.029	kg m^2]
Static imbalance	S	0.029	kg m
	Stiffness parameters		
Flap stiffness	k_α	≈ 5	Nm/rad
Pitch linear stiffness	k_θ	10.1	Nm/rad
Cross stiffness term	$k_{\alpha\theta}$	0	Nm/rad
Pitch cubic stiffness	$k_{nl,3}$	860	Nm/rad^3
	Damping parameters		
Flap damping coefficient	c_α	0.025	Nm/rad s
Pitch damping coefficient	c_θ	0.003	Nm/rad s
Cross stiffness term	$c_{\alpha\theta}$	0	Nm/rad s
	Modal parameters		
Flap frequency	f_α	0.85	Hz
Pitch frequency	f_θ	3.1	Hz
Flap damping rate	ζ_α	≈ 1	%
Pitch damping rate	ζ_θ	≈ 0.3	%

Table C.1: Structural parameters of the pitch-flap wing

Appendix D

Equations of motion of the pitch-plunge-control wing

The matrices appearing in equations 4.3 and 5.4 are given in the following appendix, and the values of all relevant parameters are detailed in table D.1.

Structural matrices

The structural inertia matrix is given by

$$\mathbf{A} = \begin{pmatrix} m & S & S_\beta \\ S & I_\alpha & I_{\alpha\beta} \\ S_\beta & I_{\alpha\beta} & I_\beta \end{pmatrix}$$

where $a = x_f/b - 1$, $b = c/2$, $c_h = x_h/b - 1$, $I_{\alpha\beta} = I_\beta + b(c_h - a)S_\beta$.

The structural damping matrix is given by

$$\mathbf{D} = \mathbf{V}^{-1^T} \begin{pmatrix} 2\bar{m}_1\omega_1\zeta_1 & 0 & 0 \\ 0 & 2\bar{m}_2\omega_2\zeta_2 & 0 \\ 0 & 0 & 2\bar{m}_3\omega_3\zeta_3 \end{pmatrix} \mathbf{V}^{-1}$$

where $\mathbf{V}$ are the eigenvectors of the matrix $\mathbf{A}^{-1}\mathbf{E}$, $\bar{m}_i$ are the diagonal elements of the matrix $\mathbf{V}^T\mathbf{A}\mathbf{V}$ and ω_i are the square roots of the eigenvalues of the matrix $\mathbf{A}^{-1}\mathbf{E}$.

Finally, the stiffness matrices of the underlying and overlying linear systems are respec-

tively given by

$$\mathbf{E_1} = \begin{pmatrix} K_h & 0 & 0 \\ 0 & 0 & 0 \\ 0 & 0 & K_\beta \end{pmatrix}$$

$$\mathbf{E} = \begin{pmatrix} K_h & 0 & 0 \\ 0 & K_\alpha & 0 \\ 0 & 0 & K_\beta \end{pmatrix}$$

LTVA matrices

Adopting the Euler-Lagrange equation and assuming small displacements, the equations of motion of the pitch-plunge-control wing coupled to a rotational LTVA of mass m_a, stiffness k_a, damping c_a, located in x_a are derived. The resulting LTVA inertia, damping and stiffness matrices are given by

$$\mathbf{A_{ltva}} = m_a \begin{pmatrix} 0 & 0 & 0 & 0 \\ 0 & 0 & 0 & 0 \\ 0 & 0 & 0 & 0 \\ 0 & 0 & 0 & 1 \end{pmatrix}$$

$$\mathbf{C_{ltva}} = c_a \begin{pmatrix} 1 & x_a & 0 & -1 \\ x_a & x_a^2 & 0 & x_a \\ 0 & 0 & 0 & 0 \\ -1 & x_a & 0 & 1 \end{pmatrix}$$

$$\mathbf{E_{ltva}} = k_a \begin{pmatrix} 1 & x_a & 0 & -1 \\ x_a & x_a^2 & 0 & x_a \\ 0 & 0 & 0 & 0 \\ -1 & x_a & 0 & 1 \end{pmatrix}$$

note that the DOF that describes this LTVA is a translational DOF in a fixed referential while the LTVA DOF on the NLPFW (see chapter 3 and appendix C) is a rotational DOF in the wing's referential. As a result, the matrices of equations D couple the LTVA to the primary system in stiffness and damping instead of in inertia, which explains the difference between equations C and equations D.

Aerodynamic matrices

The aerodynamic inertia matrix is given by

$$\mathbf{B} = b^2 \begin{pmatrix} \pi & -\pi ab & -T_1 b \\ -\pi ab & \pi b^2(1/8 + a^2) & -(T_7 + (c_h - a)T_1)b^2 \\ T_1 b & 2T_{13}b^2 & -T_3 b^2/\pi \end{pmatrix}$$

The total aerodynamic damping matrix is given by $\mathbf{D} = \mathbf{D}_1 + \Phi(0)\mathbf{D}_2$, where $\Phi(t) = 1 - \Psi_1 e^{-\varepsilon_1 Ut/b} - \Psi_2 e^{-\varepsilon_2 Ut/b}$ is Wagner's function, with $\Psi_1 = 0.165$, $\Psi_2 = 0.335$, $\varepsilon_1 = 0.0455$, $\varepsilon_2 = 0.3$ and

$$\mathbf{D}_1 = b^2 \begin{pmatrix} 0 & \pi & -T_4 \\ 0 & \pi(1/2 - a)b & (T_1 - T_8 - (c_h - a)T_4 + T_{11}/2)b \\ 0 & (-2T_9 - T_1 + T_4(a - 1/2))b & bT_{11}/2\pi \end{pmatrix}$$

$$\mathbf{D}_2 = \begin{pmatrix} 2\pi b & 2\pi b^2(1/2 - a) & 2\pi b T_{11}/2\pi \\ -2\pi b^2(a + 1/2) & -2\pi b^3(a + 1/2)(1/2 - a) & -b^3(a + 1/2)T_{11} \\ b^2 T_{12} & b^3 T_{12}(1/2 - a) & b^3 T_{12} b T_{11}/2\pi \end{pmatrix}$$

The total aerodynamic stiffness is given by $\mathbf{F} = \mathbf{F}_1 + \Phi(0)\mathbf{F}_2 + \Xi\mathbf{F}_3$ where $\Xi = \Psi_1\varepsilon_1/b + \Psi_2\varepsilon_2/b$ and

$$\mathbf{F}_1 = b^2 \begin{pmatrix} 0 & 0 & 0 \\ 0 & 0 & (T_4 + T_{10}) \\ 0 & 0 & (T_5 - T_4 T_{10})/\pi \end{pmatrix}$$

$$\mathbf{F}_2 = \begin{pmatrix} 0 & 2\pi b & 2bT_{10} \\ 0 & -2\pi b^2(a + 1/2) & -2b^2(a + 1/2)T_{10} \\ 0 & b^2 T_{12} & b^2 T_{12} T_{10}/\pi \end{pmatrix}$$

$$\mathbf{F}_3 = \begin{pmatrix} 2\pi b & 2\pi b^2(1/2 - a) & b^2 T_{11} \\ -2\pi b^2(a + 1/2) & -2\pi b^3(a + 1/2)(1/2 - a) & -b^3(a + 1/2)T11 \\ b^2 T_{12} & b^3 T_{12}(1/2 - a) & b^3 T_{12} T_{11}/2\pi \end{pmatrix}$$

The aerodynamic state influence matrix is given by

$$\mathbf{W} = [2\pi b\mathbf{W}_0 \quad -2\pi b^2(a + 1/2)\mathbf{W}_0 \quad b^2 T_{12}\mathbf{W}_0 \quad \mathbf{0}_{1\times 4}]^T$$

where

$$\mathbf{W}_0 = \begin{pmatrix} -\Psi_1(\varepsilon_1/b)^2 \\ -\Psi_2(\varepsilon_2/b)^2 \\ \Psi_1\varepsilon_1(1-\varepsilon_1(1/2-a))/b \\ \Psi_2\varepsilon_2(1-\varepsilon_2(1/2-a))/b \\ \Psi_1\varepsilon_1(T_{10}-\varepsilon_1 T_{11}/2)/\pi b \\ \Psi_2\varepsilon_2(T_{10}-\varepsilon_2 T_{11}/2)/\pi b \end{pmatrix}$$

The aerodynamic state equation matrices are given by

$$\mathbf{W}_1 = \begin{pmatrix} 1 & 0 & 0 \\ 1 & 0 & 0 \\ 0 & 1 & 0 \\ 0 & 1 & 0 \\ 0 & 0 & 1 \\ 0 & 0 & 1 \end{pmatrix}$$

$$\mathbf{W}_2 = \begin{pmatrix} -\varepsilon_1/b & 0 & 0 & 0 & 0 & 0 \\ 0 & -\varepsilon_2/b & 0 & 0 & 0 & 0 \\ 0 & 0 & -\varepsilon_1/b & 0 & 0 & 0 \\ 0 & 0 & 0 & -\varepsilon_2/b & 0 & 0 \\ 0 & 0 & 0 & 0 & -\varepsilon_1/b & 0 \\ 0 & 0 & 0 & 0 & 0 & -\varepsilon_2/b \end{pmatrix}$$

The T_1-T_{14} coefficients are defined in Theodorsen [14] and many other classic aeroelasticity texts.

	Wing dimensions	
Chord (with flap)	c	25.4 cm
Span	s	52 cm
Flexural axis	x_f	$0.25 \times c$
	Flap dimensions	
Chord (flap alone)	$-$	6.25 cm
Span	s_2	52 cm
Hinge axis	x_h	$0.75 \times c$
	Inertial parameters	
Plunge mass	m	2.562 kg
Pitch inertia	I_α	0.0181 m.kg
Control inertia	I_β	2.6610^{-4} m.kg
Pitch static imbalance	S	0.0943 m.kg
Pitch-Flap inertia product	$I_{\alpha,\beta}$	0.0013 m.kg
Flap static imbalance	S_β	0.0084 m.kg
	Stiffness parameters	
Plunge stiffness	K_h	850.7 N/m
Pitch stiffness	K_α	34 Nm/rad
Flap stiffness	K_β	1.512 Nm/rad
	Modal parameters	
Plunge mode frequency	f_1	2.9 Hz
Pitch mode frequency	f_2	7.1 Hz
Control mode frequency	f_3	17.0 Hz
Plunge mode damping	ζ_1	0.87%
Pitch mode damping	ζ_2	1.39%
Flap mode damping	ζ_3	0.6%

Table D.1: Structural parameters of the experimental system

Appendix E

Publications

The list below presents the journal and conference papers that have originated from the present thesis.

Journal publications

1. E. Verstraelen, G. Dimitriadis, G. Del Ben Rossetto and E.H. Dowell, *Two-domain and three-domain limit cycles in a typical aeroelastic system with freeplay in pitch*, submitted to the Journal of Fluids and Structures, 2017

2. E. Verstraelen, G. Habib, G. Kerschen and G. Dimitriadis, *Experimental passive flutter suppression using a linear tuned vibration absorber*,
   submitted to the AIAA Journal, 2017

Conference publications

1. E. Verstraelen, G. Kerschen and G. Dimitriadis, *Internal Resonance and Stall-Flutter in a Pitch-Flap Wing in the Wind-Tunnel*, IMAC XXXIII Conference, Orlando FL, USA, February 2015

2. E. Verstraelen, J. Boutet, C. Grappasonni, G. Kerschen and G. Dimitriadis, *Theoretical and experimental investigation of a structurally and aerodynamically nonlinear pitch and flap wing*, IFASD Conference, Saint-Petersburg, Russia, July 2015

3. E. Verstraelen, G. Habib, G. Kerschen and G. Dimitriadis, *Experimental Passive Flutter Mitigation Using a Linear Tuned Vibrations Absorber*, IMAC XXXIV Conference, Orlando FL, USA, February 2016

4. E. Verstraelen, E. Gourc, G. Kerschen and G. Dimitriadis, *Passive flutter suppression using a nonlinear tuned vibration absorber*, Poster presentation, NNM2016 Conference, Liège, Belgium, July 2016

5. E. Verstraelen, G. Kerschen and G. Dimitriadis, *Flutter and limit cycle oscillation suppression using linear and nonlinear tuned vibration absorbers*, IMAC XXXV Conference, Garden Grove CA, USA, February 2017

6. E. Verstraelen, G. Kerschen and G. Dimiatriadis, *Freeplay-induced limit cycle oscillation mitigation using linear and nonlinear tuned vibration absorbers*, IFASD Conference, Como, Italy, June 2017

Bibliography

[1] A. R. Collar. The expanding domain of aeroelasticity. *The Journal of the Royal Aeronautical Society*, 50(428):613?636, 1946.

[2] G. Brewer. The collapse of monoplane wings. In *Flight magazine*, 1913.

[3] G.T.R. Hill. Advances in aircraft structural design. In *Proceedings of the Third Anglo-American Aeronautical Conference*, Brighton, England, 1951.

[4] A.H.G. Fokker. *The Flying Dutchman*. Henry Hold and Co., 1931.

[5] F.W. Lanchester. Torsional vibration of the tail of an airplane. In *British aeronautical research council reports and memoranda*, volume 276, 1916.

[6] Joint Aviation Auhorities. JAR-25: Large Aeroplaces, 05 1994.

[7] P.A. Farell and T.G. Ryall. Flight flutter test techniques at arl. Technical Report ADA227754, Aeronautical Research Laboratory, Melbourne, Australia, 08 1990.

[8] M. Matsumoto, K. Mizuno, K. Okubo, Y. Ito, and H. Matsumiya. Flutter instability and recent development in stabilization of structures. *Journal of Wind Engineering and Industrial Aerodynamics*, 95(9):888 – 907, 2007.

[9] M. Gu, C.C. Chang, W. Wu, and H.F. Xiang. Increase of critical flutter wind speed of long-span bridges using tuned mass dampers. *Journal of Wind Engineering and Industrial Aerodynamics*, 73(2):111–123, 1998.

[10] A. Casalotti, A. Arena, and W. Lacarbonara. Mitigation of post-flutter oscillations in suspension bridges by hysteretic tuned mass dampers. *Engineering Structures*, 69:62–71, 2014.

[11] H.L. Bohon. Panel flutter tests on full scale x-15 lower vertical stabilizer at mach number of 3.0. Technical Report TN D-1385, NASA, 1962.

[12] J.J Nichols. Final report: Saturn v, s-ivb panel flutter qualification test. Technical Report TN D-5439, NASA, 1969.

[13] Missing fasteners identified as cause of f-117 crash. (december 12, 1997). Retrieved from `http://edition.cnn.com/US/9712/12/briefs/stealth.fighter.crash/`.

[14] T. Theodorsen. General theory of aerodynamic instability and the mechanism of flutter. Technical Report NACA TR-496, NACA, 1935.

[15] Y.C. Fung. *An introduction to the Theory of Aeroelasticity.* Dover Publications Inc., 1993.

[16] R.L. Bisplinghoff, H. Ashley, and R.L. Halfman. *Aeroelasticity.* Dover Publications Inc., 1996.

[17] E.H. Dowell, R. Clark, D. Cox, Curtiss H.C. Jr., J.W. Edwards, K.C. Hall, D.A. Peters, R. Scanlan, E. Simiu, F. Sisto, and T.W. Strganac. *A modern course in aeroelasticity*, volume G.M.L. GLADWELL of *Solid mechanics and its applications.* Kluwer academic publishers, 2005.

[18] J.R. Wright and J.E. Cooper. *Introduction to Aircraft Aeroelasticity and Loads.* John Wiley & Sons, 2007.

[19] D.S. Woolston, H.L. Runyan, and T.A. Byrdsong. *Some effects of system nonlinearities in the problem of aircraft flutter.* National Advisory Committee for Aeronautics, Washington, D.C., 1955.

[20] S.C. McIntosh Jr., R.E. Reed Jr., and W.P. Rodden. Experimental and theoretical study of nonlinear flutter. *Journal of Aircraft*, 18(12):1057–1063, 2017/04/28 1981.

[21] T. O'Neil, H. Gilliat, and T.W. Strganac. Investigations of aeroelastic response for a system with continuous structural nonlinearities. In *AIAA, ASME, ASCE, AHS, and ASC, 37th, Structures, Structural Dynamics and Materials Conference*, Salt Lake City, UT, 1996.

[22] E.H. Dowell, J. Edwards, and T.W. Strganac. Nonlinear aeroelasticity. *Journal of Aircraft*, 40(5):857–874, 2017/05/19 2003.

[23] W.A. Silva, T.W. Strganac, and M.R. Hajj. Higher-order spectral analysis of a nonlinear pitch and plunge apparatus. In *46th AIAA/ASME/ASCE/ASC Structures, Structural Dynamics, and Materials Conference*, Austin, Texas, 2005. AIAA.

[24] A. Abdelkefi, R. Vasconcellos, A.H. Nayfeh, and M.R. Hajj. An analytical and experimental investigation into limit-cycle oscillations of an aeroelastic system. *Nonlinear Dynamics*, 71(1-2):159–173, 2012.

[25] S.J. Price, H. Alighanbari, and B.H.K. Lee. The aeroelastic response of a two-dimensional airfoil with bilinear and cubic structural nonlinearities. *Journal of Fluids and Structures*, 9(2):175 – 193, 1995.

[26] G. Dimitriadis. *Introduction to Nonlinear Aeroelasticity.* John Wiley & Sons, Ltd, 2017.

[27] Federal Aviation Administration. *Policy for Certification and Continued Airworthiness of Unbalanced and Mass-Balanced Control Surfaces*, 2007. FAA Policy Memorandum ANM-05-115-019.

[28] Z.C. Yang and L.C. Zhao. Analysis of limit cycle flutter of an airfoil in incompressible flow. *Journal of Sound Vibration*, 123:1–13, May 1988.

[29] A. Hauenstein, R. Laurenson, W. Everman, G. Galecki, and A. Amos. *Chaotic response of aerosurfaces with structural nonlinearities (Status report).* American Institute of Aeronautics and Astronautics, 2016/09/14 1990.

[30] L. Liu, Y.S. Wong, and B.H.K. Lee. Non-linear aeroelastic analysis using the point transformation method, part 1: freeplay model. *Journal of Sound and Vibration*, 253(2):447 – 469, 2002.

[31] K.W. Chung, C.L. Chan, and B.H.K. Lee. Bifurcation analysis of a two-degree-of-freedom aeroelastic system with freeplay structural nonlinearity by a perturbation-incremental method. *Journal of Sound and Vibration*, 299(3):520–539, 2007.

[32] C.C. Marsden and S.J. Price. The aeroelastic response of a wing section with a structural freeplay nonlinearity: An experimental investigation. *Journal of Fluids and Structures*, 21(3):257 – 276, 2005. Marine and Aeronautical Fluid-Structure InteractionsMarine Acoustics8th International Conference on Flow-Induced Vibrations.

[33] Y.M. Chen and J.K. Liu. Nonlinear aeroelastic analysis of an airfoil-store system with a freeplay by precise integration method. *Journal of Fluids and Structures*, 46:149 – 164, 2014.

[34] D.M. Tang and E.H. Dowell. Flutter and stall response of a helicopter blade with structural nonlinearity. *Journal of Aircraft*, 29(5):953–960, 1992.

[35] C.T. Tran and D. Petot. Semi-empirical model for the dynamic stall of airfoils in view of the application to the calculation of responses of a helicopter in forward flight. 5:35–53, 01 1981.

[36] S.H. Lim and I. Lee. Aeroelastic analysis of a flexible airfoil with a freeplay nonlinearity. *Journal of Sound and Vibration*, 193(4):823 – 846, 1996.

[37] D.M. Tang and E.H. Dowell. Aeroelastic response induced by free play, part 1: Theory. *AIAA Journal*, 49(11):2532–2542, 2011.

[38] D.M. Tang and E.H. Dowell. Aeroelastic response induced by free play, part 2: Theoretical/experimental correlation analysis. *AIAA Journal*, 49(11):2543–2554, 2011.

[39] P.C. Chen and D.H. Lee. Flight-loads effects on horizontal tail free-play-induced limit cycle oscillation. *Journal of Aircraft*, 45(2):478–485, 2008.

[40] M.D. Conner, D.M. Tang, E.H. Dowell, and L.N. Virgin. Nonlinear behaviour of a typical airfoil section with control surface freeplay: a numerical and experimental study. *Journal of Fluids and Structures*, 11(1):89–109, 1997.

[41] D.B. Kholodar. Nature of freeplay-induced aeroelastic oscillations. *Journal of Aircraft*, 51(2):571–583, 2014.

[42] D.A. Pereira, R.M.G. Vasconcellos, M.R. Hajj, and F.D. Marques. Effects of combined hardening and free-play nonlinearities on the response of a typical aeroelastic section. *Aerospace Science and Technology*, 50:44 – 54, 2016.

[43] H. Alighanbari. Aeroelastic response of an airfoil-aileron combination with freeplay in aileron hinge. *Journal of Aircraft*, 39(4):711–713, 2016/09/15 2002.

[44] J.T. Gordon, E.E. Meyer, and R.L. Minogue. Nonlinear stability analysis of control surface flutter with freeplay effects. *Journal of Aircraft*, 45(6):1904–1916, 2016/09/26 2008.

[45] M. Manetti, G. Quaranta, and P. Mantegazza. Numerical evaluation of limit cycles of aeroelastic systems. *Journal of Aircraft*, 46(5):1759–1769, 2016/09/15 2009.

[46] R. Vasconcellos, A. Abdelkefi, F.D. Marques, and M.R. Hajj. Representation and analysis of control surface freeplay nonlinearity. *Journal of Fluids and Structures*, 31:79 – 91, 2012.

[47] C.C. Cui, J.K. Liu, and Y.M. Chen. Simulating nonlinear aeroelastic responses of an airfoil with freeplay based on precise integration method. *Communications in Nonlinear Science and Numerical Simulation*, 22:933 – 942, 2015.

[48] National renewable energy laboratory osu wind tunnel test data. (july 6, 2012). Retrieved from `http://wind.nrel.gov/airfoils/OSU_data/data/`.

[49] W.J. McCroskey, K.W. McAlister, L.W. Carr, and S.L. Pucci. An Experimental Study of Dynamic Stall on Advanced Airfoil Sections Volume 1. Summary of the Experiment. *NASA Technical Memorandum*, (TM-84245-VOL-1), 1982.

[50] K.W. McAlister, S.L. Pucci, W.J. McCroskey, and L.W. Carr. An experimental study on dynamic stall on advanced airfoil sections Volume 2. Pressure and Force Data. *NASA Technical Memorandum*, (TM-84245-VOL-2), 1982.

[51] W.J. McCroskey, K.W. McAlister, L.W. Carr, S.L. Pucci, and O. Lambert. An experimental study of Dynamic Stall on advanced airfoil sections Volume 3. Hot-wire and hot-film measurements. *NASA Technical Memorandum*, (TM-84245-VOL-3), 1982.

[52] W.J. McCroskey. Inviscid flowfield of an unsteady airfoil. *AIAA Journal*, 11(8):1130–1137, 2017/11/09 1973.

[53] L.E. Ericsson and J.P. REDING. Unsteady flow concepts for dynamic stall analysis. *Journal of Aircraft*, 21(8):601–606, 2017/11/09 1984.

[54] D.M. Tang and E.H. Dowell. Comparison of theory and experiment for non-linear flutter and stall response of a helicopter blade. *Journal of Sound and Vibration*, 165(2):251 – 276, 1993.

[55] P. Dunn and J. Dugundji. Nonlinear stall flutter and divergence analysis of cantilevered graphite/epoxy wings. *AIAA Journal*, 30(1):153–162, 2018/01/18 1992.

[56] J. Li and G. Dimitriadis. Bifurcation behavior of airfoil undergoing stall flutter oscillations in low-speed wind tunnel. *AIAA Journal*, 47(11):2577–2596, 2009.

[57] N. Abdul Razak, T. Andrianne, and G. Dimitriadis. Flutter and stall flutter of a rectangular wing in a wind tunnel. *AIAA Journal*, 49(10):2258–2271, 2011.

[58] D. Borglund and J. Kuttenkeuler. Active wing flutter suppression using a trailing edge flap. *Journal of Fluids and Structures*, 16(3):271 – 294, 2002.

[59] M. Yu and H. Hu. Flutter control based on ultrasonic motor for a two-dimensional airfoil section. *Journal of Fluids and Structures*, 28:89 – 102, 2012.

[60] V. Mukhopadhyay. Transonic flutter suppression control law design using classical and optimal techniques with wind-tunnel results. In *40th AIAA/ASME/ASCE/AHS/ASC Structures, Structural Dynamics and Materials (SDM) Conference*, St. Louis, MO, 1999. AIAA.

[61] R. Huang, W. Qian, H. Hu, and Y. Zhao. Design of active flutter suppression and wind-tunnel tests of a wing model involving a control delay. *Journal of Fluids and Structures*, 55:409 – 427, 2015.

[62] 0. Sensburg, H. Honlinger, T. E. Noll, and L. J. Huttsell. Active flutter suppression on an f-4f aircraft. *Journal of Aircraft*, 19(5):354–359, 2017/10/05 1982.

[63] J.H. Han, J. Tani, and J. Qiu. Active flutter suppression of a lifting surface using piezoelectric actuation and modern control theory. *Journal of Sound and Vibration*, 291(3-5):706 – 722, 2006.

[64] R.W. Moses. Active vertical tail buffeting alleviation on an f/a-18 model in a wind tunnel, 01 1999.

[65] M. H. Shirk, T. J. Hertz, and T. A. Weisshaar. Aeroelastic tailoring - theory, practice, and promise. *Journal of Aircraft*, 23(1):6–18, 2017/08/24 1986.

[66] A.G. Cunha-Filho, A.M.G. de Lima, M.V. Donadon, and L.S. Leao. Flutter suppression of plates using passive constrained viscoelastic layers. *Mechanical Systems and Signal Processing*, 79:99 – 111, 2016. Special Issue from {ICEDyn} 2015.

[67] A. Malher, O. Doaré, and C. Touzé. Pseudoelastic Shape Memory Alloys to Mitigate the Flutter Instability: A Numerical Study. In M. Belhaq, editor, *Structural Nonlinear Dynamics and Diagnosis*, volume 168 of *Springer Proceedings in Physics*, pages https://www.springer.com/978–3–319–19850–7. springer, 2015.

[68] A. Malher, O. Doaré, and C. Touzé. Influence of a hysteretic damper on the flutter instability. *Journal of Fluids and Structures*, 68:356 – 369, 2017.

[69] H. Frahm. Device for damping vibrations of bodies., April 18 1911. US Patent 989,958.

[70] J. Ormondroyd and J.P. Den Hartog. Theory of the dynamic vibration absorber. *Transaction of the ASME*, 50:9–22, 1928.

[71] J.P. Den Hartog. *Mechanical vibrations*. McGraw-Hill, New York, 1934.

[72] J.E. Brock. A note on the damped vibration absorber, 1946.

[73] T. Asami and O. Nishihara. Closed-form exact solution to h∞ optimization of dynamic vibration absorbers (application to different transfer functions and damping systems). *Journal of Vibration and Acoustics*, 125(3):398–405, 2003.

[74] J.Q. Sun, M.R. Jolly, and M.A. Norris. Passive, adaptive and active tuned vibration absorbers—a survey. *Journal of Mechanical Design*, 117(B):234–242, 06 1995.

[75] O.V. Gendelman, L.I. Manevitch, A.F. Vakakis, and R. M'Closkey. Energy pumping in nonlinear mechanical oscillators: Part i – dynamics of the underlying hamiltonian systems. *Journal of Applied Mechanics*, 68:34–41, 2001.

[76] A.F. Vakakis and O.V. Gendelman. Energy pumping in nonlinear mechanical oscillators: part ii: resonance capture. *Journal of Applied Mechanics*, 68(1):42–48, 2001.

[77] A.F. Vakakis, O.V. Gendelman, L.A. Bergman, D.M. McFarland, G. Kerschen, and Y.S. Lee. *Nonlinear targeted energy transfer in mechanical and structural systems*, volume 156. Springer, 2008.

[78] E. Gourdon, N.A. Alexander, C.A. Taylor, C-H Lamarque, and S. Pernot. Nonlinear energy pumping under transient forcing with strongly nonlinear coupling: Theoretical and experimental results. *Journal of Sound and Vibration*, 300(3):522–551, 2007.

[79] S. Seguy, G. Michon, A. Berlioz, and E. Gourc. Chatter control in turning process with a nonlinear energy sink. *Advanced Materials Research*, 698:89–98, 7 2013.

[80] Y.S. Lee, A.F. Vakakis, L.A. Bergman, D.M. McFarland, and G. Kerschen. Suppression aeroelastic instability using broadband passive targeted energy transfers, part 1: Theory. *AIAA Journal*, 45(3):693–711, 2016/08/17 2007.

[81] Y.S. Lee, G. Kerschen, D.M. McFarland, W.J. Hill, C. Nichkawde, T.W. Strganac, L.A. Bergman, and A.F. Vakakis. Suppressing aeroelastic instability using broadband passive targeted energy transfers, part 2: Experiments. *AIAA Journal*, 45(10):2391–2400, 2016/08/17 2007.

[82] Y.S. Lee, A.F. Vakakis, L.A. Bergman, D.M. McFarland, and G. Kerschen. Enhancing the robustness of aeroelastic instability suppression using multi-degree-of-freedom nonlinear energy sinks. *AIAA Journal*, 46(6):1371–1394, 2016/08/17 2008.

[83] S.A. Hubbard, R.L. Fontenot, D.M. McFarland, P.G.A. Cizmas, L.A. Bergman, T.W. Strganac, and A.F. Vakakis. Transonic aeroelastic instability suppression for a swept wing by targeted energy transfer. *Journal of Aircraft*, 51(5):1467–1482, 2016/08/17 2014.

[84] N. Poovarodom, S. Kanchanosot, and P. Warnitchai. Application of non-linear multiple tuned mass dampers to suppress man-induced vibrations of a pedestrian bridge. *Earthquake Engineering & Structural Dynamics*, 32(7):1117–1131, 2003.

[85] S. Ema and E. Marui. A fundamental study on impact dampers. *International Journal of Machine Tools and Manufacture*, 34(3):407–421, 1994.

[86] N. Carpineto, W. Lacarbonara, and F. Vestroni. Hysteretic tuned mass dampers for structural vibration mitigation. *Journal of Sound and Vibration*, 333:1302–1318, 2014.

[87] R.E. Roberson. Synthesis of a nonlinear dynamic vibration absorber. *Journal of the Franklin Institute*, 254:205–220, 1952.

[88] J. Shaw, S.W. Shaw, and A.G. Haddow. On the response of the non-linear vibration absorber. *International Journal of Non-Linear Mechanics*, 24(4):281–293, 1989.

[89] R. Viguié and G. Kerschen. Nonlinear vibration absorber coupled to a nonlinear primary system: a tuning methodology. *Journal of Sound and Vibration*, 326(3):780–793, 2009.

[90] R. Viguié and G. Kerschen. On the functional form of a nonlinear vibration absorber. *Journal of Sound and Vibration*, 329(25):5225–5232, 12 2010.

[91] N.A. Alexander and F. Schilder. Exploring the performance of a nonlinear tuned mass damper. *Journal of Sound and Vibration*, 319(1):445–462, 2009.

[92] G. Habib, T. Detroux, R. Viguié, and G. Kerschen. Nonlinear generalization of den hartog's equal-peak method. *Mechanical Systems and Signal Processing*, 52-53:17 28, 2015.

[93] R. Bellet, B. Cochelin, P. Herzog, and P.-O. Mattei. Experimental study of targeted energy transfer from an acoustic system to a nonlinear membrane absorber. *Journal of Sound and Vibration*, 329(14):2768 – 2791, 2010.

[94] F.S. Collette. A combined tuned absorber and pendulum impact damper under random excitation. *Journal of Sound and Vibration*, 216(2):199–213, 1998.

[95] T. Nagase and T. Hisatoku. Tuned-pendulum mass damper installed in crystal tower. *The Structural Design of Tall Buildings*, 1(1):35–56, 1992.

[96] I. Kourakis. *Structural systems and tuned mass dampers of super-tall buildings: case study of Taipei 101.* PhD thesis, Massachusetts Institute of Technology, 2007.

[97] A.C. Webster and R. Vaicaitis. Application of tuned mass dampers to control vibrations of composite floor systems. *Engineering Journal of the American Institute of Steel Construction*, 29(3):116–124, 1992.

[98] P. Dallard, A.J. Fitzpatrick, A. Flint, S. Le Bourva, A. Low, R.M. Ridsdill Smith, and M. Willford. The london millennium footbridge. *Structural Engineer*, 79(22):17–21, 2001.

[99] X. Lu and J. Chen. Mitigation of wind-induced response of shanghai center tower by tuned mass damper. *The Structural Design of Tall and Special Buildings*, 20(4):435–452, 2011.

[100] X. Lu, P. Li, X. Guo, W. Shi, and J. Liu. Vibration control using atmd and site measurements on the shanghai world financial center tower. *The Structural Design of Tall and Special Buildings*, 23(2):105–123, 2014.

[101] Soon-Duck Kwon and Kwan-Soon Park. Suppression of bridge flutter using tuned mass dampers based on robust performance design. *Journal of Wind Engineering and Industrial Aerodynamics*, 92(11):919 – 934, 2004.

[102] M. Karpel. *Design for active and passive flutter suppression and gust alleviation*, volume 3482. National Aeronautics and Space Administration, Scientific and Technical Information Branch, 1981.

[103] S.H. Moon and S.J. Kim. Active and passive suppressions of nonlinear panel flutter using finite element method. *AIAA Journal*, 39(11):2042–2050, 8 2001.

[104] J. Luo, N.E. Wierschem, S.A. Hubbard, L.A. Fahnestock, D.D. Quinn, D.M. McFarland, B.F. Spencer Jr., A.F. Vakakis, and L.A. Bergman. Large-scale experimental evaluation and numerical simulation of a system of nonlinear energy sinks for seismic mitigation. *Engineering Structures*, 77:34 – 48, 2014.

[105] F. Nucera, D.M. McFarland, L.A. Bergman, and A.F. Vakakis. Application of broadband nonlinear targeted energy transfers for seismic mitigation of a shear frame: Computational results. *Journal of Sound and Vibration*, 329(15):2973 – 2994, 2010.

[106] N. Krylov, N.N. Bogoliubov, and S. Lefschetz. *Introduction to Non-linear Mechanics*. Annals of mathematics studies. Princeton University Press, 1949.

[107] C. Grappasonni, G. Habib, T. Detroux, and G. Kerschen. Experimental demonstration of a 3d-printed nonlinear tuned vibration absorber. In *XXXIII IMAC Conference & Exposition On Structural Dynamics*, Orlando, Florida, 2015.

[108] G. Habib and G. Kerschen. Suppression of limit cycle oscillations using the nonlinear tuned vibration absorber. In *Proceedings of the Royal Society of London A: Mathematical, Physical and Engineering Sciences*, volume 471, page 20140976. The Royal Society, 2015.

[109] A. Malher, C. Touzé, O. Doaré, G. Habib, and G. Kerschen. Passive control of airfoil flutter using a nonlinear tuned vibration absorber. In *11th International Conference on Flow-induced vibrations, FIV2016*, La Haye, Netherlands, August 2016.

[110] G.J. Hancock, J.R. Wright, and A. Simpson. On the teaching of the principles of wing flexure-torsion flutter. *Aeronautical Journal*, 89:285–305, 1985.

[111] T.P. Le and P. Argoul. Continuous wavelet transform for modal identification using free decay response. *Journal of Sound and Vibration*, 277(12):73–100, 2004.

[112] L.B. Magalas and T. Malinowski. Measurement techniques of the logarithmic decrement. In *Mechanical Spectroscopy II*, volume 89 of *Solid State Phenomena*, pages 247–260. Trans Tech Publications, 2 2003.

[113] T. Detroux, G. Habib, L. Masset, and G. Kerschen. Performance, robustness and sensitivity analysis of the nonlinear tuned vibration absorber. *Mechanical Systems and Signal Processing*, 60:799–809, 2015.

[114] G. Habib and G. Kerschen. A principle of similarity for nonlinear vibration absorbers. *Physica D: Nonlinear Phenomena*, 332:1 – 8, 2016.

[115] E. Verstraelen, G. Kerschen, and G. Dimitriadis. Flutter and limit cycle oscillation suppression using linear and nonlinear tuned vibration absorbers. In *XXXV IMAC Conference & Exposition On Structural Dynamics*, Garden Grove, California, 2017.

[116] J.W. Edwards. Unsteady aerodynamic modeling for arbitrary motions. *AIAA Journal*, 17(4):365–374, 2017/07/25 1979.

[117] G. Dimitriadis. Shooting-based complete bifurcation prediction for aeroelastic systems with freeplay. *AIAA Journal*, 48(6):1864–1877, 2008.

[118] M. di Bernardo, C.J. Budd, A.R. Champneys, and P. Kowalczyk. *Piecewise-smooth dynamical systems: Theory and Applications*. Springer, 2008.

[119] D.L. Brown, R.J. Allemang, R. Zimmerman, and M. Mergeay. Parameter estimation techniques for modal analysis. In *SAE Technical Paper*. SAE International, 02 1979.

[120] C.M. Denegri, V.K. Sharma, and J.S. Northington. F-16 limit-cycle oscillation analysis using nonlinear damping. *Journal of Aircraft*, 53(1):243–250, 2017/08/30 2015.